

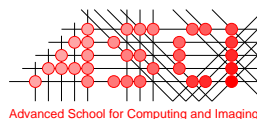
Model-Based Cell Tracking and Analysis in Fluorescence Microscopy

Oleh Dzyubachyk

Colophon

This book was typeset by the author using $\text{\LaTeX}2_{\epsilon}$. The main body of the text was set using a 10-points Palatino font. All graphics and images were included formatted as Encapsulated PostScript (TMAdobe Systems Incorporated). The final PostScript output was converted to Portable Document Format (PDF) and transferred to film for printing.

Cover design by Oleh Dzyubachyk. PCNA-GFP labeled CHO cells image is courtesy of Jeroen Essers.



Advanced School for Computing and Imaging

This work was carried out in the ASCI graduate school.
ASCI dissertation series number 231.

The research described in this thesis was carried out at the Erasmus MC – University Medical Center Rotterdam (Rotterdam, the Netherlands). This work was financially supported by the Netherlands Organization for Scientific Research (NWO) through VIDI-grant 639.022.401.

Financial support for the publication of this thesis was kindly provided by the Department of Radiology of Erasmus MC – University Medical Center Rotterdam, and the Erasmus University Rotterdam, the Netherlands.

Copyright © 2011 by Oleh Dzyubachyk. All rights reserved. No part of this publication may be reproduced or transmitted in any form or by any means, electronic or mechanical, including photocopy, recording, or any information storage and retrieval system, without permission in writing from the author.

ISBN 978-94-91211-18-8

Printed by Ipskamp Drukkers

MODEL-BASED CELL TRACKING AND ANALYSIS IN FLUORESCENCE MICROSCOPY

MODELGESTUURDE METHODEN VOOR HET VOLGEN EN
ANALYSEREN VAN CELLEN IN DE FLUORESCENTIE MICROSCOPIE

PROEFSCHRIFT

TER VERKRIJGING VAN DE GRAAD VAN DOCTOR AAN DE
ERASMUS UNIVERSITEIT ROTTERDAM
OP GEZAG VAN DE
RECTOR MAGNIFICUS

PROF.DR. H.G. SCHMIDT

EN VOLGENS BESLUIT VAN HET COLLEGE VOOR PROMOTIES.

DE OPENBARE VERDEDIGING ZAL PLAATSVINDEN OP
WOENSDAG 13 APRIL 2011 OM 13:30 UUR

DOOR

OLEH DZYUBACHYK

GEBOREN TE LVIV, OEKRAÏNE



Promotiecommissie

Promotor: **Prof.dr. W.J. Niessen**

Overige leden: **Prof.dr. R. Kanaar**
Prof.dr. R. Deriche
Prof.dr. J. Swedlow

Copromotor: **Dr.ir. H.W. Meijering**

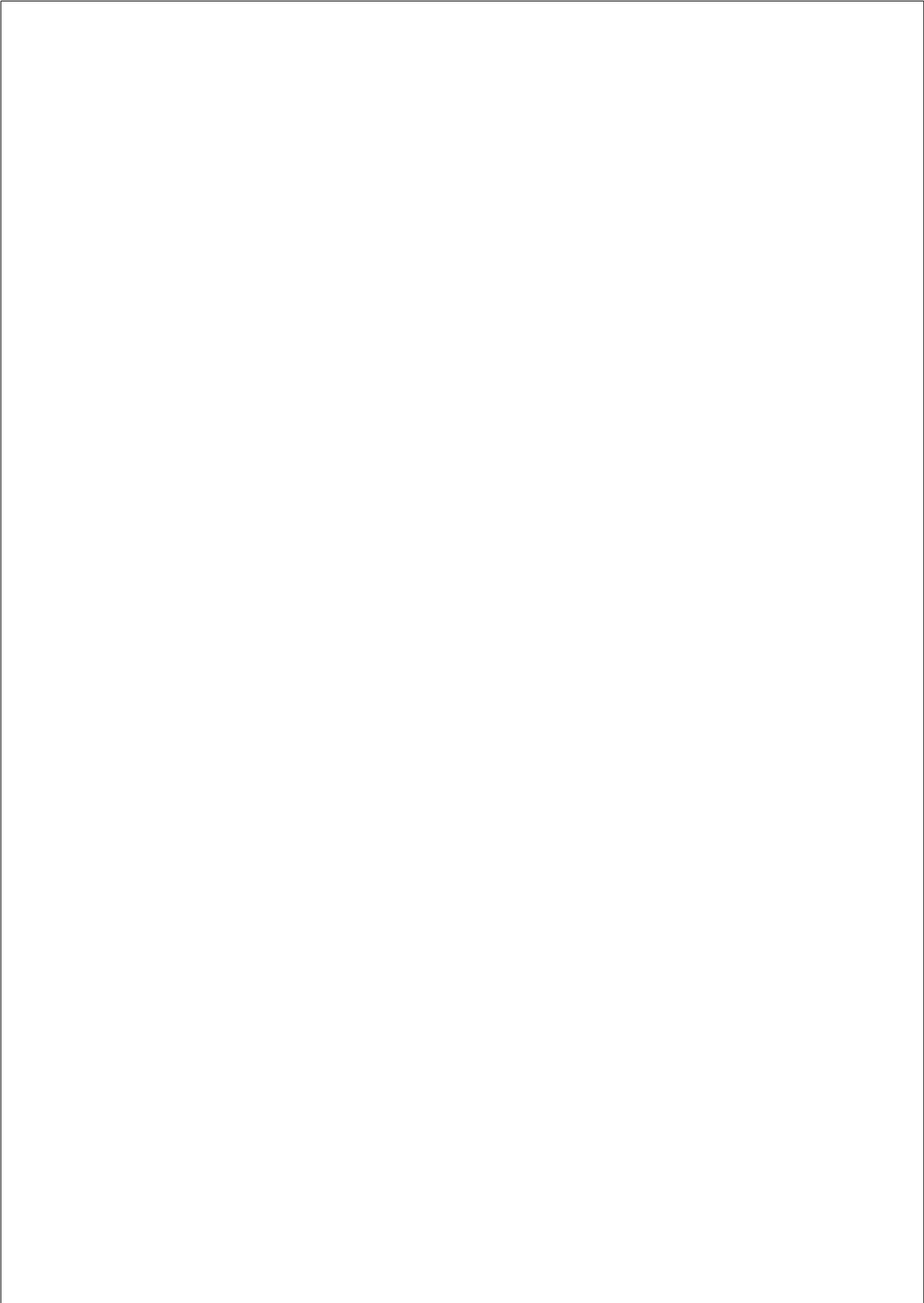
Contents

Colophon	ii
1 Introduction	1
1.1 Fluorescence Microscopy	1
1.2 Mathematical Methods for Image Analysis	2
1.3 Thesis Outline	4
2 Tracking in Cell and Developmental Biology	7
2.1 Introduction	8
2.2 Cell Tracking	9
2.2.1 Segmenting Individual Cells	9
2.2.2 Connecting Cells Over Time	10
2.2.3 Cell Tracking in Practice	12
2.3 From Cells to Molecules	12
2.3.1 Cell Motion Correction	13
2.3.2 Foci Segmentation and Tracking	13
2.4 From Cells to Organisms	15
2.4.1 Tracking Embryogenesis	16
2.4.2 Tracking Organism Behavior	16
2.4.3 Organism Tracking in Practice	18
2.5 Conclusions	18
3 Advanced Level-Set Based Cell Tracking in Time-Lapse Fluorescence Microscopy	21
3.1 Introduction	22
3.1.1 Related Work	23
3.1.2 Our Method	24
3.1.3 Chapter Outline	25
3.2 Segmentation With Coupled Active Surfaces	25
3.3 Proposed Algorithm	28
3.3.1 Algorithm Outline	28
3.3.2 Non-PDE Based Energy Minimization	30
3.3.3 Separation of Initially Touching Cells	31

3.3.4	Capturing Cell Division	32
3.3.5	Stopping Criterion	33
3.3.6	Internal Energy	34
3.3.7	Separation of Touching Cells	35
3.3.8	Re-Initialization of the Level Sets	37
3.3.9	Capturing Entering Cells	37
3.4	Experimental Results	38
3.4.1	Image Data Sets	38
3.4.2	Algorithm Parameter Settings	40
3.4.3	Segmentation Evaluation	41
3.4.4	Tracking Evaluation	45
3.4.5	Computation Time	48
3.5	Conclusions	48
4	Automated Analysis of Time-Lapse Fluorescence Microscopy Images: From Live Cell Images to Intracellular Foci	49
4.1	Introduction	50
4.2	Methods	51
4.2.1	Cell Analysis	51
4.2.2	Foci Analysis	53
4.3	Validation	57
4.3.1	Foci Counting	57
4.3.2	Cell Phase Identification	58
4.4	Conclusions	60
5	Model-Evolution Based Tracking of <i>Caenorhabditis Elegans</i> Embryoge- nesis in Fluorescence Microscopy	63
5.1	Background	64
5.2	Methods	65
5.2.1	Initial Segmentation	65
5.2.2	Division and Motion Assessment	65
5.2.3	Multi-Cell Segmentation and Tracking	69
5.2.4	Correction and Output	71
5.3	Results and Discussion	73
5.3.1	Test Data Sets	73
5.3.2	Algorithm Parameters	74
5.3.3	Segmentation and Tracking Errors	74
5.3.4	Implementation and Processing Times	77
5.4	Conclusions	77
6	Summary	81
	Bibliography	85

CONTENTS vii

Samenvatting	97
Acknowledgement	101
PhD Portfolio	103
Publications	105
Color Image Section	107
Curriculum Vitae	119



Introduction

1.1 Fluorescence Microscopy

Biological research is impossible to imagine without a microscope. Latest generations of microscopes, able to produce huge arrays of multidimensional data, only distantly resemble Leeuwenhoek's first microscope. Every advance in visualization techniques and hardware brings us one step closer to understanding life, e.g., how genome information gives identity to cells, how cells constitute organisms and how errant cells cause disease [151]. Discovery of the green fluorescent protein (GFP) [150] in the nineties of the previous century was definitely one of the most important milestones on that path, giving new strong impulse to the field of fluorescence microscopy.

Unlike other optical microscopy techniques, where images are formed by reflection and absorption, fluorescence microscopy, as its name suggests, is based on the phenomenon of fluorescence. For visualizing an organic or inorganic structure of interest, it is labelled with a fluorescent molecule called *fluorophore*. This molecule has a special property, that, when illuminated with a laser light of a certain wavelength, it is able to emit a light wave that can be detected by a charge-coupled device (CCD) [91]. Modern CCD cameras can very successfully register the light of different wavelength emitted by different fluorophores whose discovery quickly followed the discovery of GFP [19,60]. This enables acquiring multi-spectral image data, in which different structures of interest are visualized in different colors. Using optical sectioning technique it is possible to obtain three-dimensional views of an object by splitting the region occupied by the object in a number of slices, imaged by moving the focal plane of the microscope during acquisition [57]. Finally, fluorescence microscopy allows producing multiple images of the same scene over time, resulting in an image sequence that enables studying object dynamics [40,74,154].

All the mentioned properties quickly made fluorescence microscopy very popular for studying biological processes on different levels. From the molecular to the whole organism level, fluorescence microscopy is capable to produce up to five-

dimensional data. Spatial and temporal resolution ranges from $0.1\ \mu\text{m}$ to $1\ \text{cm}$ for the lateral dimensions, $0.1\ \mu\text{m}$ to $1\ \text{mm}$ for the depth, and $0.1\ \mu\text{s}$ to $10^4\ \text{s}$ for the time. Currently, none of the many other available imaging methods [151] can match fluorescence microscopy in ability to provide such combinations of spatial and temporal resolution. At the same time, it is a highly dynamic field, with a considerable amount of research being carried out to widen the mentioned ranges. For example, new generations of fluorophores, like Alexa Fluors [118], are less prone to photobleaching [17], thus enabling imaging with higher temporal resolution or/and over a longer time period. The most recent developments in the field, such as photo-activated localization microscopy (PALM) [11] or stochastic optical reconstruction microscopy (STORM) [75] techniques, allow resolving two structures that are as close to each other as $20\text{--}30\ \text{nm}$ in the lateral and $50\text{--}60\ \text{nm}$ in the axial dimension. The ever-growing size and complexity of the acquired image data, as a consequence, necessitates the increase of sophistication level of specialized computer tools and techniques for analyzing the fluorescence microscopy time-lapse data. This thesis addresses the need for efficient automated methods by employing several modern mathematical computer vision concepts for performing such analysis.

1.2 Mathematical Methods for Image Analysis

The human vision system is a sophisticated system that is able to visually extract necessary information from lower-level image features and group them into a meaningful high-level structure. This phenomenon is referred to as perceptual grouping, a term which includes grouping by proximity, similarity, continuation, closure, and symmetry [96]. For simpler scenes, it is sometimes sufficient to use only one of the mentioned groupings, for example, when structures of interest are extracted from the images based on shape or intensity similarity. However, in most of the cases, all those properties should be used in combination in order to provide the complete picture. This is definitely the case when it comes to analysis of biological image data in all its growing complexity. With ever-improving quality of the images, it is not difficult, even for non-experts, to visually decompose a scene into meaningful components. Unfortunately, visual analysis, though very useful in many situations, cannot satisfy all the needs for being purely qualitative, whereas in most of the cases quantitative measures can provide much more extensive and reliable information about the data. This point appears to be the weakest link in the chain of image analysis by humans. Manual measurements often appear to be error-prone, suffer from low reproducibility and, especially, poor productivity. This calls for automated image analysis. On the other hand, while being able to extract high-quality measurements from the images, computers cannot completely substitute humans because of one simple reason: they can only see what humans have programmed them to see. Modern computer-based image analysis systems are already quite successful in specific tasks, performing equally to, or even better than humans, but reconstructing the complete human vision system in all its complexity still remains a major challenge.

The trend in developing modern tools for image analysis, biological imaging among others, lays in incorporating as much of the available information about the

subject as possible. Usually this is quite a difficult task in itself, since the information sources can be of very different nature: intensity, shape, texture, smoothness, spatiotemporal relationships, etc. Especially for traditional, “naive”, image processing methods, e.g. morphology or thresholding, it becomes an insuperable hurdle [6]. On the other hand, many examples from other disciplines, in particular physics, demonstrate how effectively such complex problems can be resolved by formalizing and reformulating them into purely mathematical problems. For the majority of practical computer vision problems, solutions (or good approximations to them) of the corresponding formalized problems are known. Although not every mathematical theory can be directly applied to image analysis, the number of mathematical concepts that have found their application in computer vision is constantly growing. In particular, applied to the problem of segmentation and tracking, the theories of variational calculus and partial differential equations have proven to be very successful [119]. Generally, a computer vision problem can in mathematical formulation be cast into optimizing a function (or a functional) of a certain kind. As it is often required to satisfy multiple optimization criteria at the same time, this is typically achieved by combining all the mentioned criteria in one *energy functional* and solving the corresponding energy minimization problem, for which, in turn, methods from variational calculus [54] can be used. Because of the complexity of the most computer vision problems, many corresponding mathematical problems are ill-posed (have more than one solution) and/or cannot be solved analytically. For such cases, effective algorithms from the fields of partial differential equations and numerical calculus exist that can approximate the desired solution with the required precision.

Thus, no wonder that energy minimization methods [5,6,119] have become very popular choice for object tracking and segmentation as they can readily combine all the information from different sources and nature into one energy functional. For example, extracting objects of target intensity I_0 can be achieved by minimizing the following energy [23]:

$$E_{intensity}(I) = \int_{\Omega} (I(\mathbf{x}) - I_0)^2 d\mathbf{x}, \quad (1.1)$$

where I is the image intensity and Ω is the image region. The expected shape of the object can be incorporated in a similar manner [121]. Smoothness of the object's boundary ϕ can be imposed by minimizing the absolute value of the gradient of its Heaviside function $H(\phi)$:

$$E_{smoothness}(\phi) = \int_{\Omega} |\nabla H(\phi(\mathbf{x}))| d\mathbf{x}, \quad (1.2)$$

and so on. The total energy term to be minimized is in this case a composition (sum) of several terms, where the impact of each of the constituents on the final result can be adjusted by using proper weighting factors.

Finding the desired energy minimum requires, in general, usage of specialized iterative methods since the obtained Euler-Lagrange partial differential equation cannot be solved analytically. Typically, this is achieved by introducing an artificial time parameter and calculating the energy minimum via the gradient descent

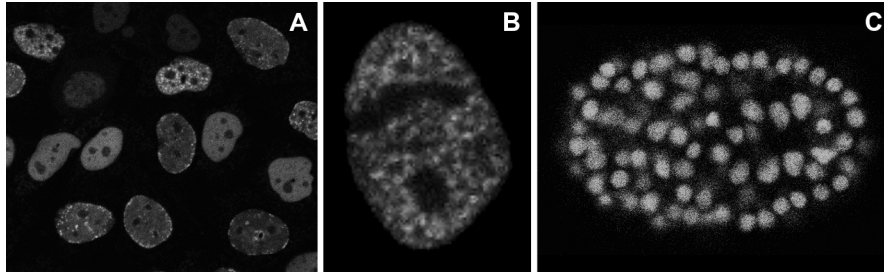


Figure. 1.1: Three levels of biological image data considered in this thesis: (A) cell level, (B) intracellular level, (C) whole-organism level (*Caenorhabditis elegans* nematode worm).

method [23]. Alternatively, more efficient minimization methods, such as graph cuts [15], exist for certain types of energy functionals.

The subject of this thesis is the development of mathematical methods to facilitate quantitative analysis of time-lapse fluorescence microscopy data. Such analysis can be performed on three different levels: whole organism, cell and intracellular, all of which are considered in this thesis (see Figure 1.1). Of these three levels, the cell-level plays the most prominent role since it serves as a basis for analysis on the other two levels. Specialized mathematical computer vision methods were customized for addressing the challenges posed by the data on each of the three mentioned levels of biological image analysis.

1.3 Thesis Outline

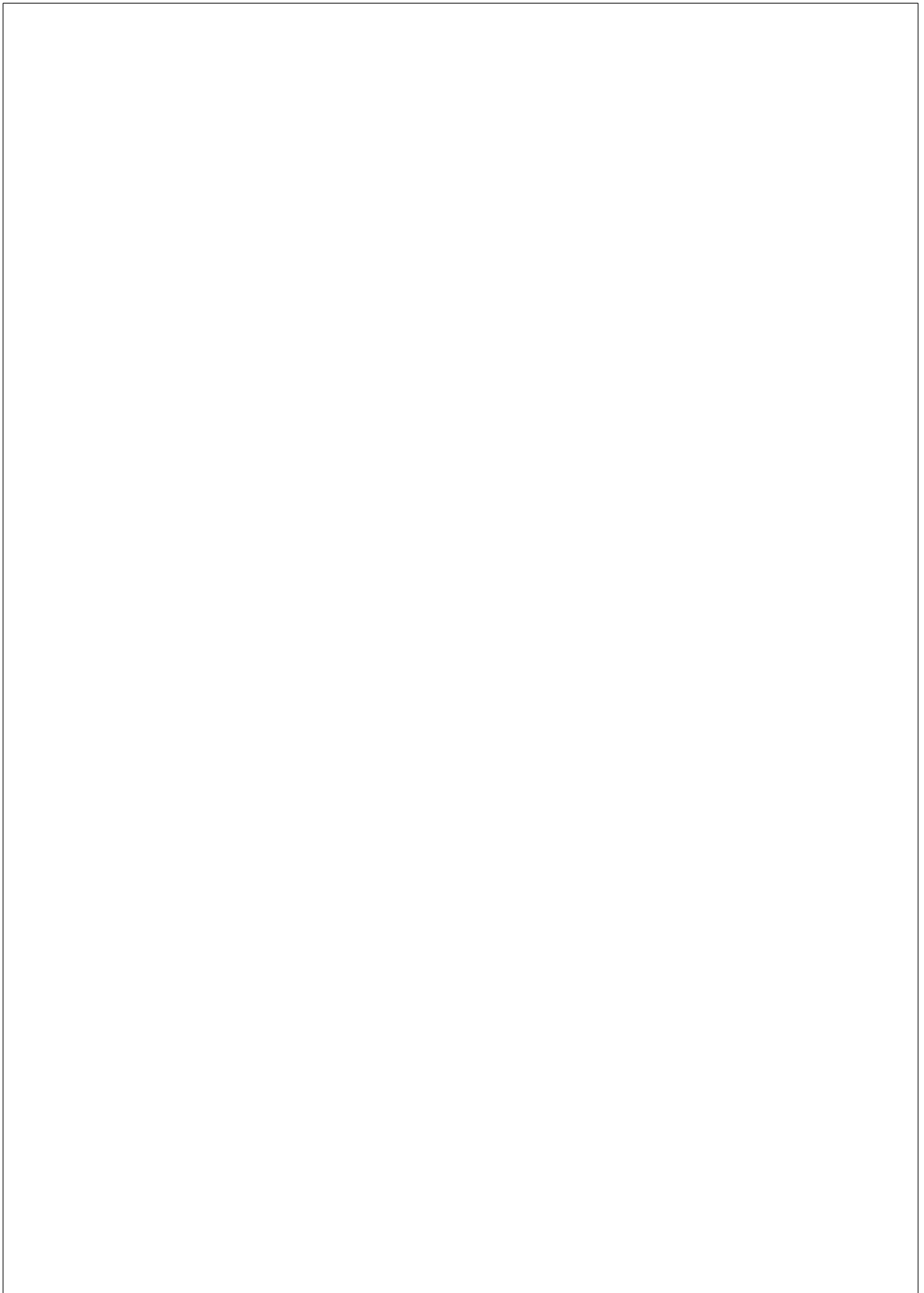
In **Chapter 2** of this thesis an overview of the computer methods and techniques used for analysis of time-lapse fluorescence microscopy data is given. Every aforementioned level of analysis is considered separately, and for each of them the most important challenges and requirements posed on the tools being developed are described. From this perspective, all relevant methods, from the “classical” to the most recent ones, and all the modern trends and research directions are discussed. The key concepts and ideas presented in this chapter are illustrated with examples on real microscopy data.

In **Chapter 3** a new cell segmentation and tracking algorithm is presented. Special attention is paid to the quality of the final segmentation and tracking results, since, as mentioned earlier, this step serves as a basis for further analysis on the intracellular- and the whole-organism levels. Thus, even small quality improvements at this stage may have considerable positive impact on the total performance of the whole system. For performing segmentation and tracking, we make use of the modern variational approach called *model evolution*. The main idea behind this approach is that each object being tracked is represented by a model, which is fitted to the data at every step, resulting in a segmentation of the object. Such “fitting”, at the same time, also provides tracking of the object by mimicking the object’s motion and deformation that occurred between two successive acquisitions, thus bridging

the gap between two imaged discrete states. Level sets are chosen as the model for yielding high-quality segmentation of complex and very inhomogeneous data, their ability to work in arbitrary-dimensional spaces, and to naturally change their topology. The algorithm is both evaluated by comparing it to human experts and publicly available tools.

In **Chapter 4** we further extend the framework presented in the previous chapter for performing intracellular analysis. The processing starts with applying a motion correction step, which is shape-based and is implemented as a variational energy minimization problem for matching two signed distance functions. The energy functional being minimized contains the following components: rigid-deformation, non-rigid deformations, and smoothness of the deformation field, which results in very accurate and realistic registrations. Fluorescent foci were chosen as the subject of the analysis on this level. For segmenting foci, a very general algorithm is developed that uses as little of the prior information about the exact nature of the imaged data as possible. The method is validated by comparing to human experts on real fluorescence microscopy data. Finally, the performance of the complete framework, from cell segmentation and tracking, to motion correction and foci segmentation, is illustrated on the problem of detecting the cell phase in proliferating cell nuclear antigen (PCNA) image data. An algorithm that is presented infers cell phase from the obtained statistics about the foci population, including average size and intensity, and spatial distribution.

Finally, **Chapter 5** demonstrates how the model-evolution-based cell tracking algorithm can be applied for analysis on the whole-organism level. The method presented in Chapter 2 was considerably extended and modified for performing segmentation and tracking on *C. elegans* embryogenesis data. Using a model-evolution-based method proves to be very beneficial in this case as it enables incorporating into the segmentation of each time step all the information about the previous state of the system. This property is very important for such data, whose complexity grows proportionally to the number of cells constituting the organism at the given moment in time. The method is validated on real time-lapse fluorescence microscopy sequences, and is shown to be able to track *C. elegans* embryogenesis for more than 3 hours, from the 4-cell to the 350-cell stage.



Tracking in Cell and Developmental Biology

2



Abstract — *The past decade has seen an unprecedented data explosion in biology. It has become evident that in order to take full advantage of the potential wealth of information hidden in the data produced by even a single experiment, visual inspection and manual analysis are no longer adequate. To ensure efficiency, consistency, and completeness in data processing and analysis, computational tools are essential. Of particular importance to many modern live-cell imaging experiments is the ability to automatically track and analyze the motion of objects in time-lapse microscopy images. This chapter surveys the recent literature in this area. Covering all scales of microscopic observation, from cells, down to molecules, and up to entire organisms, it discusses the latest trends and successes in the development and application of computerized tracking methods in cell and developmental biology.*

Based upon: E. Meijering, O. Dzyubachyk, I. Smal, W. A. van Cappellen. Tracking in Cell and Developmental Biology. *Seminars in Cell and Developmental Biology*, vol. 20, no. 8, October 2009, pp. 894–902.

2.1 Introduction

It has been increasingly recognized in recent times that life is a miraculous symphony [106]. From fast metabolic pathways to the cell cycle, to the beating of the heart, all the way to annually repeating seasonal behaviors, life is composed of a multitude of interconnected oscillations, together constituting a gigantic orchestra spanning at least 10 orders of time magnitude. Recent investigations seem to suggest that careful coordination of these rhythms and their interactions is an important precondition for the maintenance of normal development and health. Conversely, a disturbance at any level of this intricate time network can be expected to result in disease. Although it is not our purpose here to discuss the interesting findings of chronobiological investigations, they do emphasize the importance of studying life's processes in both space and time [151], that is, to analyze their structure and function.

The ability to visualize cells and subcellular dynamic processes in space and time has been made possible by revolutionary developments in imaging technology in the past two decades. Advances in molecular biology, organic chemistry, and materials science have resulted in an impressive toolbox of fluorescent proteins (GFP and variants) and nanocrystals (quantum dots), and have enabled the study of protein expression, localization, conformation, diffusion, turnover, trafficking, and interaction [60, 94]. On the hardware side, advances in optical systems design have taken light microscopy from widefield to (multiphoton) confocal and spinning disk microscopy [122, 142], and more recent efforts to break the diffraction barrier have further extended the palette [55, 71]. Together, these developments have redefined biological research by enabling the switch from fixed to living cells and from qualitative to quantitative imaging [151, 156].

As was to be expected, the new possibilities offered by these developments to image (sub)cellular processes in space, time, and at multiple wavelengths, have resulted in a true data explosion. It has now become evident that in order to ensure efficiency, consistency, and completeness in handling and examining the wealth of image data acquired in even a single experiment, computational image management, processing, and analysis methods are indispensable [1, 43, 50, 108, 123, 124, 145, 146, 173]. Thus, it seems that the bottleneck in putting modern imaging technologies to high-throughput use, has shifted from the "wetware" and the hardware to the development of adequate software tools and data models. While the need for such tools has been recognized for a long time in the medical imaging communities, and advanced image processing, computer vision, and pattern recognition methods have been developed in the past 30 years to enable computer assisted diagnosis in various clinical applications [9, 45, 144], it is only since relatively recently that similar methods are being explored to facilitate automated image analysis in biological imaging [129, 166].

This chapter briefly surveys the latest trends and successes in the endeavor to take full advantage of the vast amounts of image data acquired in biological imaging experiments. The emphasis is on tracking and motion analysis of objects in time-lapse microscopy images. Updating previous surveys, aimed at engineers [1, 103, 176] or biologists [43, 58, 78] from different perspectives, we cover tracking at

all scales of microscopic observation, from molecules, to cells, to organisms. In view of the rapid developments in the field, and because of space limitations in the present chapter, we consider only (a subset of) works published since the year 2000. First, we give an overview of recent cell segmentation and tracking algorithms, which in many experiments constitute the basis for further analyses. In the subsequent sections, we shift focus in two possible directions: from cells down to molecules (capturing the trajectories of intracellular particles), and from cells up to organisms (following embryogenesis and adult locomotory behavior). The chapter hopefully serves as a useful source of pointers to the relevant (mostly methodological) literature on tracking for a wide variety of applications in cell and developmental biology.

2.2 Cell Tracking

Being the fundamental units of life, cells are the key actors in many biological processes. Cell proliferation, differentiation, and migration are essential for the conception, development, and maintenance of any living organism. These processes also play a crucial role in the onset and progression of many diseases. Understanding physiological processes in health and disease and developing adequate drugs requires the imaging and analysis of the (morpho)dynamic behavior of single cells or cells in tissues under normal and perturbed conditions [42]. This typically involves the tracking and quantification of large numbers of cells in time-lapse fluorescence, phase-contrast, or intravital microscopy data sets consisting of hundreds to many thousands of image frames, making manual analysis no option, especially in 3D.

The automation of these tasks faces several challenges, including the generally poor image quality (low contrast and high noise levels), the varying density of cell populations due to division and cells entering or leaving the field of view, and the possibility of cells touching each other without showing sufficient image contrast. Many computerized methods for cell tracking have already been proposed, and some of these have found their way to commercial and open-source software tools (summarized in [67]), but the consensus arising from the literature seems to be that any specific tracking task requires dedicated (combinations of) algorithms to obtain optimal results. Nevertheless, several trends can be observed in the development of new cell tracking methods, suggesting the superiority of particular algorithms.

2.2.1 Segmenting Individual Cells

Cell tracking methods generally consist of two main image processing steps: 1) cell segmentation (the spatial aspect of tracking), and 2) cell association (the temporal aspect). Segmentation is the process of dividing an image into (biologically) meaningful parts (segments), resulting in a new image containing for each pixel a label indicating to which segment it belongs (such as “foreground” versus “background”). One approach to segmentation is to compare the value of each image pixel to a preset threshold value and to label pixels with values above (below) the threshold as foreground (background) [166]. Due to its simplicity, thresholding is one of the

most commonly used segmentation methods, but it is also one of the most error-prone [104]. It will be successful only if cells are well separated and their intensities differ sufficiently and consistently from the background—a condition hardly ever met in live cell imaging due to severe noise, autofluorescence and photobleaching (in the case of fluorescence microscopy), or strongly varying intensities and halos (in the case of phase- or differential interference contrast microscopy).

More sophisticated methods for cell segmentation include fitting predetermined cell intensity profiles (templates) to the image data. This template matching approach works well for images showing consistent cell shape [77], but fails in the case of significant variations in cell morphology (between cells per image, or per cell over time, or both). A more popular approach is to use the so-called watershed transform. In this case, an image is considered a topographic relief, and “flooding” this relief from the local intensity minima completely subdivides the image into regions and delimiting contours, by analogy termed “catchment basins” and “watersheds”, respectively. The most important drawbacks of this method are its sensitivity to noise and its tendency to yield too fragmented results (oversegmentation). Nevertheless, by combination with carefully designed pre- and postprocessing strategies, such as marking and model-based segment merging, the method has been successfully applied to cell segmentation in microscopy [92, 157, 170, 172].

Recent years have shown an increasing interest in the use of deformable models for cell segmentation [24, 35, 37, 41, 44, 90, 107, 115, 128, 135, 174]. These are defined either explicitly as parametric contours (mostly for 2D applications) or implicitly as the zero-level of a so-called level-set function (a mathematical concept that can be applied to image data of any dimensionality). The latter approach is often preferred, as it can naturally capture topological changes, such as cell division. Starting from a coarse, initial segmentation, deformable models are iteratively evolved in the image domain to minimize a predefined energy functional (Figure 2.1). The modeling aspect lies primarily in the definition of this energy functional. Typically it consists of image-related terms (based on image features such as intensity, gradients, and texture) and image-independent terms (based on shape properties such as boundary length or surface area, curvature, and similarity to reference shapes). This mixture of terms enables the incorporation of both image information and prior knowledge about the biological application [176]. In contrast with the watershed transform, model-evolution approaches have the tendency to yield undersegmentation of the images (the contours or surfaces of neighboring cells may easily merge in the process), and usually require postprocessing steps to refine the results.

2.2.2 Connecting Cells Over Time

After segmentation, the second step in achieving cell tracking is cell association. This refers to the process of identifying and linking segmented cells from frame to frame in the image sequence to obtain cell trajectories. The simplest approach to accomplish this is to associate each cell in any frame to the spatially nearest cell in the next frame (for example according to centroid position) within a predefined range. However, when dealing with many cells or rapid cell movements, this may easily lead to mismatches. In order to allow for better discrimination of potential matches,

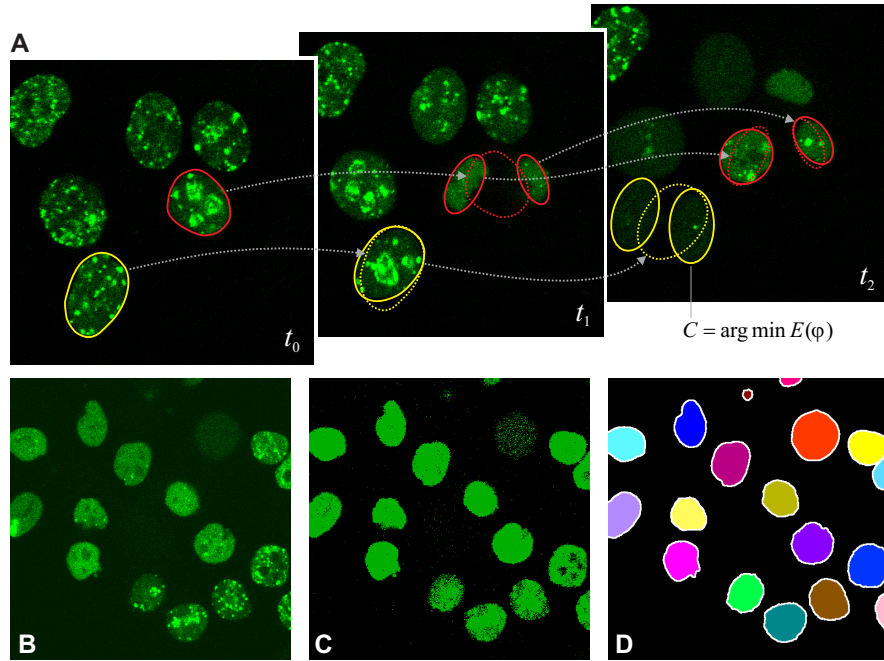


Figure. 2.1: Cell tracking. (A) Three frames from a time-lapse fluorescence microscopy image, illustrating the concept of model-evolution based cell segmentation and association. Cell contours or surfaces can be defined parametrically or as the zero-level of a higher-dimensional function. In each image frame, the final contour of a cell (solid line) is obtained by minimization of an energy functional, typically consisting of image-based and shape-based terms. The initial cell contour (dotted line) for each frame is usually taken to be the final contour from the previous frame. Cell divisions can be detected by monitoring the shape of the contour function during energy minimization. (B) Depending on the type of labeling, the appearance of cells (or in this case their nuclei) may vary greatly, within one frame as well as over time. (C) Thresholding usually results in a very noisy (at low thresholds) or fragmented (at high thresholds) segmentation. (D) Model-based segmentation (in this case using level sets) can yield much more sensible results.

the definition of “nearest” may be extended to include similarity in (average) intensity, area or volume, perimeter or surface area, orientation of major and minor axes, boundary curvature, estimated displacement, and other features. Increasing the number of features used for comparison reduces the risk of ambiguity. A similar argument applies when using so-called mean-shift processes to iteratively compute cell positions [28,36].

Several of the discussed methods for cell segmentation can naturally be extended to also perform cell association. The concept of template matching, for example, can serve as a basis for image registration between time points. Registration refers to the process of (global or local) alignment of images, using intensity- or geometry-based features. This can be done at the cell level [165], at the level of feature points [100], or down to the pixel level, reminiscent of optic-flow schemes [67,169]. In the case

of deformable models, cell association can be performed “on the fly”, by using the segmentation results in any frame as initialization for the segmentation process in the next frame (Figure 2.1). Essentially, this is again a nearest-neighbor linking approach, which works well if the population density is not too high and the rate at which images are acquired is such that cells do not move more than at most their diameter between consecutive frames. If these conditions are not met, or they need to be compromised for practical reasons, more sophistication is required, such as the use of gradient-vector flows [127, 174], estimated cell dynamics [35, 135], and special procedures to handle cell contacts, divisions, appearances, and disappearances [44, 167]. Another trend in the attempt to achieve more robustness is the use of probabilistic schemes [32, 77, 90, 135].

2.2.3 Cell Tracking in Practice

Once the cells are properly segmented in all frames of a time-lapse image sequence, and the correct associations have been established between successive frames, it is relatively easy to compute (morpho)dynamic features that may reveal biologically relevant phenomena. For example, variabilities in cell shape (within populations or per cell over time) can be very effectively studied using statistical tools such as principal component analysis (PCA) of the cell outlines [125]. Power spectrum analysis of size changes over time have revealed the presence of regularities (periodicities hinting at underlying biochemical clocks) in the membrane deformation of crawling amoebae that were not obvious from visual inspection [176]. Automated measurement of cell motility and proliferation have enabled the study of factors influencing osteoblast differentiation and growth, involved in the processes of bone formation and maintenance, as well as the dysregulation of these processes leading to osteoporosis [8]. As a final example, computerized analysis of cell velocities, directional persistence, turning frequencies, and invasion profiles, have demonstrated significant dependence of tumor cell infiltration and migration on cell type and the microenvironment, suggesting that metastasis is not a completely random phenomenon [39]. These examples clearly illustrate that computerized cell tracking not only provides objective numbers rather than subjective visual impressions, but also offers a level of sensitivity and statistical power unattainable by human observers.

2.3 From Cells to Molecules

The capacity of cells to perform their fundamental roles in living organisms is the product of a complex machinery of intracellular and intranuclear processes, involving thousands of proteins and other constructs. Spurred by the technological advances mentioned in the introduction, the quest to improve medicine is therefore increasingly focussing on acquiring a deeper understanding of these processes. In turn, this has boosted the demand for powerful image processing tools able to automatically compute the location, distribution, and dynamics of large numbers of macromolecules in (usually fluorescence) microscopy image sequences.

2.3.1 Cell Motion Correction

In biological time-lapse studies cells usually manifest themselves as highly viable objects that exhibit permanent change of position (motion), shape (deformation) and appearance (see e.g. Figure 2.2). Such complex behavior, even when the cells are segmented and tracked throughout the lifespan of the data sequence, still makes the further intracellular analysis a rather difficult task. This problem can be greatly reduced by applying a motion correction step, which separates local deformations and motions of the intracellular structures from the global motion of the cell. Formally speaking, the latter means switching from the global coordinates to the local coordinate system “frozen” in each of the cells. Transferring the data to such “frozen” coordinate system is not only a very convenient starting point for further automated intracellular analysis, but it also greatly facilitates understanding of the biological processes within the cell even by simple visual observation (see Figure 2.2).

The mentioned transformation of the coordinate system is on itself a complex task, whose main difficulty lays in the impossibility to unambiguously separate the motion and deformation [171]. The separation of the two mentioned processes is usually achieved by imposing additional constraints on them (for example, assuming the motion to be rigid, etc.). In practice, the transformation of all the segmented regions occupied by the same cell at different time points is performed via image registration. In this case, the coordinate system is fixed on the reference frame (usually the first time point at which the cell is present) and the rest of the time points are brought to that coordinate system by registering each cell’s region either to its predecessor or to the region corresponding to the reference time point.

The alignment of the two regions can be performed using any suitable image registration algorithm. The latter can be divided into two large groups: intensity-based and shape-based, named after the type of information used for performing the registration. The intensity-based methods perform alignment of two regions using image intensity or (and) features derived from it (in this case the segmentation of the regions being aligned is generally speaking not required), whereas the shape-based registration completely relies on the result of the segmentation [177]. The algorithms representing both groups were successfully applied for motion compensation in time-lapse fluorescence microscopy studies using the point-based registration scheme [100], quaternion-based registration scheme [82], demons algorithm [82,169], or thin-plate splines [99] as the final implementation. The final choice of using one or another registration method is determined by the underlying biological problem.

2.3.2 Foci Segmentation and Tracking

Fluorescent foci are a very representative example of a subject of the intracellular analysis. Indicating the presence of large concentrations of the protein that they are tagging, they can appear on the image as blobs ranging from a couple of pixels large diffraction-limited spots to huge conglomerates of proteins occupying a significant part of the cell body. Typically, foci-based analysis is performed in order to get statistical measures (e.g. total number, average size, intensity, distance to the nuclear envelope, velocity, etc.) of the foci population through the lifespan of the sequence. For example, it is known [52] how the number, appearance and spa-

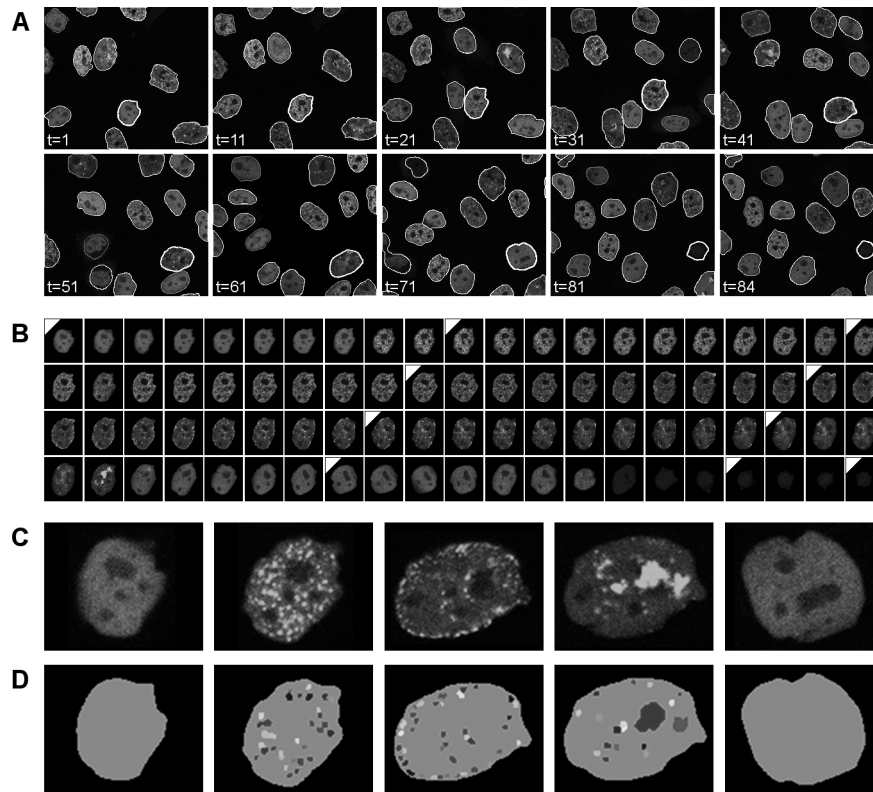


Figure. 2.2: Example of cell motion correction. (A) One cell followed through the time-lapse fluorescence microscopy image data set (outlined). During its lifetime the cell undergoes complex changes: movement, deformations, rotations, etc. (B) Cell segmentation and tracking enables extraction of each of the cells separately at every moment of time and bringing all the extracted regions occupied by the same cell to the “frozen” coordinate system by applying motion correction. Marked time points correspond to the time points shown in panel (A). In this case only the global motion of the nucleus is subtracted. (C,D) Appearance and result of segmentation of the PCNA foci for each stage of the cell cycle: G1, early-S, mid-S, late-S and G2 correspondingly (magnified).

tial distribution of the foci formed by the proliferating cell nuclear antigen (PCNA), which is involved in DNA replication, changes through the cell cycle (see Figure 2.2). Thus, being able to segment the foci and to measure all the mentioned distributions enables recognition of the cell phase, which, in its turn, might serve as a marker in further cell-cycle-related studies.

Modern fluorescence microscopy imaging techniques provide excellent opportunities for the foci-related intracellular analysis by the possibility to visualize multiple proteins simultaneously in different colors. However, similar to the cell segmentation and tracking algorithms, in practice it is necessary to develop specialized analysis tools for every particular application. For example, in fluorescence in situ hybridization (FISH) experiments [64, 83, 113, 126], the image data usually contains a low number of high-contrast foci of similar size that can be relatively easily seg-

mented. Thus the problem of “overlapping foci” is the main difficulty for quantification of such data, effective solutions for which were presented for both 2D [113] and 3D [64] cases. Particle tracking methods [138] are another example of intracellular time-lapse studies. Here, the foci are very small in size (thus called particles), so that they can only be detected rather than segmented. In many other studies, unlike the two mentioned cases, the size or appearance (or both) of the foci varies in time and between different foci in the same image.

Detection of fluorescent foci is performed by extracting peaks of the intensity profile. In case of larger-sized foci (e.g. FISH dots) this is usually achieved by applying a top-hat filter [64, 83, 113, 126]. Extracted intensity maxima are used as markers for subsequent foci segmentation. The latter is performed locally in the vicinity of each of the detected markers in order to handle closely positioned foci. The actual segmentation is achieved by thresholding, which can be applied directly [64, 126] or used as a basis for more advanced methods [83, 113]. Such approach typically results in large amount of false positives that can be removed by applying a specially built selection procedure. The location of subresolution particles is usually estimated by fitting the point-spread function of the microscope to the intensity profile. Usually, the image data containing such particles is obtained with high temporal sampling rate, which enables analysis of the foci dynamics by tracking each object separately. In this case, tracking is achieved by linking detected particles between two consecutive time points, for which probabilistic methods have proven their efficiency. Such methods allow predicting particle state (position, speed, etc.) by accumulating all available information about its previous states. This approach, in particular, allows resolving ambiguous matching situations when the trajectories of two particles intersect at a certain moment of time. The quality of tracking results is naturally strongly dependent on the temporal sampling rate of the acquired data. The choice of the latter for foci analysis is completely determined by the underlying biological application and can range from seconds to hours between two consecutive acquisitions. Smaller time intervals provide more precise tracking, allowing better estimation of foci dynamics, but higher sampling rates are restricted by the photobleaching effect [93, 142].

2.4 From Cells to Organisms

One of the major goals of biological research in our postgenomic era is to gain full understanding of the processes by which the genome directs the development of a single-cell zygote into a multicellular organism. Complete knowledge of the gene regulatory networks giving rise to specific phenotypes will dramatically advance the discovery of drugs and, ultimately, the development of clinical therapies. Model organisms such as the nematode worm *Caenorhabditis elegans* and the zebrafish are now widely used to study developmental phenomena efficiently. However, the imaging and quantification of every cell cleavage and every cell-cell interaction in an entire developing organism, as well as the phenotypical characteristics and behaviors of adult organisms, pose enormous challenges in terms of both image acquisition and image analysis [65, 79, 109, 154]. Concerning the latter, it is safe to say that such

studies constitute the ultimate test cases for automated tracking and motion analysis methods. Nevertheless, recent literature has shown first successes in the development and application of new methods for this purpose.

2.4.1 Tracking Embryogenesis

The indispensability of computational tools for studying embryogenesis quantitatively has already been recognized for some time. Interactive computer-assisted systems facilitated the segmentation, reconstruction, visualization, and motion analysis of every cell and nucleus in a developing embryo [70, 147], but required substantial manual effort in tracing and editing contours, limiting the practical use of these systems to the very early stages of embryogenesis. Automation of cell tracking in these stages is possible by applying basic image filtering techniques for cell segmentation and using spatial distance or the degree of cell overlap between image frames for cell association [65]. However, problems easily occur at later stages, due to the rapidly increasing number of cells and the cell density (Figure 2.3).

In the endeavor to track embryogenesis much further down the line, alternative methods have been developed, based on fitting spherical models for segmentation and using heuristics about the shape and size of the nuclei at the various stages of the cell cycle to disambiguate potential matches between time frames [10, 110]. The use of additional cues is of crucial importance when tracking densely packed cells through mitosis, when the telophase daughter nuclei are sent to the distal ends of the cell, and the two newborn cells may easily end up being closer to neighboring cells than to the mother cell in the previous frame. Several methods were recently developed for tracking and lineage construction of cultured cell populations [2, 90] which may also prove useful for tracking embryogenesis. In line with the foregoing sections, especially the use of contour models, motion models, and probabilistic filtering schemes [90] can be expected to add considerably to the much-needed robustness of cell tracking for this application.

2.4.2 Tracking Organism Behavior

In order to get a full picture for genotype-phenotype mapping, quantitative studies of the development of an organism from the single cell stage to maturity must be complemented by analyses of the behavioral (ab)normalities of the adult subjects. This brings us to yet another (and in this chapter final) level of spatial and temporal observation, with its own peculiarities requiring special attention (Figure 2.3). In the case of *C. elegans* tracking, on which we will focus in the sequel, a large (inter- and intra-subject) variability in appearance and behavior may be observed. For robust geometric modeling, it has been proposed [131] to make a distinction between the principal shape (the resting width-profile, length, and body orientation), and the conformation (bending patterns or curvature profiles) of the worms.

The use of standard stereo dissecting microscopes for worm tracking usually results in fairly high-contrast images, so that simple intensity thresholding can be used to segment the subjects from the background. Convenient centerline representations of the worms can then be easily obtained by applying “skeletonization”

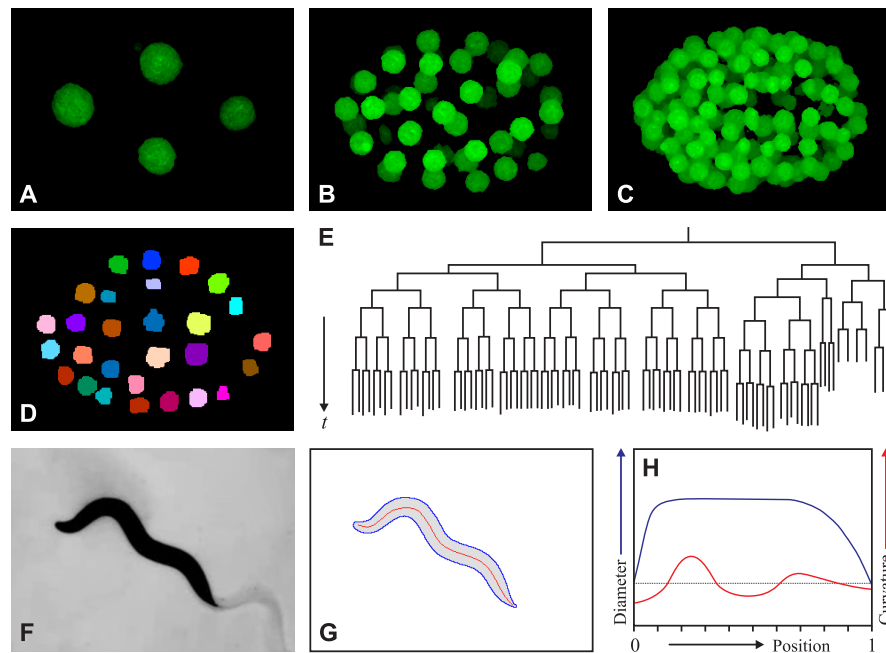


Figure. 2.3: Organism tracking. (A-C) Volume renderings of three time points (3D image stacks) from a time-lapse fluorescence microscopy data set, showing *C. elegans* embryogenesis from the four-cell stage to approximately one and two hours later, respectively. The rapidly increasing number of cells and cell density pose a real challenge for automated cell tracking. (D) Result of 3D segmentation (only one plane is shown here) obtained by applying a level-set based model-evolution algorithm and morphological postprocessing to the stack rendered in (C). (E) Tracking results can be conveniently summarized and presented (after completion or even in the process) using lineage trees, which give a clear picture of mother-daughter relations of cells, division times, and symmetry breaking events. (F) Single frame from time-lapse image data acquired using a dissecting microscope and showing the morphological and behavioral phenotypes of an adult worm. (G) Owing to the high contrast in the image, the worm body can be accurately segmented using intensity thresholding, and simple morphological operations subsequently yield the outer contour and centerline ("skeleton"). (H) Finally, a variety of morphological features, such as body diameter and curvature, can be easily computed at any position along the extracted centerline.

algorithms from mathematical morphology [31,56,73] or by using curve fitting procedures [131]. The segmentation and association tasks become more difficult, however, when studying multiple worms simultaneously for social behavior, where subject interactions, overlaps, or complex entanglements may occur. In addition, to be able to distinguish forward from backward movement, the head and tail need to be identified. Here too, similar to cell and particle tracking, the trend in the development of more robust tracking methods is in the direction of model-based and probabilistic estimation approaches [131].

2.4.3 Organism Tracking in Practice

For the presentation of the deluge of information resulting from exhaustive cell tracking during embryogenesis, cell lineage trees (Figure 2.3) can be very helpful. Such trees not only offer a convenient visual impression of mother-daughter relations of cells, they also give a clear picture of division times, (a)synchronous divisions, symmetry breaking events, and even (by color coding) of gene expression levels, for which quantitative metrics can be computed straightforwardly. However, in order for lineage related analyses to make biological sense, the reconstructed trees need to be flawless. Since a single tracking error will invalidate the entire corresponding subtree, this imposes extremely high demands on the accuracy and robustness of cell tracking algorithms. Because even state-of-the-art algorithms are not quite error-free, careful manual curation and postediting of the resulting trees will always be necessary. Several software tools for visualizing, editing, and comparing cell lineage trees are publically available [16, 18].

For the quantification of adult morphological phenotypes, geometrical features such as body length, area, thickness, symmetry, and curvature can be easily extracted upon successful segmentation [56]. As for behavioral phenotypes, *C. elegans* locomotion can be roughly classified into forward movement, backward movement, rest, and curl, the duration and change-rates of which are important parameters [73]. Automated tracking systems have been successfully used for quantifying a variety of morphological and behavioral patterns under controlled conditions (summarized in [56]). The statistical clustering of phenotypic patterns and their matching with genotypic classes and environmental conditions will yield new insights into the different mechanisms driving organism development and how to influence them beneficially.

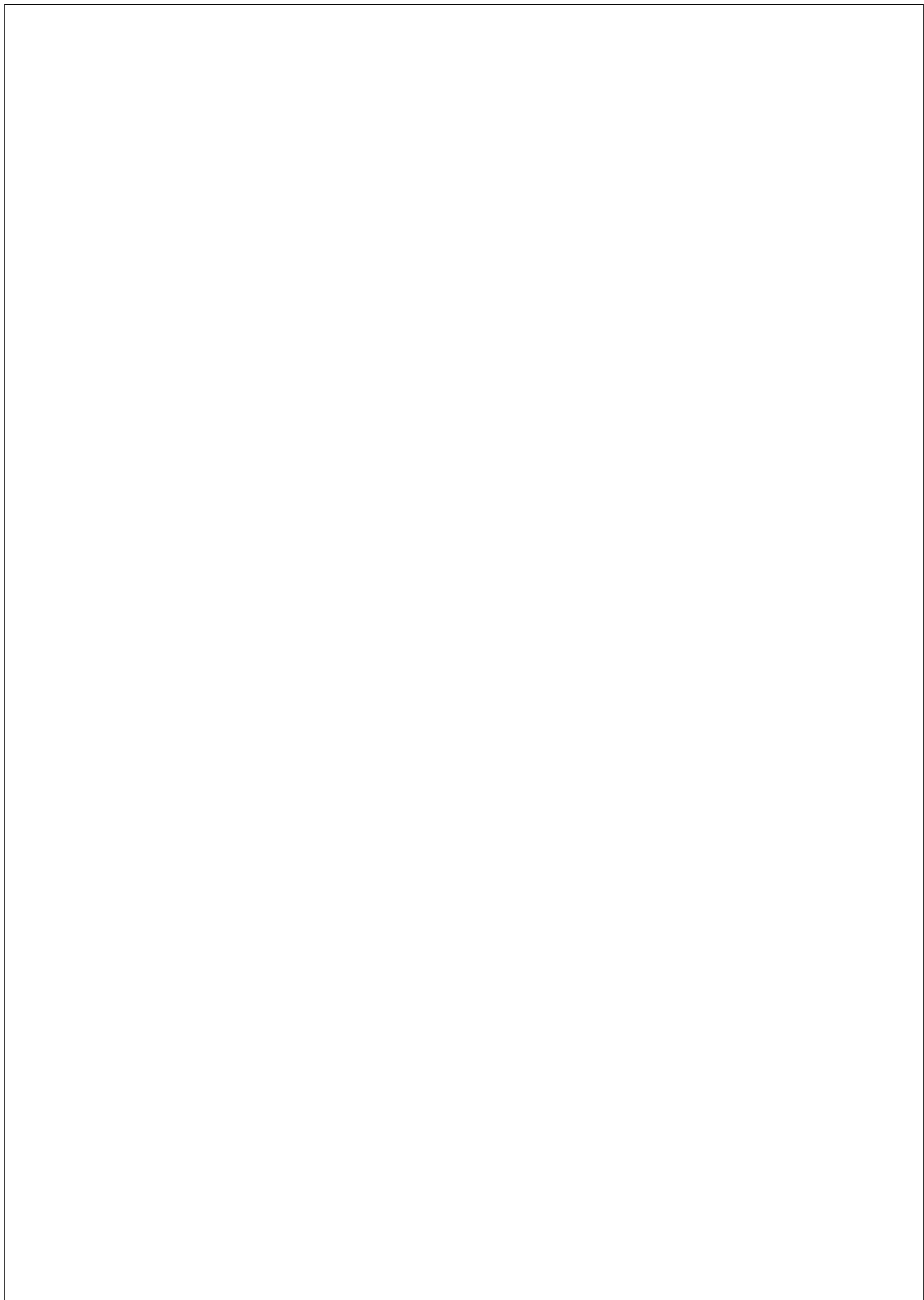
2.5 Conclusions

In concluding this chapter, we summarize the most important observations and their implications for future research. First, in view of the data explosion that is currently taking place in cell and developmental biology, it is increasingly realized that powerful software tools are now essential on the road to discovery and breakthrough. The massive change in scale of biological investigations not only calls for efficient solutions for data management, but also requires computational methods for objective and reproducible processing, analysis, and interpretation of the data. While the first challenge has already resulted in open standards for storing and sharing image and meta data, the problem of how to best automate the actual “data crunching” is still being vigorously researched by many groups worldwide, and in this chapter we have attempted to provide the reader with a good overview of recent efforts in the field to develop methods for tracking and motion analysis of objects in time-lapse microscopy image data.

Second, the exponential growth of publications in the past few years on bio-image informatics related problems is not just a testimony of the utter need for and the development of computational tools, but also of the fact that the field is still very much in an exploratory phase. The general conclusion emerging from the cur-

rent body of literature seems to be that there are no universal solutions to tracking problems in cell and developmental biology, and that tools pretending the existence of such solutions (such as many commercial software packages) generally show mediocre performance. This is understandable by realizing that, especially in developmental experiments, one must be concerned with the analysis of events at the molecular level (nanometer scale), the cellular level (micrometer scale), up to the organism level (millimeter scale), that is at least six orders of spatial (not to mention temporal) detail, each with its own idiosyncrasies. However, the advent of whole-body scanners for fluorescence and bioluminescence tomography imaging, and the desire to be able to quantify (sub)cellular processes within intact organisms, will push the demand for integrated methods capable of tracking motion at all relevant scales simultaneously. Currently, several trends can be observed in the development of new tracking methods, including the increasing use of models (of object shape and dynamics as well as image formation) and probabilistic (Bayesian) estimation methods, which are known from other fields to yield improved robustness.

Finally, since every specific tracking problem currently requires its own dedicated solutions to optimally extract and exploit the information contained in the data, investigators are constantly faced with the challenge to develop their own software tools. This is increasingly possible, even for users without expertise in computer programming, by means of commercial and open-source tools facilitating the assembly of existing image processing algorithms and the integration of custom-designed algorithms. However, biology has by now unquestionably developed into a multidisciplinary field, and it seems that the joint optimization of all aspects of biological experimentation (sample preparation, image acquisition, image analysis, data modeling, and statistics) is best achieved by a close collaboration between biologists, chemists, physicists, mathematicians, statisticians, as well as computer scientists, all the way from experiment planning to the ultimate interpretation of the results. Academic environments and research programs fostering this collaboration will likely prove to be the main contributors to progress in biology.



Advanced Level-Set Based Cell Tracking in Time-Lapse Fluorescence Microscopy

3

Abstract — Cell segmentation and tracking in time-lapse fluorescence microscopy images is a task of fundamental importance in many biological studies on cell migration and proliferation. In recent years, level sets have been shown to provide a very appropriate framework for this purpose, as they are well suited to capture topological changes occurring during mitosis, and they easily extend to higher-dimensional image data. This model evolution approach has also been extended to deal with many cells concurrently. Notwithstanding its high potential, the multiple-level-set method suffers from a number of shortcomings, which limit its applicability to a larger variety of cell biological imaging studies. In this chapter we propose several modifications and extensions to the coupled-active-surfaces algorithm, which considerably improve its robustness and applicability. Our algorithm was validated by comparing it to the original algorithm and two other cell segmentation algorithms. For the evaluation, four real fluorescence microscopy image data sets were used, involving different cell types and labelings that are representative of a large range of biological experiments. Improved tracking performance in terms of precision (up to 11 percent), recall (up to 8 percent), ability to correctly capture all cell division events, and computation time (up to 9 times reduction) is achieved.

Based upon: O. Dzyubachyk, W. A. van Cappellen, J. Essers, W. J. Niessen, E. Meijering Advanced Level-Set Based Cell Tracking in Time-Lapse Fluorescence Microscopy. *IEEE Transactions on Medical Imaging*, vol. 29, no. 3, March 2010, pp. 852–867.

3.1 Introduction

Many cell biological studies rely on the analysis of large cell populations by means of microscopy imaging [30, 42, 50, 123, 163, 176]. Especially when the goal is to (also) study intracellular phenomena, fluorescence (confocal) microscopy is often used for such studies, as it allows biologists to perform live cell experiments with high sensitivity and specificity [122, 142, 151, 156]. The earliest applications of cell tracking included the fields of immunobiology and hematopoiesis, answering questions of how stem cells, progenitor cells and various leukocyte subtypes migrate throughout the body, and how their states of differentiation and activation vary depending upon their location or interaction with each other and, in the case of immune cells, with antigen and antigen presenting cells [158]. Nowadays, tracking techniques are applied to a variety of cell types, including tumor cells [117, 149, 159], embryonic stem cells [10], endothelial and epithelial cells [80]. Time-lapse studies of live cells have aimed at studying cell migration, cell cycle [115, 149, 159] and growth control [117], proliferation [2, 10, 90], adhesion [80], and many other functions, under various conditions.

Analyses of cell populations as a whole provide information about average cell characteristics and (morpho)dynamic behavior. The ability to perform analyses on individual cells would not only refine that information, but also enable detection of rare events, which can lead to better understanding of the cell's functionality. In many of the applications, the identification of each cell and the precise delineation of its boundaries are tasks of equal importance. The complexity of performing these tasks is increasing with growing size of the image data being analyzed. Manual processing of such data is not only subjective (possibly biased) and error prone, it is also very laborious and in many cases simply impossible, creating a strong demand for automated techniques.

The use of fluorescence microscopy for live cell analysis poses a number of additional challenges to automated segmentation and tracking. First, the variety of fluorescent proteins and labeling techniques used in practice for different experiments leads to considerable differences in the appearance of cells in the images (Figure 3.1 shows some typical examples of fluorescent microscopy images where different labelings were used). Second, the intensities of the fluorophores (and their distribution) may change over time during an experiment, and may temporarily even disappear completely. Third, since cells are sensitive to photodamage, the (laser) light intensity needed to excite the fluorescent proteins is often reduced to a minimum, leading to very low signal-to-noise ratios (SNR) [104, 142]. Fourth, for the same reason, the temporal and spatial sampling rates are often reduced as well, sometimes causing large jumps from one frame to the next. Fifth, fluorescence microscopy images may contain autofluorescence [98], interfering with the signal of interest. Sixth, in the case of 3D imaging over time, the characteristics of the system (point-spread function) are different for slices close to the coverslip compared to slices situated deeper in the specimen [59]. Finally, the usage of any classic computer vision tracking methods for this application would be hampered by the necessity to also track dividing targets.

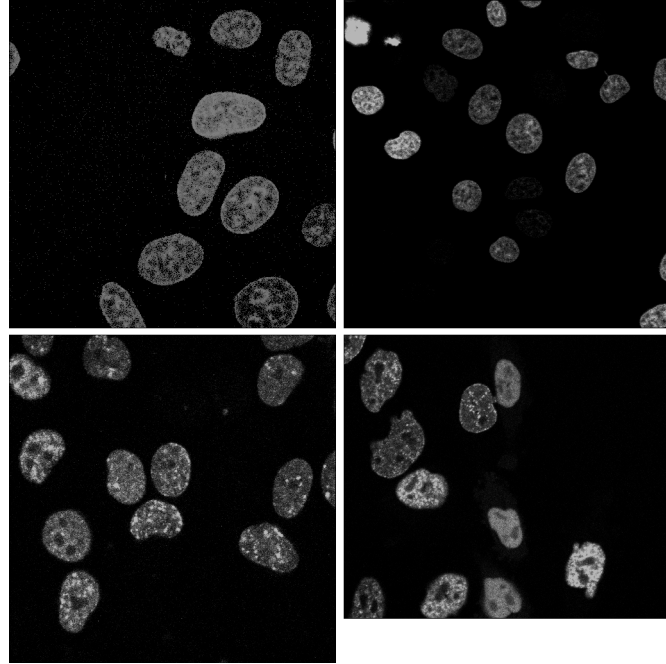


Figure 3.1: Sample images from the data sets used in this study. From top-left to bottom-right: Hoechst-labeled HeLa cells, H2B-GFP labeled HeLa cells, RAD18-YFP labeled HeLa cells, and PCNA-GFP labeled CHO cells (see Section 3.4 for abbreviations and experimental details).

3.1.1 Related Work

Over the past decade, a number of cell tracking algorithms have been developed. These algorithms concentrate on a variety of cell types, and are based on different visual tracking methods. In general, they can be divided into two categories, with respect to the tracking paradigm being used. The first consists of algorithms based on the “first detect, then track” principle. These algorithms first perform detection of all cells in the whole image sequence and then establish links between detected cells from frame to frame based on certain criteria. Examples of such algorithms include [2, 27, 68, 116, 168, 170]. The main characteristic of this approach is its computational efficiency with respect to segmentation, but the algorithms often encounter problems during the temporal data association stage [133]. Especially, this is the case for tracking data with high cell densities, large numbers of cell division events, and cells entering and leaving the imaging frame, i.e. when it is difficult to determine the exact number of interacting cells in the current frame [81, 139, 140, 164]. Every case where one-to-many or many-to-one correspondence is established requires a special treatment procedure for splitting or merging some of the tracks. Usually such cases are resolved by using information from the adjacent frame(s). Development of an efficient splitting/merging procedure often requires training on large numbers of features, thus making such approach inconvenient in practice. Another weakness of

this type of algorithms is that during the segmentation step, usually no information about the segmentation of previous frames is used.

The second category of algorithms uses an integrated segmentation and tracking scheme, which, when combined with contour models, is often referred to as the *model evolution approach* [176]. The idea behind this type of tracking is that for each object a model is created that describes the object being tracked. In this case, segmentation and tracking are performed simultaneously by fitting the model to the image data and using the end result in one frame as the starting point for segmentation in the next frame. One example of this type of tracking is the mean-shift process [36], which works well in case of tracking cells of known shape showing relatively small displacements between frames. Another option for the model is active contours, which in the past few years became the first choice for model evolution based cell tracking [41, 44, 107, 115]. In practice, active contours can be implemented explicitly, via a parametrization (e.g. snakes), or implicitly, using the level set framework. Active contours can in principle perform tracking on any type of cell image sequences, but they can also be tailored to a specific application by putting, for example, size or shape constraints.

The main advantage of the model evolution approach is that each object being tracked preserves its identity, and events changing the total number of objects (mitosis, apoptosis, cells entering or leaving the frame) can be handled more easily. The other advantage is that all available information from the previous time step can be directly incorporated into the segmentation of the current image frame. This leads to much more realistic results in comparison to algorithms based on separated segmentation and tracking. The main drawback of the model evolution approach is that it is often rather expensive from a computational point of view. In addition, each type of model used within this framework has its own pros and cons (in Section 3.3 we will elaborate on these for the case of coupled active surfaces).

Finally, we mention one important subclass of algorithms within the model evolution approach paradigm. In probabilistic contour tracking algorithms, presented e.g. in [135] and [153], the Bayesian framework is used to complement the active contours method. The idea behind this type of algorithms applied to cell tracking is that they try to predict in a probabilistic way the global motion of the object and its characteristic parameters. To this end, the Kalman filter or related methods (e.g. particle filters) can be used. In this case, the deformation of the tracked object is assumed to be small, which, unfortunately, does not hold for dividing cells. To our knowledge, none of the existing probabilistic contour tracking methods is able to deal with such cases, which strongly limits their application to cell tracking.

3.1.2 Our Method

In this chapter we present a considerably extended version of the cell tracking algorithm that was previously presented at a conference [48], which in turn is based on the coupled active surfaces framework [44, 111, 175]. Specifically, we modify the original algorithm to make cell segmentation and tracking both faster and more robust. The modifications concern most of the shortcomings of the original algorithm, such as its sensitivity to the energy weights and how it handles (initially) touching cells,

and cells entering the observation frame. Also, we suggest several improvements for implementation of the algorithm, and perform an extensive evaluation.

Our algorithm is based on the model evolution approach. Level sets were chosen for the model because of their ability to segment objects of varying intensity and shape, to handle topological changes naturally, and to deal with both 2D and 3D image sequences. In our algorithm, each level-set function represents one object (cell or nucleus), and the evolution equation for each level-set function is derived using the variational approach, replacing the original weights from the energy functional by more meaningful parameters that can be computed automatically from the data. The initial position of the level-set function in any frame is its final position in the previous frame. In the first frame, the initial position is found via segmentation with one level-set function and splitting the function according to the number of connected components. Since this step is crucial for further tracking, and the single-level-set approach tends to lump closely positioned cells together, we apply the watershed transform to refine the results. To improve the separation of level-set functions corresponding to closely positioned cells, we apply the Radon transform, which “decouples” the active surfaces by means of separating planes, making it possible to apply the stopping criterion to each level-set function separately. The efficiency of the algorithm is improved by introducing a new stopping criterion. Also, we incorporate a modified non-PDE based energy minimization scheme, which suggests a different way of treating the image-based and the smoothness-based energy terms. To further speed-up this scheme, we approximate contour length using the so-called cut metric. In addition, we suggest a different way of detecting cells entering the observation frame. Finally, we perform more economical recomputation of the algorithm’s parameters.

3.1.3 Chapter Outline

The remainder of this chapter is organized as follows. First, in Section 3.2, we give an overview of the coupled active surface framework, which constitutes the basis of our algorithm. Next, in Section 3.3, we present our advanced cell segmentation and tracking algorithm, and discuss in detail the modifications compared to the original algorithm. The performance of our algorithm in comparison with the original algorithm and two publicly available specialized software packages was evaluated on four real biological image data sets obtained with different fluorescent labelings and/or cell types. The experimental setups and results are presented in Section 3.4. Finally, the main conclusions following from our work are summarized in Section 3.5.

3.2 Segmentation With Coupled Active Surfaces

In this section we provide a brief overview of the tracking algorithm by Dufour *et al.* [44], which is an extension of the classical segmentation algorithm of Chan and Vese [23]. This framework was chosen as the starting point for the development of our algorithm because for our opinion it is the most elegant and promising method

for simultaneous cell segmentation and tracking currently available. It is based on the level-set representation, which makes it easily extendable from the original formulation in 2D to 3D and, if necessary, to higher dimensions. The energy functional for the 3D case is

$$E(S, c_I, c_O) = \iint_S \alpha g dS + \lambda_I \iiint_{\text{inside}(S)} (I - c_I)^2 dx dy dz + \lambda_O \iiint_{\text{outside}(S)} (I - c_O)^2 dx dy dz, \quad (3.1)$$

where S is the set of surfaces defining the image partition, c_I and c_O are scalar variables related to average intensities inside and outside S , $I = I(x, y, z; \tau)$ is the image intensity at time τ at location $(x, y, z) \in \Omega$, with $\Omega \subset \mathbb{R}^3$ the image domain, and α , λ_I , and λ_O are fixed weights. The use of function g allows accounting for possible presence of edge information.

Representing the set of surfaces S as the zero-level of a three-dimensional embedding function, we arrive at the following implicit formula for S :

$$S = \phi^{-1}(0) = \{(x, y, z) \in \Omega \mid \phi(x, y, z) = 0\}, \quad (3.2)$$

where ϕ is the scalar level-set function defined on Ω and index “-1” denotes function inversion. We define ϕ such that $\phi > 0$ inside the surfaces and $\phi < 0$ outside the surfaces. The representation (3.2) allows us to rewrite the energy functional (3.1) in terms of the level-set function ϕ :

$$E(\phi, c_I, c_O) = \iiint_{\Omega} \left[\alpha g \delta_{\epsilon}(\phi) |\nabla \phi| + \lambda_I H_{\epsilon}(\phi) (I - c_I)^2 + \lambda_O (1 - H_{\epsilon}(\phi)) (I - c_O)^2 \right] dx dy dz, \quad (3.3)$$

where H_{ϵ} and δ_{ϵ} are the regularized Heaviside and the regularized Dirac function, respectively. Applying to (3.3) the Euler-Lagrange equation, we derive the following evolution equation for the function ϕ :

$$\frac{\partial \phi}{\partial t} = \delta_{\epsilon}(\phi) \left[\alpha g \nabla \cdot \frac{\nabla \phi}{|\nabla \phi|} + \alpha \nabla g \cdot \frac{\nabla \phi}{|\nabla \phi|} - \lambda_I (I - c_I)^2 + \lambda_O (I - c_O)^2 \right], \quad (3.4)$$

where t is an artificial (evolution) time parameter. The Euler-Lagrange equation for the parameters c_I and c_O can be directly solved, resulting in those parameters being equal to the average intensity of the voxels outside and inside the active surface, respectively (corresponding expressions can be found in [23]).

In order to be able to track each cell separately, the concept of multiple coupled active surfaces is introduced [44]. The tracking algorithm is based on assigning one level-set function, ϕ_i , to each cell, $i = 1, \dots, n$. Disregarding the cases of dividing cells and cells entering or leaving the observation frame makes it possible to keep the number of level-set functions n fixed during segmentation of the current frame.

Going from one frame to the next, all biological events that may change the number of cells are handled after the frame is segmented, leading to disappearance of existing level-set functions or to creation of new ones. Defining the background as $\Omega_0 = \{(x, y, z) \mid \phi_i(x, y, z) < 0, \forall i = 1, \dots, n\}$ we write the total energy of the set of functions ϕ_i as

$$E(\phi_1, \dots, \phi_n, c_O, c_{I,1}, \dots, c_{I,n}) = \iiint_{\Omega} \sum_{i=1}^n \left[\alpha g \delta_{\varepsilon}(\phi_i) |\nabla \phi_i| + \lambda_I H_{\varepsilon}(\phi_i) (I - c_{I,i})^2 \right. \\ \left. + \frac{\lambda_O}{n} \prod_{j=1}^n (1 - H_{\varepsilon}(\phi_j)) (I - c_O)^2 + \gamma \sum_{i < j} H_{\varepsilon}(\phi_i) H_{\varepsilon}(\phi_j) \right] dx dy dz, \quad (3.5)$$

which amounts to the sum of energies (3.3) plus a coupling term weighted by γ . The purpose of the coupling term is to minimize the pair-wise intersections of the interiors of active surfaces. Applying to (3.5) the Euler-Lagrange equation, we obtain the mean values c_O and $c_{I,i}$ for each level-set function (for analytical expressions see [44]) and the equivalent of the evolution equation (3.4):

$$\frac{\partial \phi_i}{\partial t} = \delta_{\varepsilon}(\phi_i) \left[\alpha g \nabla \cdot \frac{\nabla \phi_i}{|\nabla \phi_i|} + \alpha \nabla g \cdot \frac{\nabla \phi_i}{|\nabla \phi_i|} - \lambda_I (I - c_{I,i})^2 \right. \\ \left. + \lambda_O \prod_{j \neq i} (1 - H_{\varepsilon}(\phi_j)) (I - c_O)^2 - \gamma \sum_{j \neq i} H_{\varepsilon}(\phi_j) \right]. \quad (3.6)$$

Using the above concepts, we can summarize the main steps of the tracking algorithm as follows:

1. Segment the first frame with one level set using the algorithm of Chan and Vese [23] and determine the number of connected components n .
2. Assign one level-set function, ϕ_i , to each component, $i = 1, \dots, n$, and set it to the signed distance function of the boundaries of the component.
3. Evolve each level-set function according to (3.6) updating c_O and $c_{I,i}$ every iteration (until convergence).
4. Determine whether existing level-set functions need to be terminated or new functions introduced.
5. If there is a next frame, pass the converged level-set functions on to that frame and go to Step 3).

The algorithm inherits the strong points of the level-set framework, namely the ability to segment objects of strongly varying intensity and shape, and to handle changes in topology. However, the level-set formulation has a number of shortcomings, which limit the algorithm's performance.

One of the problems that makes this framework inconvenient to use in practice is its dependence on the weighting parameters α , λ_O , $\lambda_{I,i}$, and γ . Since these lack

physical meaning, the only way to obtain sensible values for them is by trial and error. But even then, the problem remains that the performance of the algorithm is very sensitive to these weights, requiring very careful tuning to each new data set. Another drawback of any level-set framework, and hence of this tracking algorithm, is that it is computationally very expensive. To our knowledge, no good criterion for stopping the curve evolution process has been suggested in the literature. The convergence speed is also strongly influenced by good initialization and by re-initialization of the level set to the signed distance function for preventing numerical instabilities. The final difficulty that we encountered is not related to the level-set framework as such, but to the considered algorithm [44]: even though the algorithm was able to separate closely positioned cells, the resulting separating surfaces were not always biologically correct (see Figure 3.9 for illustration).

3.3 Proposed Algorithm

In this section we present our level-set based segmentation and tracking algorithm in detail. We start (Section 3.3.1) with an outline of the general flow of the algorithm. Then we describe all the different aspects of the algorithm, for which we propose new approaches. These include non-PDE based energy minimization for obtaining a good initial segmentation (Section 3.3.2), separation of initially touching cells (Section 3.3.3), handling cell division events (Section 3.3.4), the stopping criterion (Section 3.3.5), a new “internal” energy of the level-set function (Section 3.3.6), separation of closely positioned or even touching cells (Section 3.3.7), re-initialization of the level sets (Section 3.3.8), and detection of cells entering the observation frame (Section 3.3.9).

3.3.1 Algorithm Outline

The general flow of our cell tracking algorithm is similar to that described in the previous section. The improvements that we introduce in the original algorithm can be classified into two parts: 1) related to the quality of segmentation and tracking, and 2) related to the performance of the algorithm in terms of computation time. Some of the changes have strong impact on both issues.

Our algorithm is based on the representation of every object of interest by its own level-set function. Their positions in the first frame are determined by segmenting the frame using one level-set function by the method of Rousson and Deriche [132]. Non-PDE based energy minimization (Section 3.3.2) is used to obtain a good initialization, which significantly reduces the computation time. The watershed segmentation algorithm combined with the flood-level threshold (Section 3.3.3) is used to separate initially touching cells and to extract connected components from the image segmented using one level-set function. For each of the n detected components, a level-set function, ϕ_i , is created. Optimal segmentation of the current frame

is then obtained by minimizing

$$E(\phi_1, \dots, \phi_n) = \sum_{i=0}^n \iiint_{\Omega_i} -\log P(I(\mathbf{x})|\Omega_i) dx dy dz + \alpha \cdot \text{Length}(\partial\Omega), \quad (3.7)$$

where Ω_0 is the background, $\Omega_i = \{\mathbf{x} | \phi_i(\mathbf{x}) > 0\}$, $i = 1, \dots, n$, are the regions such that $\Omega = \bigcup_{i=0}^n \Omega_i$, $\partial\Omega$ is the boundary between regions, $P(I(\mathbf{x})|\Omega_i)$ is the conditional probability that voxel $\mathbf{x} = (x, y, z)$ with intensity $I(\mathbf{x})$ belongs to the region Ω_i [120]. We assume here that this distribution is Gaussian (Section 3.3.6). Notice that here we use a region-based formulation of the coupled active surfaces framework only, since when experimenting with the region-based formulation on real biological data, we did not observe any improvement of quality of the results in comparison with using both region- and boundary-based formulations. Using the multiple level-set representation we rewrite (3.7) as

$$\begin{aligned} E(\phi_1, \dots, \phi_n) = & \iiint_{\Omega} \sum_{i=1}^n \left[\alpha \delta_{\epsilon}(\phi_i) |\nabla \phi_i| \right. \\ & \left. + H_{\epsilon}(\phi_i) e_{1,i} + \frac{1}{n} \prod_{j=1}^n (1 - H_{\epsilon}(\phi_j)) e_0 \right] dx dy dz, \end{aligned} \quad (3.8)$$

which is equivalent to (3.5) for the case of modified "internal" energies $e_0(\mathbf{x})$ and $e_{1,i}(\mathbf{x})$ (Section 3.3.6) and absent coupling term. Applying to (3.8) the Euler-Lagrange equation, we derive the evolution equation for each level-set function:

$$\frac{\partial \phi_i}{\partial t} = \delta_{\epsilon}(\phi_i) \left[\alpha \nabla \cdot \frac{\nabla \phi_i}{|\nabla \phi_i|} + \prod_{j \neq i} (1 - H_{\epsilon}(\phi_j)) e_0 - e_{1,i} \right]. \quad (3.9)$$

Every level-set function ϕ_i evolves according to (3.9), starting from its initial position, which is defined as the result of segmentation using one level-set function (for the first frame) or the final result of the segmentation of the previous frame (for the second and subsequent frames). Evolution stops when the convergence condition is met (Section 3.3.5), which is applied to each level-set function separately, independently of the other $n - 1$ level-set functions.

The number of the level-set functions remains constant during the tracking procedure, unless cells divide (Section 3.3.4), or when cells leave or enter the observation frame (Section 3.3.9). The first two events are treated at the end of segmentation process of each frame, after all the level-set functions have converged. The cells entering the frame, however, require a special detection procedure.

In summary, our algorithm consists of the following steps, refining those of the original algorithm (Section 3.2):

1. Segment the first frame with one level set using the algorithm of Rousson and Deriche [132], using non-PDE based segmentation as initialization (Section 3.3.2), and watersheds to separate initially touching cells and extract n connected components (Section 3.3.3).

2. Create one level-set function, ϕ_i , for each component, $i = 1, \dots, n$, and set it to the signed distance function of the boundaries of the component.
3. Only for mitotic cells in case DNA-bound staining is used: check if the corresponding cell has divided (Section 3.3.4). If true, extend the active contour to capture both daughter cells and recompute the narrow band.
4. Find the first level set ϕ_i in the queue for which the stopping criterion (Section 3.3.5) does not hold, otherwise skip to Step 7).
5. Calculate the energies $e_{1,i}$ and e_0 (Section 3.3.6), and evolve ϕ_i during n_i iterations according to (3.9) within a narrow band around the zero-level, while applying separation masks to functions whose zero-levels come into close contact (Section 3.3.7).
6. Re-initialize ϕ_i to the signed distance function (Section 3.3.8) and recompute the narrow band, then move ϕ_i to the end of the queue and go to Step 4).
7. Determine which level-set functions correspond to dividing or leaving cells, or whether new cells are entering the observation frame, and take proper actions on the level sets (Section 3.3.9).
8. If there is a next frame, pass the converged level-set functions on to that frame and go to Step 4).

3.3.2 Non-PDE Based Energy Minimization

The non-PDE based energy minimization algorithm of Song [141] is a simple and efficient technique for image segmentation if the image consists of only two classes ("foreground" and "background"). The idea behind this scheme is to start from an initial partition and see what happens if each of the voxels changes its label from "foreground" to "background" and vice versa. This relabeling is performed only if it decreases the total energy, and generally produces partitions close to the optimal, especially for images with a small amount of noise. In [44], it has been used during the segmentation of the first frame using a single level-set function. The result of the non-PDE based energy minimization is then used as a good initialization for the level-set evolution.

The main problem of this non-PDE based scheme is the way it acts on smoothness- and image-based energy terms. The image-based energy term is much easier to incorporate into this scheme. Moreover, it is possible to prove theoretically that, if only the image-based term is used, the scheme converges under certain conditions. Including the smoothness-based term, however, often leads to very slow convergence, thus drastically reducing the biggest advantage of this scheme: its speed. On the contrary, running the algorithm without this term produces very undesirable results, strongly influenced by the noise level. The reason is that in this case, every voxel with intensity differing from the background intensity will most likely be labeled as part of the foreground. Another problem when using both energy terms together is the need to use the weight α , which strongly influences the final

result and currently can be determined only experimentally (automatic calculation of the optimal value of α is the subject of ongoing research). In order to overcome these problems, the two energy terms are often treated separately. In the original algorithm [44], the non-PDE based scheme is executed in two steps: 1) without the smoothness-based term (for a few iterations only), and after that 2) with that term (also for a few iterations only).

In our algorithm we use a slightly different approach. Within one iteration, we first relabel voxels using only image-based energy, and after that we perform relabeling using the smoothness-based energy term only. If necessary, the second relabeling can be performed more than one time. This approach has the advantage that, instead of setting a predefined number of iterations, here it is possible to establish convergence. Moreover, by treating two energy terms of different nature separately, as proposed, we avoid the need of using the parameter α . Notice that in these calculations, we are also using different region statistics compared to the original algorithm, thus a different image-based energy term (Section 3.3.6). The expressions that are used to calculate the energy differences, together with their derivation, can be found in our earlier conference report [47].

An additional modification that we used for this scheme concerns the computation of the smoothness-based energy term. In the original scheme [141], this energy term was approximated by finite differences on the grid.

In order to reduce the number of operations required to calculate the smoothness-based energy, we suggest using the cut metric introduced by Boykov and Kolmogorov [15]. This metric is based on the Cauchy-Crofton formula, which relates the Euclidean length of a plane curve \mathcal{C} to the number of straight lines that \mathcal{C} crosses. Thus we can write down the following approximation for the Euclidean length of curve \mathcal{C} on the grid:

$$|\mathcal{C}|_{\mathcal{E}} = \sum_{k=1}^{n_G} n_c(k) \cdot w_k, \quad w_k = \frac{\delta_G^2 \cdot \Delta \varphi_k}{2 \cdot |e_k|}, \quad (3.10)$$

where $n_c(k)$ is the number of lines belonging to the family of edge lines that \mathcal{C} crosses, n_G is the total number of lines in the family, $|e_k|$ is the length of the k -th line in the family, $\Delta \varphi_k$ is the angle between lines k and $k+1$, and δ_G is the distance between the nodes of the grid. Since the value of w_k depends only on the chosen family of edge lines and hence is known in advance, the only parameter in (3.10) that depends on curve \mathcal{C} is $n_c(k)$, which can be easily calculated. This idea can be directly extended to the 3D case [15].

3.3.3 Separation of Initially Touching Cells

As mentioned in Section 3.2, the total number of level-set functions remains constant if no cell division occurs and no cells enter or leave the observation frame. Thus, in order to perform correct cell tracking, it is vitally important to have a good segmentation of the first frame. This requirement is not always fulfilled when cells are positioned close to each other or touch. The level-set based segmentation tends to lump such cells together. Fully automated separation of such cells is hardly possible,

since there is no obvious automatic way to distinguish between a cell with unusual appearance and two cells lumped together.

For data sets containing such cases, we apply the watershed segmentation to the level-set function obtained from the pre-segmentation of the initial frame with one level-set function. This approach has the advantage that except for separating lumped cells, it also extracts the connected components, which is necessary for the tracking algorithm. It is well known that the classical watershed segmentation often produces oversegmentation. One of the possible ways to correct this is to use, for example, marker-controlled watersheds [170]. Our approach to this problem is to use region merging based on the flood-level threshold (sometimes referred to as the H-minima transform) [126].

3.3.4 Capturing Cell Division

In addition to cells that (nearly) touch each other, we found that cell division events form another important source of tracking errors, especially for level-set based tracking algorithms that use narrow-banding. In practice it often happens that the temporal sampling rate is rather low (for reasons described in the introduction). In such cases, particularly when DNA-bound labeling is used (which implies that the images of the cell nuclei become very condensed during division), the distance between the mother nucleus in one frame and the two daughter nuclei in the next frame may be too large for the tracking algorithm to make the correct association, as there is no overlap between the initial contour and the final region to be detected by the corresponding level-set function (Figure 3.2). This phenomenon is a problem when using the narrow-banding technique: if a cell (or nucleus) in a next frame is not covered by at least a part of the narrow band of the corresponding level-set function from the previous frame, it will not be segmented. Moreover, even if the narrow band is wide enough to intersect with the expected object region, this case also requires evolution of the corresponding level-set without re-initialization, until the moment when its zero-level contour captures a part of the cell. In practice these two issues seriously limit the performance of the tracking algorithm on the data with DNA-bound labeling. It has to be pointed out that usage of such data for biological research is quite common: two out of four data sets selected for the validation of this algorithm (Hoechst and H2B-GFP; see Section 3.4.1) were of this type.

To overcome this difficulty, we used the following strategy based on the typical appearance of the mitotic and after-mitotic cells under DNA-bound labeling (Figure 3.5). More specifically, mitotic cells in this case were detected by the decreased total volume and pronounced elongated shape (Figure 3.2). Analyzing the intensity profile in the direction perpendicular to the major axis we can identify the division events as the moment when this profile becomes essentially bimodal in the region of interest. Thus, we extend the corresponding cell region in such a way that it includes both peaks of the mentioned bimodal profile. In practice the latter can be easily performed by rising the corresponding level-set function by adding to it a positive constant (illustrated in Figure 3.2). Using this method, our algorithm was able to correctly handle almost all cell divisions in the experiments (Table 3.2 in Section 3.4.4).

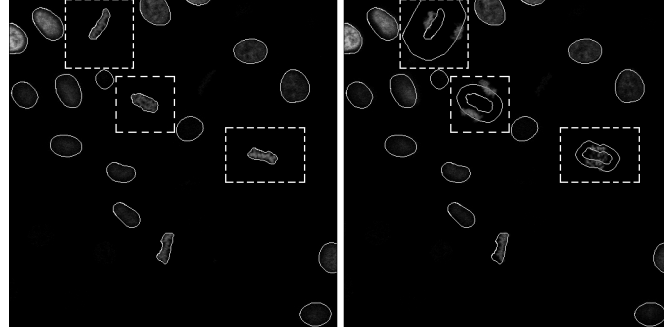


Figure 3.2: Example of cell division at low temporal sampling. Two successive frames of a sequence are shown. The first (left image) shows three mitotic cells (indicated by the dashed rectangles) that are about to divide. Segmentation results for this frame are also shown (overlaid white contours). The next frame (right image) shows the telophase daughter nuclei right after division. For reference, the segmentation results for the previous frame are also overlaid here (white contours), as they are the initial contours of the level-set functions for this frame. Since there is no overlap between these contours and the daughter nuclei, the latter will not be segmented. Extending the contours as shown (described in Section 3.3.4) yielded the correct segmentation in all three cases.

3.3.5 Stopping Criterion

A good stopping criterion is an important component of every level-set based algorithm. Being able to determine the moment at which the zero-level of the level-set function effectively stops changing is very important, as it allows avoiding unnecessary computations. Few practical solutions to this problem are available in the specialized literature. Most implementations use a maximum number of iterations as a stopping criterion. Alternatively, it has been proposed to use the rate of change of the contour length during iteration as an indicator for stopping or continuing [25]. If, after a required minimum number of iterations, this rate is less than some prescribed value, the convergence condition is met.

In practice it turns out that the latter approach has a number of drawbacks. One of them is that it is rather sensitive to the limiting value for the rate of change of the contour length. The optimal value for this parameter has to be tuned for every image data set separately. Another inconvenience concerns the use of a minimal number of iterations after which the stopping criterion is applied. This condition seems to be rather artificial, as there are no mathematical or physical reasons for using it. Since the mentioned condition is based on the curve length, the length has to be recomputed every iteration, which slows down the algorithm.

Our solution to the problem is to check the rate of sign change by every voxel, and to use that information for deciding to continue or to stop evolving the level set. This criterion is very convenient when using the narrow banding technique, since in this case only the voxels inside the narrow band have to be considered. In practice, we are using not the whole narrow band, but exclude from it one layer of voxels

closest to the contour, on both sides (motivated below). Every change of the voxel's sign means that this voxel changes its label from "foreground" to "background" or vice versa. For each of the evolving level sets, the stopping criterion is established as follows: if during a prescribed number of iterations, n_{conv} , the total number of sign changes by all voxels in the "cropped" narrow band does not exceed the given value, n_ϵ , the process stops. In practice, even for $n_\epsilon = 0$, the criterion is met quite quickly for typical numbers of iterations, $n_{conv} = 40$.

The need to exclude the layers of voxels closest to the contour from the narrow band is dictated by practical reasons. Analyzing the behavior of the contour close to its final position, we found that for the voxels belonging to the layers adjacent to the noisy object's boundary it is not always possible to determine whether they belong to the object or to the background. Consequently, such voxels tend to change their label constantly between object and background, which is the reason to disregard them.

3.3.6 Internal Energy

One of the issues that makes the original level-set framework of Chan and Vese [23] problematic in use is its sensitivity to the energy weights α , λ_O , and λ_I . Different values of these parameters may produce very different segmentations, and there is no good way to calculate these weights in advance, thus requiring tuning to each application. To tackle this problem, we used the approach of Rousson and Deriche [132], which gives physical meaning to the weights λ_O and λ_I , if we make the reasonable assumption that the intensity distributions of each object and of the background are Gaussian:

$$\begin{aligned} P(I|\Omega_0) &= \frac{1}{(2\pi)^{d/2}\sigma_O} \exp\left(-\frac{(I - c_O)^2}{2\sigma_O^2}\right), \\ P(I|\Omega_i) &= \frac{1}{(2\pi)^{d/2}\sigma_{I,i}} \exp\left(-\frac{(I - c_{I,i})^2}{2\sigma_{I,i}^2}\right). \end{aligned} \quad (3.11)$$

In these equations, c_O , σ_O^2 , $c_{I,i}$ and $\sigma_{I,i}^2$ are the intensity means and variances of the corresponding regions, and d is the number of image dimensions. Consequently, the internal energy of the background e_0 and that of each object $e_{1,i}$ are (up to a constant) defined as the negative logarithm of (3.11):

$$\begin{aligned} e_0 &= \log(\sigma_O^2) + \frac{(I - c_O)^2}{\sigma_O^2}, \\ e_{1,i} &= \log(\sigma_{I,i}^2) + \frac{(I - c_{I,i})^2}{\sigma_{I,i}^2}. \end{aligned} \quad (3.12)$$

From (3.12) it turns out that under these assumptions, λ_O and λ_I are inversely proportional to the intensity variances of the corresponding regions. For the segmentation algorithm, this is a great advantage, since, instead of tuning the energy weights

λ_O and λ_I , it was shown in [132] that the Euler-Lagrange equation for the variances can now be solved directly.

Another advantage of this approach reveals itself when tracking cells with varying intensities between frames (Figure 3.5), as well as between individual cells within one frame (Figure 3.1). The original scheme (3.6), which contains a constant weight λ_O for the background and a constant weight λ_I (one for all level sets), is not always able to find the desired energy minimum. In case of using the approach from [132], instead of the energy weights one now deals with the background variance σ_O^2 and the variances $\sigma_{I,i}^2$ of each cell being tracked. These variances are updated in a similar way to c_O and $c_{I,i}$, which considerably improves the quality of segmentation under strongly varying foreground and background intensity distributions.

The internal energies of the objects, $e_{1,i}$, and of the background, e_0 , should, in principle, be re-evaluated after each iteration, which is computationally expensive. It has been proposed [44] to avoid re-evaluation of these energies, by assuming the corresponding intensity distributions of the objects and of the background to be equal to the ones obtained from the previous frame, implying that the energies will also be equal to the ones calculated from the segmentation result of the previous frame. In order to improve the algorithm's performance, we suggest to assume the image-based energy of each level set to be constant during a number of iterations, n_i (usually $n_i = 20$ to 40 iterations). This allows to perform the surface evolution during n_i iterations with only recomputing the smoothness-based energy.

3.3.7 Separation of Touching Cells

The problem of properly separating closely positioned objects is one of the most difficult issues in automated cell tracking. Therefore, some authors have proposed manual or semi-automatic solutions [101], but the challenge remains to find fully automated solutions. In [44], the repulsive coupling term was used to prevent the positive parts of different active surfaces from overlapping. Since this term is not based on the image data, it does not favor any particular position of the separating surface. This often leads to incorrect segmentation of touching objects, especially in the case when their movement is relatively large (for example see Figures 3.9A and 3.9B). In order to account for this, a volume conservation constraint was introduced [44], which improves the object separation but, unfortunately, this also does not solve the problem completely. We observed that incorporating this constraint into the cell tracking algorithm decreases its performance because of two reasons. The main reason is that this constraint is quite strong, meaning that the assumption that a cell's (imaged) volume remains approximately constant does not always hold. Especially this is not true in 3D, since usually only a few slices are imaged, not covering the whole cell. If the cell moves in the vertical direction, the volume constraint will most likely be violated. The other reason is that this constraint does not hold for dividing cells. Detecting the moment when a cell starts dividing is problematic when using the volume conservation constraint, since volume change is often indicative of mitosis.

In our algorithm we use a different strategy. It is based on the observation that the boundary between touching cells usually can be approximated by a straight line

(or a plane in 3D). In this case, the Radon transform is a natural choice for locating the exact position of the separating surface. Originally this idea was suggested for segmenting mammospheres [66]. Our version of this idea consists of two main steps. First, we calculate the Radon transform for each pair of closely located objects (the latter are detected by overlapping narrow bands). The position of the optimal separating plane (line in 2D case) corresponds to a local minimum of the Radon transform. This minimum is automatically found based on certain criteria (see below). Next, we constrain the evolution of the level-set functions corresponding to the two objects to the regions on either side of this separating plane.

The Radon transform of a function [34] gives values of its projections along the various planes:

$$R_0(\rho, \varphi, \theta) = \iiint f(x, y, z) \delta_R(\mathbf{x}; \rho, \varphi, \theta) dx dy dz, \quad (3.13)$$

where

$$\delta_R = \delta(\rho - x \cos \varphi \cos \theta - y \sin \varphi \cos \theta - z \sin \theta), \quad (3.14)$$

ρ is the shortest distance from the origin to the plane, φ is the azimuth around the z axis, and θ is the elevation angle around the y axis. Applying (3.13) to the image intensity $I(\mathbf{x})$, we find the correct local minimum of the function

$$R(\rho, \varphi, \theta) = \frac{\iiint I(x, y, z) \delta_R(x, y, z; \rho, \varphi, \theta) dx dy dz}{\iiint \delta_R(x, y, z; \rho, \varphi, \theta) dx dy dz}, \quad (3.15)$$

as the plane separating two seeds (we used the centers of the two objects). In addition, information about the position of the optimal separating plane from the previous frame is used for limiting the set of feasible solutions. The Radon transform is applied only locally, for each pair of closely positioned cells, and is calculated within the window containing two regions currently occupied by them. In addition, each object's region is extended with a band a couple of voxels wide around it, in order to account for possible cell movement. Restricting the calculation of the Radon transform to a small window also has a positive impact on the computation time. We calculate the separating plane for each pair of closely positioned cells only once, using the current states of their active surfaces. It is done either before segmentation of the frame if the corresponding objects are already in contact, or at a later stage, as the cells come close to each other. Since in this case we are not performing the separation of the final regions occupied by the cells in the given frame, but of the current ones, this approach can be regarded only as an approximation. Nevertheless, it is valid when cell movement is relatively small compared to its size.

The next step after the optimal separating plane is found is to create a "mask", m_i , for each object, $i = 1, \dots, n$. This mask defines the image part in which the corresponding level-set function is allowed to evolve (Figure 3.3). In cases where there are more than two cells close to each other, we apply the Radon-transform based separation for every pair of these cells. The mask for any object in these cases is obtained as the intersection of all the masks found for that object.

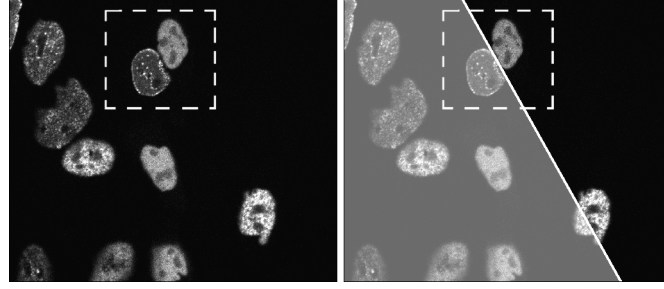


Figure 3.3: Two closely positioned cells separated using the Radon transform. The transform is computed in a small region around the two cells (indicated by the dashed rectangles in the images), and a separating plane is obtained by finding the correct local minimum in the transform, which is used to construct evolution masks for the level-set functions corresponding to the two cells (one mask is shown as a shaded area in the right image).

Finally, we point out one more benefit of searching for the separating surface in the form of a plane. Namely, since a plane can be easily parameterized, there is no need to store the mask as a binary image in memory. Instead, only the coefficients of the separating plane are stored, from which the mask can be easily recomputed at any moment when needed. This is especially advantageous when dealing with large images containing large number of cells.

3.3.8 Re-Initialization of the Level Sets

Re-initialization of each level-set function after a number of iterations is necessary to prevent numerical instabilities. There are two main approaches to re-initialization. The approach of Osher and Fedkiw [114] suggests using a special kind of differential equation. In order to solve that equation, the gradient descent method is used. Another approach is to use the distance transform [84]. This is often favored, as it is faster than the one based on the differential equation: it uses only two passes through the image to calculate the whole distance transform. Since in practice all 3D microscopy images have an axial resolution that is different from the in-plane resolution, we use the weighted distance transform [137].

3.3.9 Capturing Entering Cells

Cases of cells entering the observation frame require special attention, since they can strongly influence the tracking result. For example, when a cell enters the frame close to an existing one, it may cause the level-set function of the existing cell to engulf the newcomer. Another problem is that if an entered cell is not properly assigned to a corresponding level set function, it will be considered part of the background, which can drastically change the background statistics and lead to incorrect segmentation results.

To deal with entering cells, it has been suggested [44] to use an additional level-set function located at the boundaries of the frame, to capture cells crossing these

boundaries. However, with this approach, problems may occur around existing cells that are already located at the boundary. The level-set function that targets entering cells may capture parts of existing cells as well, producing incorrect segmentations, and causing two parts of the same cell to be represented by multiple level set functions (illustrated in Figure 3.9). The errors propagate and deteriorate in subsequent frames. Moreover, we noticed that dividing cells sometimes leave the observation frame via the upper boundary, and enter it again at a later stage. Using an additional level-set function is absolutely undesirable for detection of cells entering the frame from the top, since often almost all cells are actually located at the upper boundary.

Our alternative strategy for the detection of entering cells is the following. After the current frame has been segmented without taking entering cells into consideration, non-PDE based segmentation (Section 3.3.2) is applied to determine possible “candidates” for entering cells. The candidates are those connected components that i) are located at the boundary of the image (including, if necessary, the upper boundary) and ii) do not intersect with any of the existing cells. For each candidate, a level-set function is created, and the level-set segmentation process is started again from the current positions of the level sets. Since the level sets of all cells except the “newcomers” have already converged, this process takes relatively short time to complete.

3.4 Experimental Results

The proposed level-set based cell segmentation and tracking algorithm was compared to the original algorithm by evaluation on real fluorescence microscopy image data sets acquired for different biological studies. Here we first describe the data sets (Section 3.4.1) and the algorithm parameter settings used in the experiments (Section 3.4.2). Then we present the experiments and the results, which demonstrate the improved performance of the proposed algorithm in terms of segmentation quality (Section 3.4.3), tracking quality (Section 3.4.4), and computation time (Section 3.4.5).

3.4.1 Image Data Sets

Four raw 3D time-lapse fluorescence microscopy image data sets were selected by expert biologists to evaluate the proposed algorithm under different experimental conditions. The data sets were chosen to be representative of data acquired in everyday biological imaging practice, each of them containing a single layer of cells. All images were acquired with a Zeiss LSM-510 laser-scanning confocal microscope. A summary of the features and microscope settings for acquiring each of the four data sets is given in Table 3.1. A sample image from each of the data sets is shown in Figure 3.1.

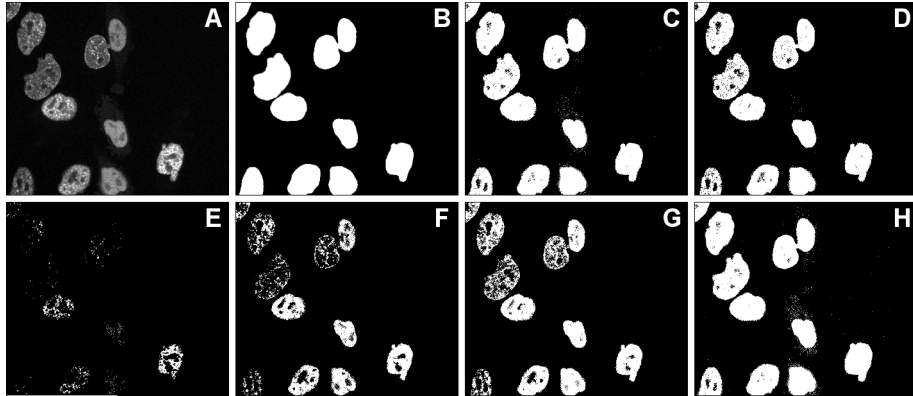


Figure. 3.4: Comparison of segmentation quality on the test image (A) between our algorithm (B) and a number of commonly used thresholding algorithms: (C) Huang's, (D) Li's, (E) Kapur-Sahoo-Wong's (Maximum Entropy), (F) Tsai's, (G) Otsu's, and (H) Yen's [134]. The chosen test image is the first slice ($z = 1$) of the first stack from the PCNA-GFP sequence.

The main cause of difference in appearance of cells in fluorescence microscopy images is the type of labeling used. Each data set was made using a different type of labeling, resulting in cell appearance of different complexity for automated cell segmentation and tracking. The first, Hoechst (in this case we used Hoechst 33342), is harmful for cells when excited, especially at the optimal UV-wavelength of 360 nm . Therefore, we used 2-photon excitation (with a Ti:Sapphire laser of coherent light) at 800 nm and kept the Hoechst concentration and the laser power as low as possible, leading to noisy images (Figure 3.5). In the second data set [53], we used H2B-GFP labeling (green fluorescent protein linked to one of the histone types that form the protein backbone around which the DNA winds). Histone-2B is expressed quite high in most cells and therefore yields a somewhat higher SNR. However, during mitosis, the H2B-GFP shows the equatorial plate of condensed chromosomes, which has a completely different appearance than the staining patterns seen during interphase (the time between cell divisions), and makes tracking during mitosis quite different and more difficult (Figure 3.5). In the third and fourth data set, we used RAD18-YFP (yellow fluorescent protein linked to RAD18 proteins) and PCNA-GFP (green fluorescent protein linked to "proliferating cell nuclear antigens" proteins) labeling, respectively. RAD18 is a DNA-binding protein involved in postreplication repair of UV-damaged DNA, while PCNA has a role in DNA synthesis, DNA repair, and cell cycle progression [52]. The labeling patterns of RAD18 and PCNA are quite different: the former starts with a few foci in G1-phase, many foci in the S-phase and early G2-phase, and nucleolar staining in the late G2-phase (Figure 3.5), while PCNA forms clear foci during the S-phase but is more or less homogeneous during both the G1- and G2-phase. These time-varying labeling patterns make automated segmentation and tracking very challenging (Figure 3.4 and Figure 3.5).

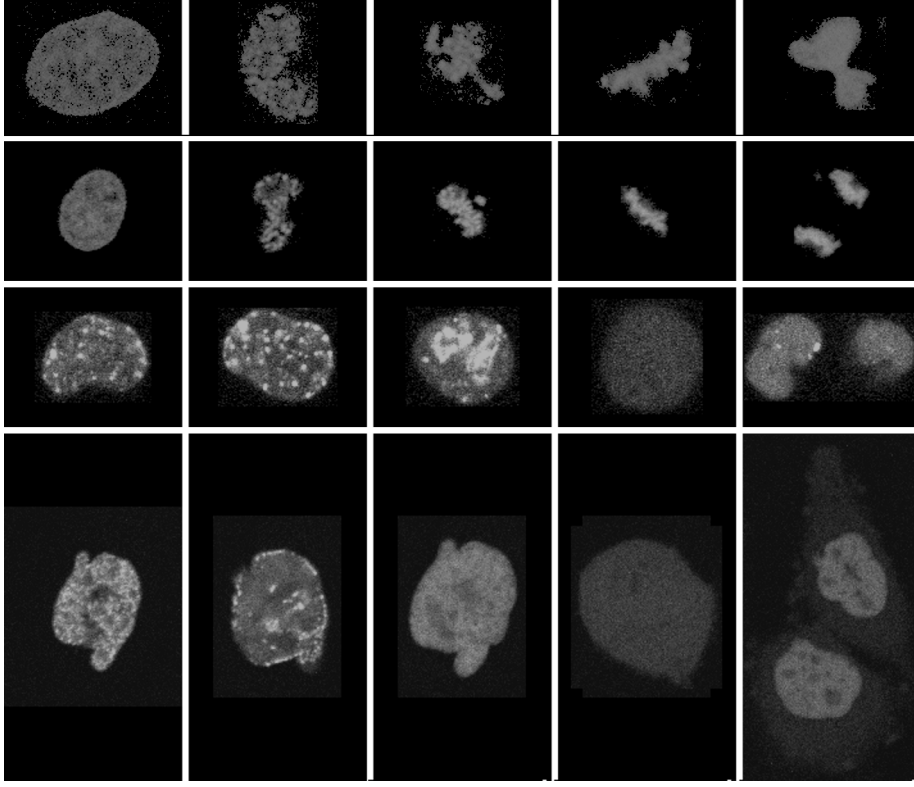


Figure. 3.5: Typical appearance of the nuclei through the cell cycle under different staining: Hoecht (first row), H2B-GFP (second row), RAD18-YFP (third row) and PCNA-GFP (fourth row). These images clearly indicate the difficulty connected with tracking mitosis events caused by dramatic change of nuclei shape and intensity during cell division.

3.4.2 Algorithm Parameter Settings

For all data sets, the parameters of our proposed algorithm (Section 3.3) were fixed to the following values: $\alpha = 20$, $n_i = 40$, $n_{conv} = 40$, $n_\epsilon = 0$. The parameters of the other algorithms used in the evaluations were optimized to obtain the best possible results per data set. We note that this may positively bias the results of the latter algorithms relative to our algorithm, but at the same time it allows us to further demonstrate the improved robustness of our algorithm. For the original level-set based segmentation and tracking algorithm [44] we experimentally determined the following parameter values: $\alpha = 20$ (weight of the smoothness-based term), $\eta = 0.001$ (weight of the volume conservation constraint), and γ differing per data set (ranging from 20 to 100) to obtain optimal results. The parameters λ_1 and λ_2 were chosen as the inverse values of the foreground and background intensity variances in the first frame, which yields the optimal segmentation of this frame in case these intensities are normally distributed. Since for using the volume constraint this

algorithm requires knowledge of whether a cell is dividing or not at the given time point, this information was provided in advance, before the algorithm was executed. For both algorithms, the evolution time step was fixed to $\Delta t = 0.1$.

3.4.3 Segmentation Evaluation

Since ground-truth segmentations were not available for the data sets, the segmentation results of both algorithms were compared with manual segmentations by four expert human observers. Whereas the algorithms segmented and tracked all data sets completely, manual segmentation of all data would be an extremely laborious and time-consuming task. Therefore, we restricted the manual segmentations (and thus the comparisons) to 10 randomly selected images (slices) per data set. Due to the randomness of image selection, all temporal positions (time frames) of the sequences, as well as all depth positions (slices), were more or less equally represented in the experiments.

A reference segmentation for each image was calculated from the manual segmentations using the STAPLE algorithm [161]. The reference segmentations also allowed us to calculate estimates for the local SNR per object in each of the four test data sets. The average SNR for each of the images is shown in Figure 3.6. Here, SNR is defined as the ratio of the difference between the mean intensity of the foreground and of the background to the standard deviation of intensity in the foreground region, which is appropriate in our case of signal-dependent (Poisson) noise [22, 26].

For further comparison, we have also chosen two publicly available specialized software packages: CellProfiler [21, 85] and DCellIQ (based on [88, 160]). Both packages were created for performing high-throughput/high-content screening of cell populations, involving cell segmentation (CellProfiler) or both cell segmentation and cell tracking (DCellIQ). The drawback of these software packages is that they are essentially 2D, which limits the value of any comparisons with our algorithm. Nevertheless, it does give an impression of the relative segmentation performance of our algorithm in 2D, even though our algorithm operates in 3D.

Precision (or positive predictive value) and recall (or sensitivity) are two common measures for evaluating the quality of results [3, 152]. Let X denote the segmentation result by one of the considered methods and let Y be the ground truth. The precision and recall are defined as

$$precision = \frac{|X \cap Y|}{|X|}, \quad recall = \frac{|X \cap Y|}{|Y|}. \quad (3.16)$$

These can be combined into a single measure of performance, by taking the harmonic mean, resulting in the F -score:

$$F = \frac{2 \cdot precision \cdot recall}{precision + recall}. \quad (3.17)$$

Precision and recall values for the four expert human observers were obtained from the STAPLE algorithm.

Table. 3.1: Microscope settings used for obtaining the test data sets.

Feature	Data Set 1	Data Set 2	Data Set 3	Data Set 4
Labeling	Hoechst	H2B-GFP	RAD18-YFP	PCNA-GFP
Cell type	HeLa	HeLa	HeLa	CHO
Objective	Plan-Neofluar 10 \times /0.3	Plan-Apochromat 63 \times /1.4 Oil DIC	Plan-Apochromat 63 \times /1.4 Oil	Plan-Apochromat 63 \times /1.4 Oil
Stack size (voxels)	512 \times 512 \times 6	512 \times 512 \times 6	512 \times 512 \times 6	512 \times 443 \times 5
Stack size (μm)	97.5 \times 97.5 \times 5.0	146.25 \times 146.55 \times 5.0	97.5 \times 97.5 \times 5.0	103.4 \times 89.5 \times 4.0
Number of stacks	85	82	50	92

Table. 3.2: Tracking performance of our algorithm (DZ09) and the original algorithm (DUF05).

Data set	Precision		Recall		Number of Sequences	Divisions		False Divisions	
	DUF05	DZ09	DUF05	DZ09		DUF05	DZ09	DUF05	DZ09
Hoechst	90.6 %	99.7 %	98.7 %	99.8 %	11	14 / 21	19 / 21	15	2
H2B-GFP	91.6 %	100.0 %	94.7 %	100.0 %	21	60 / 80	80 / 80	141	4
RAD18-YFP	88.5 %	97.1 %	85.5 %	93.8 %	4	16 / 23	23 / 23	8	1
PCNA-GFP	87.8 %	99.1 %	92.8 %	98.5 %	5	17 / 25	24 / 25	10	2

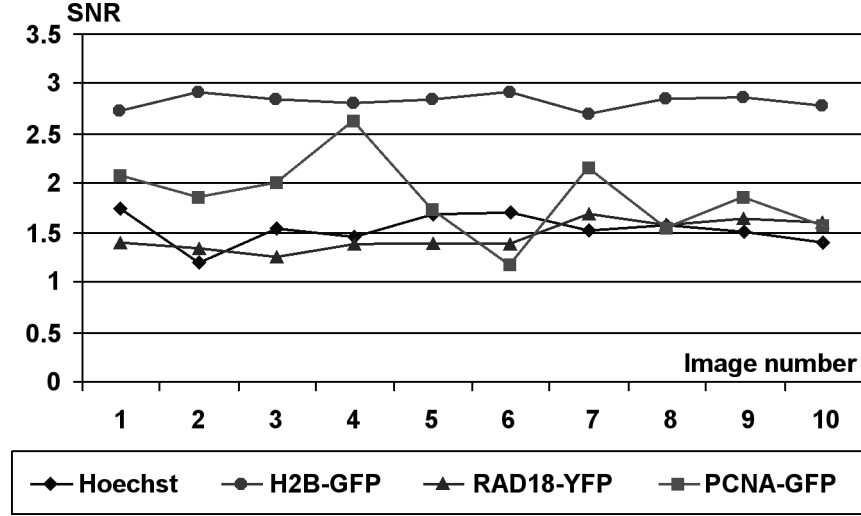


Figure. 3.6: Average SNRs within the 10 test images selected randomly from each of the four data sets. The profiles give an impression of the behavior over time of the SNR in the data sets, caused by the time-varying appearance of the fluorescent labels.

The segmentation performance of each of the methods and four human observers in terms of the precision and recall is shown in Figure 3.8, where our algorithm is denoted as “DZ09” and the original algorithm on which it is based as “DUF05”. Several important observations can be made here. First, the quality of segmentation is strongly correlated with SNR (compare Figure 3.6). Second, the original algorithm (DUF05) has the tendency to show decreased performance closer to the end of the sequences (recall that in the graphs the images are sorted such that increasing image numbers correspond to increasing time). Third, the performance of our algorithm (DZ09), contrary to the original (DUF05), remains fairly constant throughout the sequences and is mostly dependent on the SNR. Fourth, for all four image sequences, our algorithm shows a segmentation quality that is better than or comparable to the other three methods. The only exception here is the PCNA-GFP data set, where for images 5 and 10 our method performed worse than CellProfiler and DCellIQ. This is likely a consequence of the fact that the appearance of the PCNA-GFP data set varies strongly between slices, which negatively affected our 3D segmentation in comparison with the 2D methods. Nevertheless, the overall performance of our method is superior, which was confirmed by using a paired Student t -test. For all four test data sets the mean F -score of our algorithm was higher than that of the other three algorithms. For all four data sets the significance level of the performance improvement was $p < 0.1$, except for CellProfiler on the H2B-GFP ($p < 0.2$) and the PCNA-GFP ($p < 0.38$) sequences and DCellIQ on the PCNA-GFP ($p < 0.33$) sequence. In particular, comparing only the DZ09 and DUF05 algorithms, we obtained the significance level $p < 0.02$ for all four test sequences.

In addition, we tested all four algorithms on presence of systematic bias. This was done by using a similar measure to the bias index [20], which is the measure

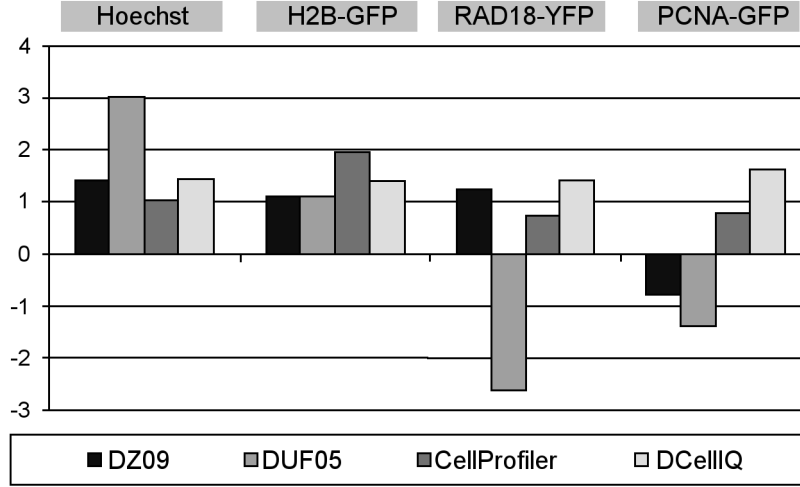


Figure. 3.7: Average bias of the four considered methods on four test data sets.

that is commonly used in epidemiology. We define the bias index for a single object as

$$BI_{object} = \frac{|X \cap Y^C| - |Y \cap X^C|}{|\Omega|}, \quad (3.18)$$

where the letter "C" next to the region's name denotes its complement, and the sets X , Y and Ω were described earlier in the text. In order to obtain a meaningful measure for performance of a particular method on the given data set, we divide its average bias index by the average bias index of all four observers on all objects of this data set:

$$BI_{method} = \frac{\text{sign}(BI_{objects}) \cdot \text{mean}(|BI_{objects}|)}{\text{mean}(|BI_{objects,observers}|)}. \quad (3.19)$$

The sign factor in the last formula was used for indication of the oversegmentation ($BI > 0$) or undersegmentation ($BI < 0$). Here we restricted ourselves only with those objects for which at least one pixel was segmented by all four methods. The result of the systematic bias analysis is shown in Figure 3.7. From this figure we can observe that the maximal absolute bias value of our method is less than 1.5, which is comparable with the average bias rate of four human observers. The maximal absolute bias value for the DCellIQ algorithm is close to ours (approximately 1.6), while for the DUF05 and the CellProfiler methods this value is relatively higher (3.0 and 1.9 respectively). Also it can be observed that the DCellIQ and the CellProfiler algorithms tend to oversegment objects in all four test data sets, while our method and the original one show more balanced performance.

3.4.4 Tracking Evaluation

For estimation of the tracking performance, two expert biologists independently checked all the results of both our algorithm and the original algorithm, by carefully scrolling through the data sets with the tracking results overlaid as color-coded regions. In this process, they visually detected false positives or negatives, and false or missed cell divisions. From these observations, the following three quantitative measures of tracking performance were obtained:

- *Tracking accuracy*: The quality of cell identification over time in terms of precision and recall, defined as (3.16), but now with a different meaning of variables X and Y : here, the ground truth Y is the presence or absence of a cell in current frame (a binary variable), while X is the tracking result ("true" if the active contour of interest covered the corresponding cell region, or a part of it, and "false" otherwise). The average precision and recall rates over all time frames were calculated.
- *Number of true divisions*: The number of division events in which both daughter cells (nuclei) were correctly identified and associated with the mother cell (nucleus), relative to the real number of divisions.
- *Number of false divisions*: The number of cases in which two cells (nuclei) were incorrectly associated with one cell (nucleus) in the previous frame.

In order to perform better validation of cell division events the corresponding measures were tested on a larger number of image sequences from the four data sets mentioned above: Hoechst (11), H2B-GFP (21), PCNA-GFP (5) and RAD18-YFP (4). For performing this kind of analysis, whenever it was necessary to determine the precise moment of cell division, the biologists also used the transmission channel images that were recorded along with the fluorescence images. The tracking results of the original algorithm and our proposed algorithm are listed in Table 3.2. The numbers clearly indicate the superiority of our method for all data sets and for all criteria. The false divisions in the results of our algorithm are mostly caused by mitotic cell breaking up or by rare events in the vicinity of the existing cell: the presence of an apoptotic cell or a new cell entering the observation frame. The somewhat lower recall value of our algorithm (93.8 %) for the RAD18-YFP data set can be explained by the typical division pattern of cells stained that way: a couple of frames before and after division, the fluorescence can be observed all over the cytoplasm and is no longer concentrated in the nucleus. Consequently, our method tends to separate the daughter cells from each other with a delay of a couple of frames, thus lowering their recall rate (see Figure 3.10). The very high false division rate for the DUF05 algorithm for the H2B-GFP sequence can be explained by considerable cell movement between consecutive frames and by the high variation of the intensity distribution within the cell which results in level-set function segmenting intracellular structures rather than the cell body. Though some part of these division errors might potentially be corrected by putting additional constraints on divided cells, it was not done here in order to demonstrate the robustness of our algorithm with respect to handling cell division events.

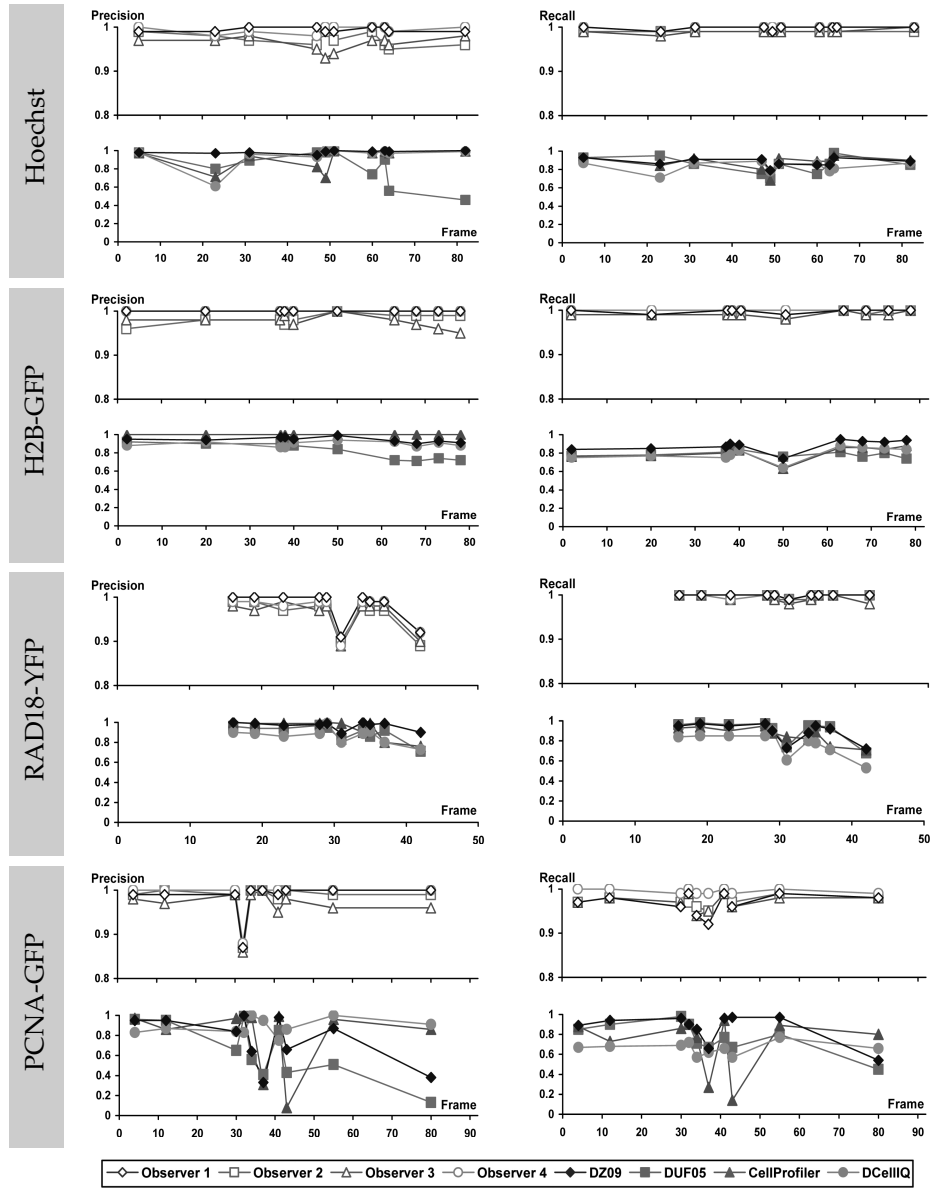


Figure. 3.8: Average precision and recall values showing the segmentation performance of four human observers and the four methods: our algorithm (DZ09), the original level-set based algorithm (DUF05), CellProfiler, and DCellIQ. The scores are shown for a subset of 10 images selected from the four different image data sets: Hoechst (first row), H2B-GFP (second row), RAD18-YFP (third row), and PCNA-GFP (fourth row).

Table. 3.3: Computation times (in hh:mm) of both algorithms.

Method	Hoechst	H2B-GFP	RAD18-YFP	PCNA-GFP
DUF05	21:37	17:53	11:02	13:19
DZ09	2:26	2:24	2:12	2:38

The improved tracking and segmentation quality of our algorithm in comparison with the original algorithm is illustrated with a number of examples in Figure 3.9. Some cases when our algorithm fails to produce the optimal results are shown in Figure 3.10.

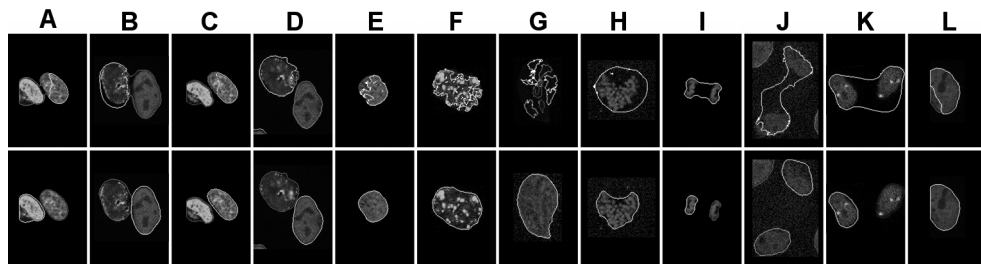


Figure. 3.9: Typical examples of errors produced by the original multiple-level-set tracking algorithm (top row) in comparison with improved performance by our modified algorithm (bottom row): (A,B) incorrect separation of two touching cells; (C,D) contour splitting as a result of such incorrect separation (this may lead to detection of cell division that in reality did not occur); (E,F) incorrect segmentation of objects with complex foreground intensity distribution; (G) the same, which leads to breaking of the contour into a number of sub-contours segmenting intracellular structures instead of the whole nucleus; (H) disability to handle rapid shape change; (I–K) difficulty with properly handling the correct moment of cell division, which may cause a significant delay of detection of this event; (L) incorrect identification of a part of an existent object located at image's boundary as a new object.

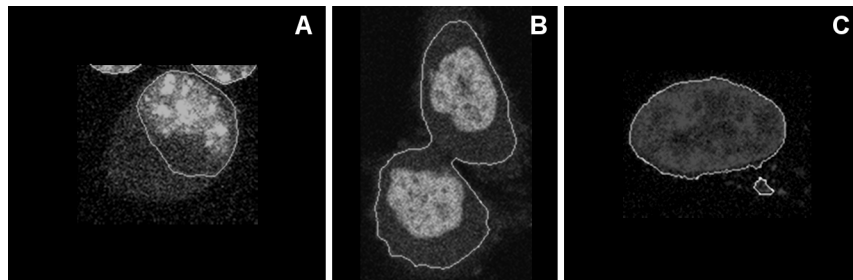


Figure. 3.10: Typical examples of segmentation and tracking errors produced by our algorithm: (A) incorrect segmentation after rapid change of objects's shape and contrast (correct segmentation was recovered after the next time step); (B) delayed detection of cell division event (separation of daughter nuclei); (C) false cell division event due to rare event (appeared apoptotic cell) in the vicinity of the object.

3.4.5 Computation Time

Both the original and our proposed algorithm were implemented in the same experimental programming environment (Matlab version R14). This allows for a fair comparison of computation times. Both algorithms were implemented in a similar fashion and optimized from the programming perspective. In addition, the modifications introduced in Section 3.3 enabled the incorporation of several simplifications in our algorithm (approximation of the regularized Heaviside function, re-initialization limited to the region of interest, etc.), which significantly reduced computational times. The times required by the algorithms to segment and track each data set are given in Table 3.3. These numbers show a reduction in execution time of 5 to almost 9 times when using our algorithm. We note that further optimization of the code is still possible, as well as conversion to a faster programming or even hardware environment [86]. While this will likely reduce the required absolute computation times by a considerable amount, our proposed algorithm will remain substantially faster than the original algorithm. In general, the main factors that influence the total computation time of our algorithm are: number and size of cells (approximately linear dependence), amount of cell clustering, and SNR of the processed data.

3.5 Conclusions

In this chapter we have presented an advanced algorithm for multi-cell segmentation and tracking, based on the coupled active surfaces framework. A number of shortcomings of the original algorithm were discussed, and new solutions proposed. These concerned the segmentation and tracking accuracy, robustness, and computational cost. Specifically, we redefined the energy functional to be minimized, thereby reducing the number of energy weights. Also, we introduced the use of the Radon transform for improved separation of touching cells. To obtain a better segmentation of the first frame, which is crucial to avoid initial error propagation, we incorporated the watershed algorithm. In addition, we developed improved schemes for capturing cell division events and cells entering the observation frame. Finally, a number of implementational improvements were proposed, to make the algorithm computationally faster, or more accurate, or both. These include an efficient criterion for stopping the level-set evolution process, a modified non-PDE based energy minimization algorithm, the use of the cut metric for computing the smoothness-based energy term, and the weighted distance transform for regular re-initialization of the active surfaces. Evaluation experiments were performed on four time-lapse fluorescence microscopy image data sets, where different cell types and/or labelings were used, so as to be representative of a large variety of biological experiments. The results clearly showed the improved tracking performance of our new algorithm, with improved precision (up to 11 percent) and recall (up to 8 percent), as well as perfect detection of true positive cell divisions, and reduced false positive detections. Finally, the new algorithm was found to be computationally much more efficient (up to 9 times faster).

Automated Analysis of Time-Lapse Fluorescence Microscopy Images: From Live Cell Images to Intracellular Foci

4

Abstract — Complete, accurate, and reproducible analysis of intracellular foci from fluorescence microscopy image sequences of live cells requires full automation of all processing steps involved: cell segmentation and tracking followed by foci segmentation and pattern analysis. Integrated systems for this purpose are lacking. Extending the work in cell segmentation and tracking presented in the previous chapter, a new system for performing fully automated analysis of fluorescent foci in single cells was developed. The system was validated by applying it to two common tasks: intracellular foci counting (in DNA damage repair experiments) and cell phase identification based on foci pattern analysis (in DNA replication experiments). Experimental results show that the system performs comparably to expert human observers. Thus, it may replace tedious manual analyses for the considered tasks, and enables high-content screening. The described system was implemented in MATLAB (The MathWorks, Inc., USA) and compiled to run as a stand-alone program. It is publicly released, free of charge for non-commercial use.

Based upon: O. Dzyubachyk, J. Essers, W. A. van Cappellen, C. Baldeyron, A. Inagaki, W. J. Niessen, E. Meijering. Automated Analysis of Time-Lapse Fluorescence Microscopy Images: From Live Cell Images to Intracellular Foci. *Bioinformatics*, vol. 26, no. 19, October 2010, pp. 2424–2430.

4.1 Introduction

The ability to perform analyses on individual cells presents evident advantages over the traditional averaging over the whole cell population [62]. In many studies, such analyses are mainly performed manually, which is very tedious and often lacks accuracy, completeness, and reproducibility. To improve this, automated methods are essential. In this chapter, we present a new system for performing intracellular analysis in time-lapse fluorescence microscopy image data of cell colonies. The system consists of two main modules: cell analysis and foci analysis. The first is more generic and can be applied to a large variety of biological data acquired for cell analysis. The second is naturally a more application dependent step and requires specialized methods depending on the structures of interest.

A number of cell segmentation and tracking algorithms have been presented in the recent literature [2, 44, 51, 90, 115]. However, very few can potentially satisfy the requirements imposed by live cell imaging and analysis at the individual cell level. Specifically, a candidate algorithm should have capability to handle 3D time-lapse image data sets, it should provide full segmentation (detection only is insufficient) and tracking, be able to handle cell divisions, and show good performance even in the presence of significant noise and inhomogeneous intensity distributions (whether in the background or within cells). Here we use our robust level-set based cell segmentation and tracking algorithm [49] for this purpose. We also present an extension of the algorithm that allows registration of each cell to a common coordinate system by applying motion correction after segmentation and tracking. This is necessary to study the true relative dynamics of intracellular processes.

As for the subsequent step of intracellular analysis, we focus here on fluorescent foci, which appear in many biological studies. Representing high concentrations of the corresponding fluorescently labeled protein, foci are usually the main indicator of an underlying biological process occurring at these locations [57, 87]. Consequently, this makes foci analysis the main tool for studying protein-related processes by means of fluorescence microscopy. Examples of biological research based on foci analysis include fluorescent in situ hybridization (FISH) experiments [64, 83, 112, 126], analysis of DNA replication and repair [53, 76, 105], and classification of cell cycle phases [51]. In this chapter, we present a novel foci segmentation algorithm, and evaluate its robustness in segmenting foci of different size and intensity, as well as clustered foci.

In addition to presenting the algorithms used in the different steps, we also validate the complete system by showing its ability to reproduce findings from two biological studies that were based on expert manual analyses. In the first experiment, we investigate the time course of nuclear foci formation and disappearance upon treatment with ionizing radiation of the 53BP1 DNA repair protein. In the second experiment, we employ the system for identifying cell phases in time-lapse images of PCNA-GFP stained cells. PCNA or “proliferating cell nuclear antigen” is a central protein in DNA replication and PCNA foci mark the sites of active DNA synthesis. Thereby, automated cell phase identification is an important application that will facilitate further research of cell-cycle related studies [136], in particular cancer drug discovery [160]. To this end, as part of the second step of the system, we de-

veloped a simple yet effective algorithm for cell phase detection based on observed typical PCNA foci patterns through the cell cycle [87]. The results of the validation experiments clearly show the potential of the system for performing screening of high-content cell-based assays in applications involving the considered tasks.

4.2 Methods

The developed system processes images in a top-down fashion: 1) cell analysis and 2) foci analysis. Here we present the methods developed for performing these tasks.

4.2.1 Cell Analysis

To prepare for analysis of intracellular structures it is necessary to first determine the position and outline of each cell in the image data. Often it is also useful to transform the found cells to a common coordinate system to analyze intracellular changes free of global cell motion. This requires two processing steps: 1) cell segmentation and tracking, and 2) cell motion correction.

Cell Segmentation and Tracking

Segmentation and tracking of cells in image sequences is a difficult task. Especially in live cell imaging experiments it is hampered by low signal-to-noise ratio, cell clustering (unclear cell boundaries), inhomogeneous intensity distributions (in the background or within the cells), and intensity decay (due to photobleaching). In this system we have adopted our recently developed level-set based cell segmentation and tracking algorithm [49]. The algorithm performs simultaneous segmentation and tracking by means of a model evolution approach, employing level sets as the underlying model. In the cited paper we have shown that such approach guarantees a high quality of segmentation under strongly varying intensities (whether spatially or temporally), the ability to handle data of any dimensionality (2D, 3D, or even higher) without requiring fundamental changes to the algorithm, and natural handling of topological changes, which is a prerequisite when dealing with dividing cells. A detailed description of this algorithm can be found in the cited paper.

Cell Motion Correction

Motion correction methods can be roughly divided into two groups: feature-based and shape-based (or area-based) [177]. The former use information about image features (usually related to image intensity) whereas the latter use shape information only. The choice for one type or the other is dependent on the underlying biological application. Both types of methods have been applied successfully for motion correction of segmented cells [82, 99, 100, 169]. However, none of these methods can be applied directly to our problem. First, since our ultimate aim is to perform analysis of intracellular structures, only shape-based registration can be used. Second, the method should be able to separate global cell motion from local deformations, which is an ill-posed problem [171].

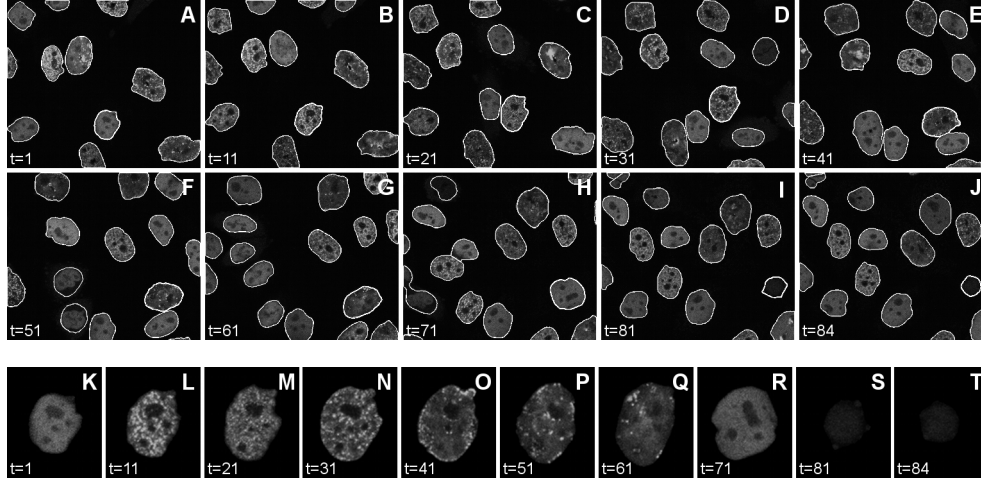


Figure. 4.1: Example of motion correction using the proposed approach. The two top rows show the motion of one cell extracted from a time-lapse fluorescence microscopy image data set (outlined in white). One slice ($z = 1$) is shown for time steps 1, 11, 21, 31, 41, 51, 61, 71, 81, and 84. The third row shows (magnified) the result of cell motion correction after segmentation and tracking. In this case only the global motion of the nucleus is subtracted.

To solve this problem, we have adapted the approach of Paragios *et al.* [121], where a shape is described by a signed distance function. This perfectly fits our needs, as the output of the cell segmentation and tracking step are level-set functions using the same representation. Shape registration is then performed via energy minimization, using an energy functional that contains terms representing both global motion and local deformation. Since normally cells do not change shape dramatically between two consecutive time steps, we register each image to its predecessor. The only exception is cell mitosis, during which a cell undergoes considerable (and quite typical) shape change. To deal with such cases, we consider the newly-born daughter cells as new objects, and initiate a new registration sequence for each of them. Thus, registration is performed on the full lifespan of a cell: from the moment after division (or from the first frame in the sequence) until the moment when the cell divides (or until the last frame).

Another issue arises from the typical sparseness of microscopy data along the z axis in 3D. As pointed out by [100], the rotation of cells in a typical assay is virtually limited to rotation around the z axis only, and since vertical displacement is practically absent too, the registration task essentially becomes a 2D problem. Therefore, we perform registration on the maximum intensity projection of the 3D cell region, and apply this transformation to each slice of the 3D image.

In our algorithm, the deformation of a 2D cell region is described by rotation angle θ , shift $T = (T_x, T_y)$, scaling factor s , and local deformation field (U, V) . Shape

registration is then achieved by minimization of the following energy functional:

$$\begin{aligned}
E(s, \theta, T, (U, V)) = & \alpha \iint_{\Omega} N_{\delta_1} (s\Phi_D - \Phi_S(A))^2 d\Omega \\
& + (1 - \alpha)\beta \iint_{\Omega} N_{\delta_2} (s\Phi_D - \Phi_S(A - (U, V)))^2 d\Omega \quad (4.1) \\
& + (1 - \alpha)(1 - \beta) \iint_{\Omega} N_{\delta_2} (U_x^2 + U_y^2 + V_x^2 + V_y^2) d\Omega,
\end{aligned}$$

where Φ_D and Φ_S are the signed distance functions corresponding to the source and the target shapes, Ω is the image region, $N_{\delta_1} = N_{\delta_1}(\Phi_D, \Phi_S)$ and $N_{\delta_2} = N_{\delta_2}(\Phi_D, \Phi_S)$ are narrow bands around the shape contours, $\alpha, \beta \in [0, 1]$ are balancing weights,

$$A(x, y) = \begin{pmatrix} A_x \\ A_y \end{pmatrix} = s \begin{pmatrix} \cos \theta & \sin \theta \\ -\sin \theta & \cos \theta \end{pmatrix} \begin{pmatrix} x \\ y \end{pmatrix} + \begin{pmatrix} T_x \\ T_y \end{pmatrix} \quad (4.2)$$

is the image transformation, and (x, y) are the Cartesian coordinates on Ω . Here, the non-rigid deformation field (U, V) serves as a complement to the transformation A to ensure better fitting and convergence. For generating the warped image, either only rotation and shift, or all the registration parameters are used, depending on the application. This way, the global motion of the object (in the first case) or the whole deformation (in the second case) can be removed, while retaining the local motion of intracellular structures (see Figure 4.1 for an example).

4.2.2 Foci Analysis

The next step after all cells are extracted from the image data is to analyze their content. For our applications, which involve the analysis of fluorescent foci, this requires two processing steps: 1) foci segmentation, and 2) foci pattern recognition.

Foci Segmentation

Similar to cell segmentation, the foci segmentation process is a challenging task, due to imperfections in the imaging and the fact that foci may vary considerably in size (from subresolution to large regions), as well as in local contrast, total number, and degree of clustering. For example, in the case of PCNA, foci may be completely absent in both G phases of the cell cycle (Figure 4.1K,R–T and Figure 4.2), or appear as small spots in the early-S (Figure 4.1L–N and Figure 4.2) and middle-S (Figure 4.1O and Figure 4.2) phases, or as a large bright blob in the late-S phase (Figure 4.1P,Q and Figure 4.2). Existing algorithms for foci segmentation were developed mostly for the analysis of FISH dots [64, 83, 112, 126], which are easier to deal with due to their high contrast, regular spherical shape, uniform size, relatively small number, and thus relatively small degree or even complete absence of clustering. More involved methods for foci segmentation have also been proposed [12] but these require a large number of measurements to properly handle overlapping foci regions. Here we present a novel method for segmentation of fluorescent foci,

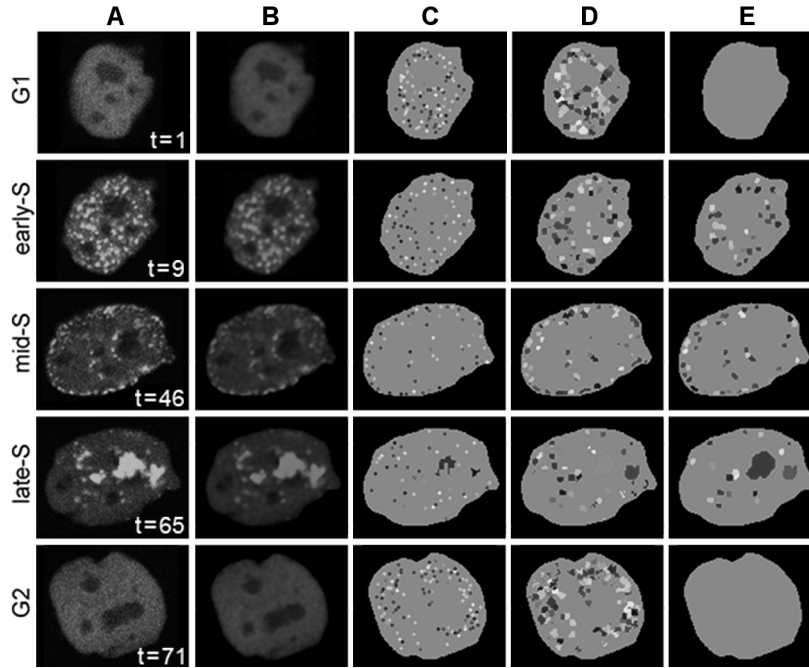


Figure. 4.2: Example of foci segmentation using our algorithm: (A) images of the same nucleus in five different time steps (1, 9, 46, 65, 71), each representing one of the phases of the cell cycle (G1, early-S, middle-S, late-S, G2); (B) results of applying patch-based reconstruction to each image; (C) initially detected foci markers (dots in different colors); (D) results of the graph-cut based segmentation algorithm; (E) final results after foci selection. All images are the first slice ($z = 1$) of the corresponding 3D image stack.

which uses a similar “local” strategy as that of Netten *et al.* [112], but includes additional steps that also enable segmentation of heavily clustered cells of varying sizes and shapes. The segmentation pipeline consists of three steps: 1) detection of foci markers, 2) foci segmentation, and 3) foci selection.

In the first step of the pipeline, a marker is identified for each potential focus, to be used as seed for the actual segmentation in the second step. All local maxima of the intensity landscape are initially selected as markers. In order to lower the number of false positives (local maxima that do not represent actual foci) in this stage, we first perform patch-based image reconstruction [13]. Since foci may appear as relatively small structures, we use patches of size 3×3 pixels. Using larger patches may blur the boundary between two neighboring foci so that it will become impossible to recognize them as two separate objects. Additionally, since we aim to perform the segmentation in 3D, we apply depth correction of intensity such that the mean and the variance of the intensity distribution of each slice within the cell (or nucleus) region are equal to those of the chosen reference slice. Example results after applying patch-based reconstruction and foci marker detection are shown in Figure 4.2B and Figure 4.2C respectively.

In the second step, foci segmentation is started by predicting the size of each focus, which is accomplished by calculating the average intensity in a window centered around its corresponding marker. Specifically, for each focus, the local average intensity is calculated for different sizes of the window (from unity to a predefined maximum value of expected foci sizes), and the estimated radius is taken to be the position of the maximum gradient of the resulting curve. In most cases, this procedure allows correct segmentation of neighboring foci, even if their sizes differ significantly, and it helps to segment large conglomerates of clustered foci (see Figure 4.2 for the late-S phase). Segmentation is then performed in a window Ω_0 corresponding to the estimated size of the focus and centered around its marker, by energy minimization using the graph-cuts method [15], which allows to combine both image-based and smoothness-based energies:

$$E = E_{\text{image}} + E_{\text{smoothness}}. \quad (4.3)$$

The latter is especially important in the case of noisy fluorescence microscopy images, where the boundaries of the foci are very weak. In order to calculate the image-based energy, we first perform fitting of the intensity histogram in Ω_0 , thereby obtaining two classes: foreground (foci) and background. The image-based energy of the foreground and of the background is defined as the negative logarithm of the corresponding intensity histogram, and the total image-based energy is obtained as:

$$E_{\text{image}} = \sum_{\mathbf{x} \in \Omega_0} -\ln \frac{h_f(I(\mathbf{x}))}{h_b(I(\mathbf{x}))}, \quad (4.4)$$

where $I(\mathbf{x})$ is the image intensity of the voxel \mathbf{x} , and h_f and h_b are the smoothed intensity histograms of the foreground and of the background, respectively. The regularization energy term is defined as the sum of a certain form functional over the set N of all the neighboring voxel pairs (p, q) :

$$E_{\text{smoothness}} = \lambda \sum_{(p,q) \in N} \exp \left(-\frac{\|I_p - I_q\|^2}{2\sigma^2} \right) \frac{1}{\|p - q\|}, \quad (4.5)$$

where λ is a real-valued weight, and the parameter σ is calculated from the data. The result of the foci segmentation step is shown in Figure 4.2D.

The third and final step is the selection of segmented foci in order to reject false positives. This process is guided by two parameters, which can be determined empirically: the expected minimum focus size and the expected minimum contrast (the difference between the mean intensities of a focus region and its local background). In addition, the Grubbs test [63] for detection of statistical outliers is applied. The test is performed on the intensity distribution of a local window around each segmented focus. Specifically, all voxels belonging to a segmented focus are added one-by-one to the mentioned local background distribution, and the Grubbs test is performed to detect which of these are outliers. If the number of outliers detected this way is less than the provided minimum focus size threshold, the focus is rejected. Applying all three criteria (minimum foci size, minimum contrast, and the statistical test) together, we obtain the final result of the foci segmentation algorithm, examples of which are shown in Figure 4.2E.

Foci Pattern Recognition

The analysis of foci patterns is relevant to many biological studies. In this chapter we consider the example of automatic identification of the cell cycle phase based on PCNA-GFP foci. Most of the published methods for cell cycle phase identification rely on machine learning techniques, which typically require large numbers of training data and/or the calculation of a large number of (static and dynamic) features for classification [51, 68, 160]. Alternatively, cells may be labeled explicitly with cell phase markers [115, 148], giving them a characteristic appearance during each of the cell cycle phases. In our applications, we aim to identify the cell phases directly from the inherent labels used in the experiments. Our algorithm is based on the typical behavior of PCNA foci through each of the phases of the cell cycle. Since in this particular application we are interested in the duration of each of the phases of the cell cycle (see the experimental section), we approach the problem by finding transitions between different phases in the complete sequence rather than trying to classify each of the images as belonging to one of the cell phases regardless of the rest of the images in the sequence. A set of simple techniques is used to distinguish the moment at which some cell goes from one stage to another.

The algorithm starts with detecting the presence of the G1 and the G2 phases by the absence of foci (in practice this is done by checking the number of segmented foci against a predefined threshold), keeping in mind that G1 is always the first and G2 the last phase in the sequence. Then, it detects possible transitions between the early-S and the middle-S phase, and between the middle-S and the late-S phase, using *K*-means clustering. Since different features are discriminative for different sub-phases of the S phase, we found it convenient to perform the clustering twice (once for the early-S and the middle-S and once for the middle-S and the late-S phases) rather than trying to classify all three sub-phases in one step. The clustering is achieved by using only two features (time step and percentage of foci located at the boundary) in the first case, and three features (time step, average focus size, and average distance from the foci to the upper boundary) in the second case. For both cases, seeds are provided for the *K*-means algorithm, which are calculated based on the number of foci features (such as average size, number, percentage of foci located at the boundary). Since in some of the sequences not all the phases are imaged, the missing phases should be disregarded during the cell phase classification. In the algorithm the decision about the existence of some of the sub-phases of S is done automatically by analyzing the range of the values of the two features: the number of foci located at the boundary (for the transition from the early-S to the middle-S) and the number of foci in the upmost slice that contains foci (for the transition from the middle-S to the late-S). The corresponding transition is disregarded if the maximal and the minimal value of a feature are on the same side of an empirically set threshold.

4.3 Validation

The developed system was validated by comparing its performance to expert human observers in two experiments: 1) foci counting, and 2) foci-pattern based cell phase identification.

4.3.1 Foci Counting

The protein 53BP1 forms foci in response to genotoxic stress, particularly agents inducing DNA double strand breaks [4]. Moreover, these foci are thought to represent actual sites of DNA breaks [130] and their disappearance is related to the DNA double strand break repair kinetics. For example, we found in normal mouse embryonic stem (ES) cells (IB-10) that the percentage of positive cells (containing at least 5 foci per cell) drastically increased just 5 min after treatment by 8 Gy ionizing radiation (IR) and decreased at 3 h to reach the normal situation in untreated cells at 24 h after IR (data not published; see Figure 4.3).

Data

ES cells were fixed at selected time points after IR treatment (8 Gy) and 53BP1 foci were imaged by indirect immunofluorescence using anti-53BP1 antibodies and confocal microscopy (Zeiss LSM-510) with a Plan-Apochromat $63\times/1.4$ oil-immersion objective lens. The data set consisted of in total 49 images of size 512×512 pixels (resolution $146.2\times 146.2\text{ }\mu\text{m}/\text{pixel}$) or 1024×1024 pixels (resolution $73.1\times 73.1\text{ }\mu\text{m}/\text{pixel}$). Each image contained two channels: the DNA channel and the protein channel. The DNA channel was used for the segmentation of the cells because of its more homogeneous signal distribution in the cell regions (see Figure 4.4).

Results

The sample images in Figure 4.4 illustrate that the cell colonies were densely clustered and that some of the nuclei showed very irregular shapes (as imaged). Together with the relatively low and inhomogeneous contrast, and a considerable amount of noise, this makes automated segmentation challenging. Nevertheless, in all the images our system was able to yield satisfactory segmentations for subsequent foci analysis. Next, automatic foci counting was performed, and the results were compared to manual counts by an expert human observer. In order to make a fair comparison, for each image we selected the same number of segmented cells as considered by the human expert in the manual analysis, by applying a size threshold. In total, 858 cells were selected for automatic foci counting, 685 of which contained foci, and 435 were identified as positive (≥ 5 foci). Two measures were calculated for each time point: the percentage of positive cells and the average number of foci per cell. The results (Figure 4.3) clearly show that the automatically obtained results are in good agreement with the results obtained by manual analysis, both qualitatively and quantitatively. In particular, for both measures, the calculated general trend is virtually the same.

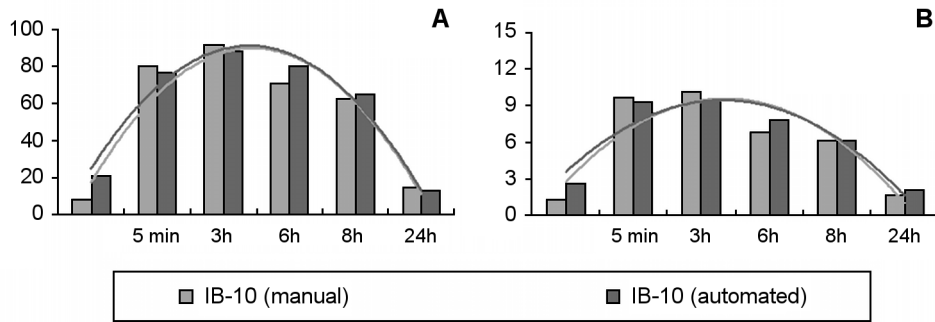


Figure. 4.3: Comparison between manual (orange) and automated (blue) 53BP1 foci counting for normal embryonic stem cells (IB-10) in terms of (A) the percentage of the positive cells and (B) the average number of foci per cell at various time points. For each of the measures the corresponding values and the obtained polynomial trend lines are shown.

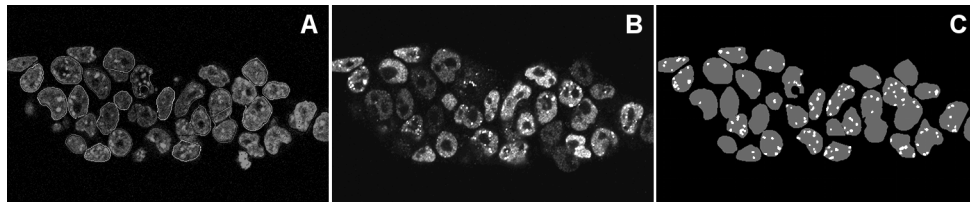


Figure. 4.4: Sample results from the automated foci counting experiment: (A) DNA channel with segmented cell boundaries overlaid (contours of various colors); (B) protein channel; (C) region masks (red) extracted from (A) together with the foci of interest (white) segmented from (B). Each of the images has been cropped from its original size and on the images (A) and (B) contrast enhancement was performed for better visualization.

4.3.2 Cell Phase Identification

The DNA polymerase processivity factor proliferating cell nuclear antigen (PCNA) is central in DNA replication. We analyzed the temporal localization pattern of green fluorescent protein (GFP) tagged PCNA in living CHO cells during the different cell cycle phases (G1, early-S, middle-S, late-S, G2). Replication of the mammalian genome starts at thousands of origins activated at different times during S phase. By tracking the individual sites of replication foci represented by PCNA, we can investigate how this replication program is coordinated. In a previous study [52] we showed that the average times needed to progress through one complete cell cycle varies greatly in individual cells, with the largest variation in the duration of the G1 phase. Here we aim to perform similar analysis in a fully automatic fashion using our system.

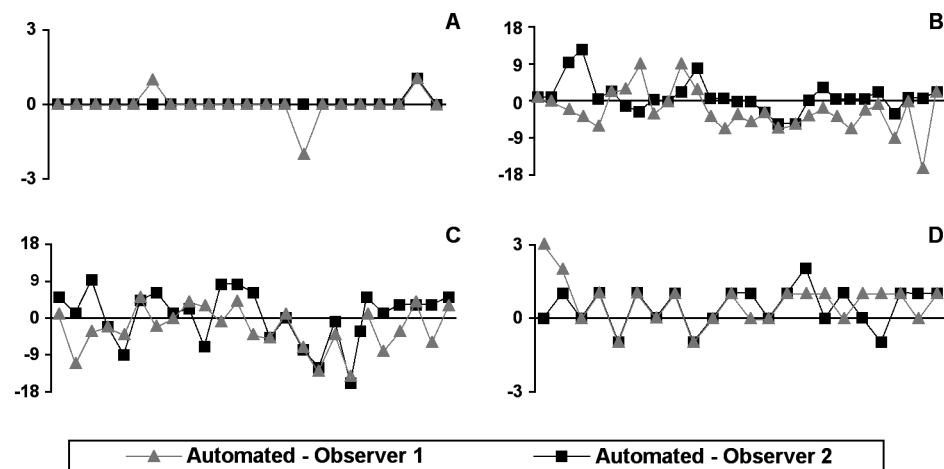


Figure 4.5: Comparison between manual and automated detection of phase transition moments in PCNA-stained cells. The four plots correspond to the four possible phase transitions: (A) G1 to early-S (21 cases), (B) early-S to middle-S (29 cases), (C) middle-S to late-S (26 cases), and (D) late-S to G2 (22 cases). In each case, the difference in detection times between the automated method and each of the two observers is plotted. A missing point on one of the curves in (C) means that the corresponding phase transition was not detected by the corresponding observer.

Data

Five fluorescence microscopy image data sets were acquired as described by Essers *et al.* [52] using a confocal microscope (Zeiss LSM-510) with a Plan-Apochromat $63\times/1.4$ oil-immersion objective lens. The images consisted of 92 time steps (≈ 10 min intervals) each having 5 slices ($1\ \mu\text{m}$ apart) of size 512×443 pixels ($103.4 \times 89.5\ \mu\text{m}$). All cell nuclei were automatically segmented, tracked, and motion corrected (for retrospective visual examination; see sample results in Figure 4.6), and for each of the nuclei the PCNA foci were segmented. The subsequent analysis was restricted to cells passing through at least one whole phase of the cell cycle during the time span of the sequence. In addition, cells partly falling outside the field of view at any time point were also disregarded, as these cannot be reliably analyzed due to incomplete information. This selection procedure resulted in 29 cells suitable for analysis. Two expert biologists independently marked the transition moments between the different phases of the cell cycle for each of the selected cells in the raw image data to serve as the ground truth.

Results

The plots in Figure 4.5 show the differences in the phase transition times as found by our system versus both observers for each of the four possible phase transitions. The results clearly confirm, in agreement with Ersoy *et al.* [51], that it is much easier to distinguish the G1 and G2 phases from the S phase (Figure 4.5A,D and Figure 4.6)

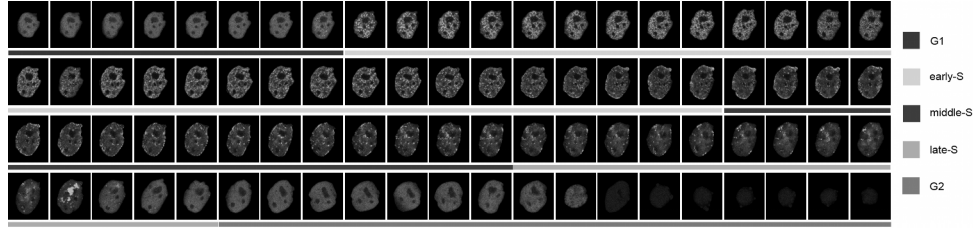


Figure 4.6: Sample results from the cell phase identification experiment. Shown from top left to bottom right are cropped images of 84 successive time points of a single, motion-corrected cell nucleus, going from the G1 phase, through the early-S, middle-S, late-S, to the G2 phase (indicated by bars in different colors below the images), as automatically recognized by our system based on characteristic foci patterns for each of these phases. The example also illustrates the observation that it is easier (also visually) to distinguish the G phases from the S phases than to distinguish between the different S phases.

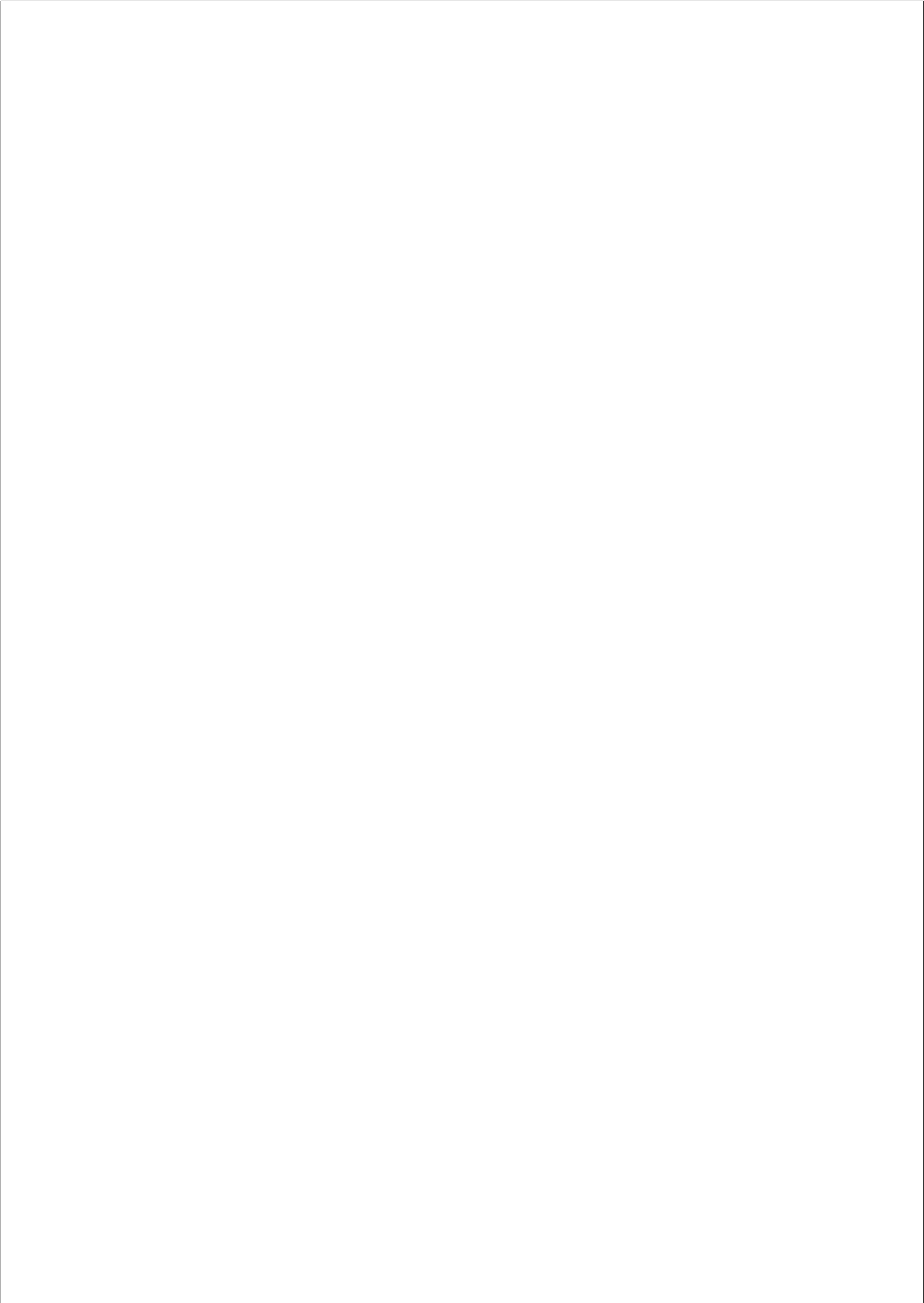
than to distinguish between the different sub-phases of the S phase (Figure 4.5B,C and Figure 4.6). For the transitions from G1 to early-S, and from late-S to G2, the absolute differences in the times detected by our system versus any of the two observers did not exceed 2 time points, which is less than the maximum difference found between the two observers. For the transitions from early-S and middle-S, and from middle-S to late-S, the maximum absolute difference between our system and any of the observers was 17 time points, which is equal to the maximum difference found between the two observers. In most cases, the differences with respect to the two observers showed opposite signs (meaning that the automatically detected transition time was in between the times indicated by the observers), or one of the differences was relatively small (indicating that the automatically detected time point was close to that found by one of the observers). However, there were also several cases where our algorithm showed considerable difference with both observers, while their results were in good agreement. An important observation following from these cases is that the results were much better (closer to those of the observers) for sequences where more transitions (ideally all four) were present. And vice versa, for sequences where only two or three out of four transitions were present, our algorithm encountered difficulties in correctly detecting the time moments of those transitions.

4.4 Conclusions

In this work we have presented our fully automated system for performing intracellular analysis at the individual-cell level. The system consists of two main parts: cell analysis (including cell segmentation, tracking, motion correction), and foci analysis (foci segmentation and pattern analysis). The experimental results presented in this chapter show that the system performs comparably to manual analysis by expert biologists for the tasks of foci counting and foci-pattern based cell phase identification. The main contribution of the work is that the different analysis tasks are

combined into an integrated, fully automated system, which does not require any user interaction (apart from inevitable initial parameter setting). An additional advantage of the system compared to some other advanced methods is that it does not involve an explicit (machine-)learning stage, which would require large amounts of training data. Instead, it uses features derived directly from the segmented foci. Direct comparisons with experimental results reported in other papers on automated foci counting and cell phase identification methods could not be made, either because these experiments focused on different applications than ours, or they were based on different quantitative measures and/or imaging protocols. However, our primary goal was to develop a system that would allow upscaling of experiments that are normally performed manually by expert human observers. Being able to reproduce their findings, our system can indeed replace tedious manual analyses, and thus enables high-content screening.

The current version of the system (as used in the presented experiments) was coded in MATLAB (The MathWorks, Inc., USA) and compiled for use as a stand-alone software tool. On a standard PC (Intel Pentium 4-CPU, 3.6GHz, 3 GB RAM, running Windows XP), full cell segmentation and tracking currently takes about 3.5 hours per sequence of 92 time steps which contain 20 cells on average (that is, about 7 seconds per cell, per time point), optional cell motion correction takes about 35 seconds per cell per time point, foci segmentation about 15 seconds per cell per time point, and finally the calculation of foci-related measures and cell phase identification about 0.5 seconds in total per time point. Considerably higher speeds can be expected after conversion to a full C++ implementation and further optimization of the source code. Also, parts of the system allow a parallel implementation, which would further increase performance. This is envisaged for near-future work. The software will be made publicly available, free of charge for non-commercial use, after publication of this chapter.



Model-Evolution Based Tracking of *Caenorhabditis* *Elegans* Embryogenesis in Fluorescence Microscopy

5

Abstract — Fluorescence microscopy has become a primary tool for studying embryogenesis of the *Caenorhabditis elegans* (*C. elegans*) nematode worm. It enables imaging of individual embryos from the single cell to the adult stage with good spatial and temporal resolution. There is a great need for improved tools that allow fully automated analysis of the resulting large and complex image data sets. A novel automated system for analyzing *C. elegans* embryogenesis image data was developed. The system is based on a model evolution approach to cell nuclei segmentation and tracking, and is able to follow *C. elegans* embryogenesis until at least the 350-cell stage with high accuracy, as confirmed by validation experiments on four data sets originating from two different laboratories. Calculated error rates indicate the superiority of the presented approach over state-of-the-art algorithms for tracking of *C. elegans* embryogenesis. The proposed system proves to be both effective and efficient in performing simultaneous segmentation and tracking (lineage reconstruction) of *C. elegans* embryogenesis fluorescence microscopy data. Apart from initial parameter setting, it requires no (or very limited) user interaction, which allows to completely substitute (at the early stages of embryogenesis) or complement (at the later stages) expert human observers.

Based upon: O. Dzyubachyk, R. Jelier, A. Krüger, W. J. Niessen, B. Lehner, E. Meijering. Model-Evolution Based Tracking of *Caenorhabditis Elegans* Embryogenesis in Fluorescence Microscopy, prepared for submission.

5.1 Background

The nematode *Caenorhabditis elegans* (*C. elegans*) is a widely used model organism in molecular and developmental biology due to its relative simplicity (the adult organism consists of only 959 cells), known genome and ease of genetic manipulation [72,162], invariant lineage tree [143], fast reproduction (the development from a single zygote to a complete adult worm takes only a couple of hours), and its transparency. Usage of modern fluorescence microscopy techniques enable imaging of *C. elegans* embryogenesis from the single cell to the adult stage with good spatial and temporal resolution. However, further progress in this field is greatly hampered by the lack of reliable tools for (semi-)automated analysis of the resulting image sequences. The 4D data sets typically consist of many thousands of images, showing hundreds of cell divisions, and on the order of 10,000 cell nuclei at different time points [7], precluding fully manual processing.

Up till now, only few attempts have been made to perform automated segmentation and tracking on *C. elegans* embryogenesis image data. In [89] the authors used gradient flow tracking to segment stacks of (on average) 187.75 nuclei with over- and under-segmentation error rates of, respectively, 1.59 % and 0.39 %. In [95] the authors used a cascade of simple image processing techniques to segment nuclei on the images of straightened *C. elegans* embryos at the 558-cell stage. They selected 357 that could be reliably distinguished from all nuclei present at that time point and used their method to segment these, reaching an overall success rate of 86 %. In [29] a specialized tracking segmentation algorithm for automated construction of *C. elegans* lineages was presented. Nuclei were segmented by the 3D watershed algorithm [155] and tracking was performed by linking the segmented nuclei between consecutive time points. The algorithm was able to reach the 90-cell stage with 68 % tracking accuracy.

A state-of-the-art tool for lineage tracking in developing *C. elegans* embryos is StarryNite [10]. It performs frame-by-frame detection of the nuclei by fitting a spherical model to the image, and subsequently links the found nuclei between consecutive frames. Using this tool, reliable tracking can be performed until at least the 180-cell stage, after which its performance drops rapidly, requiring excessive manual curation of the results after the 350-cell stage, for which various visualization and editing tools exist [16,18,110]. The underlying algorithms have a number of shortcomings that hamper wider usage, namely the need to carefully tune a large number of (time-dependent) parameters, and poor robustness across data sets acquired with (even slightly) different imaging settings. Specific errors (such as movements erroneously labeled as divisions) can be significantly reduced by postprocessing using machine learning [7]. However, the 350-cell stage remains challenging, and improved methods for fully automated lineage reconstruction up to and beyond that stage are still very much needed.

Here we present a novel, fully automated method for reconstructing cell lineages of developing *C. elegans* embryos from time-lapse fluorescence microscopy image data. The work considerably extends our preliminary conference report [46]. The presented method performs both segmentation (rather than mere detection) of cell nuclei and their tracking over time. In order to be as little imaging-protocol de-

pendent as possible, we designed the algorithm such that it uses only a few input parameters, with clear physical meaning, and without the need to (re)set them to different values during processing, for different stages of development. In addition, relevant image and cell features are continuously monitored over time, and their values in previous time steps are used to automatically adapt corresponding parameters to the current time step. Experiments on sample data sets from two different laboratories demonstrate the robustness of the method.

5.2 Methods

The method we propose is based on the so-called model-evolution approach [102, 176], which performs both segmentation and tracking. Recently we have presented an algorithm applying this approach to cell segmentation and tracking, using level sets as the main model [49]. In application to tracking *C. elegans* embryogenesis, this approach has several advantages, including (i) incorporation of information of the current state of the system (accumulated from previous time steps) into the segmentation of the next image stack in the sequence, which is especially useful when segmenting densely packed cell colonies, (ii) the ability to naturally handle cell divisions, and (iii) robustness to noise and varying foreground and background intensity distributions. However, a major disadvantage of the algorithm is its computational cost, which prohibits direct application to tracking *C. elegans* embryogenesis, due to the very large number of images and objects to be processed. In the present chapter, we propose a specialized algorithm for segmentation and tracking in *C. elegans* embryogenesis image data, which is still based on the idea of model evolution, but differs considerably in implementation. The general flow of the new algorithm can be divided into four main steps (Figure 5.1): 1) initial segmentation, 2) division and motion assessment, 3) multi-cell segmentation and tracking, and 4) correction and output. The following subsections describe each of these steps.

5.2.1 Initial Segmentation

The first image stack in the sequence is relatively simple to segment, as it usually contains only a small number of objects (typically four nuclei as in Figure 5.2), and therefore does not require a very sophisticated method. For this initial segmentation, which is performed only once, we use a non-PDE based energy minimization method [141] refined by level-set segmentation. More details on the implementation of the described approach can be found in [49]. The output of this step is the starting point for the segmentation and tracking of the subsequent image stacks in the sequence, performed by iterating the steps described in the next subsections.

5.2.2 Division and Motion Assessment

The processing of each next image stack in the sequence commences with the detection and handling of divided cells, and the initial motion estimation of all other cells, which are considerably adapted (the former) or newly added (the latter) operations

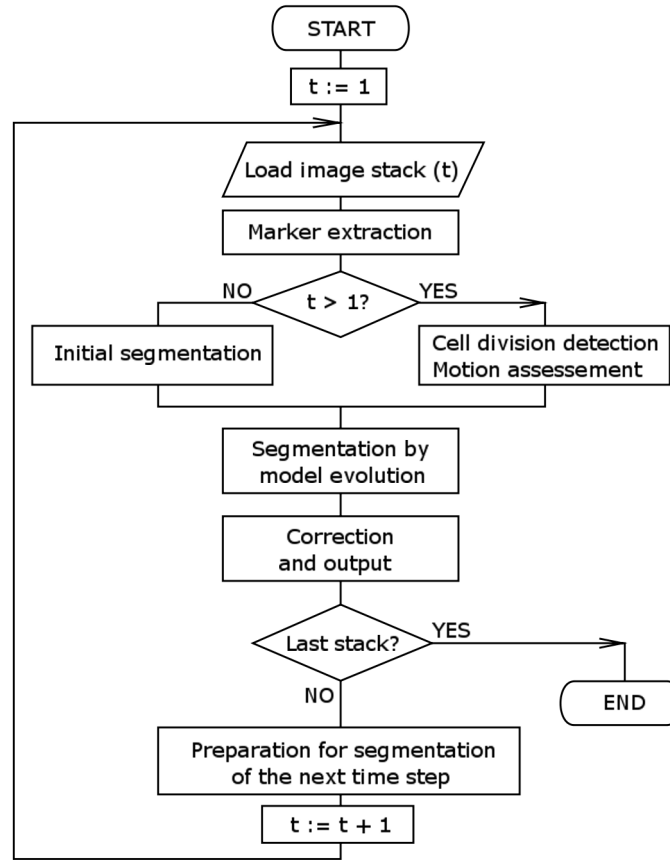


Figure. 5.1: Flow diagram of the method. The diagram lists all the important steps of the algorithm (described in detail in the methods section of the main text) and the order in which they are executed.

compared with our general-purpose algorithm [49]. Both operations rely on measurements obtained from the images. Specifically, we extract markers representing the new (center) positions of nuclei, by filtering each slice of the image stack with a disk of radius equal to the estimated average radius of the nuclei at the given time point. The peaks of the resulting surface $I_f = I_f(t)$ are taken as the markers.

The first operation, detection and handling of divided cells, is necessary to capture the daughter cells that move away from the mother cell after the moment of division. Since the actual cell division often occurs between two time points (image stacks), and the displacement of the two daughter cells with respect to the mother cell can be relatively large compared to the regular cell motion, evolving the model in the close vicinity of its previous state is usually insufficient. To tackle this, we developed a specialized procedure that analyzes the set of found markers in the neigh-

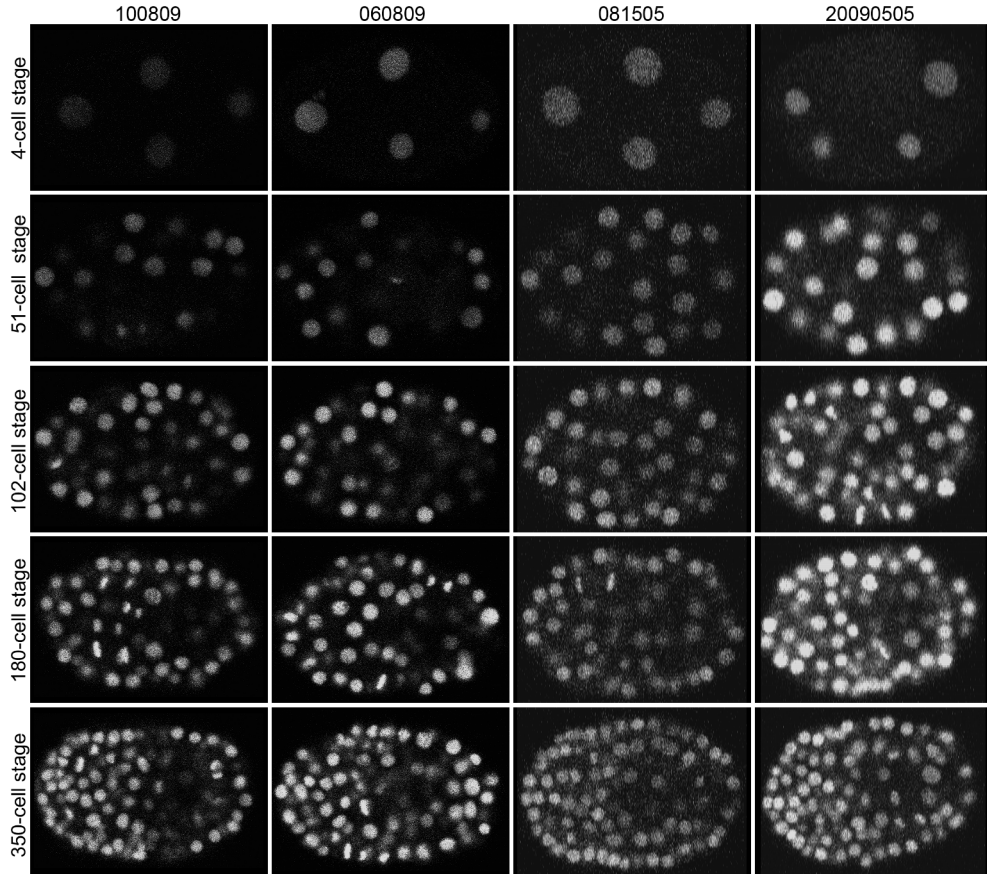


Figure 5.2: Sample image data. For each data set (the identification number of which is shown at the top) used for the evaluation of our method, one slice (z index) is shown from the image stacks at five different time points (corresponding to the 4, 51, 102, 180, and 350-cell stage): $z = 8$ (100809 and 060809), $z = 16$ (081505), $z = 14$ (20090505).

borhood of each mitotic cell (our algorithm for detection of mitotic cells is described later in the text and illustrated in Figure 5.3).

For a cell to be labeled as divided, the following natural conditions must be satisfied: 1) the profile connecting the markers of the potential daughter cells should be bi-modal (as determined with the Hartigan dip test [69]), 2) no other object should intersect the line connecting both markers, and 3) the daughters should be close to the mother:

$$\max(d_i^{(1)}, d_i^{(2)}) < D_{max}, \quad (5.1)$$

where $d_i^{(1)}$ and $d_i^{(2)}$ are the distances of the markers of the potential daughters to the center position of the mother cell i in the previous time point and D_{max} is the maxi-

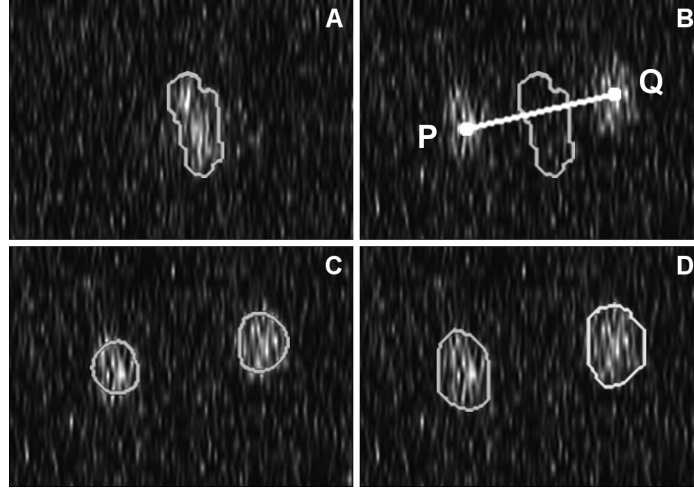


Figure. 5.3: Detection of cell division. The panels show (A) a cell in one time point, with its segmentation (overlaid colored contour), (B) the line connecting markers P and Q of the potential daughter cells, (C) the seeds and (D) final segmentation of the two daughter nuclei.

mum allowed distance. If a set of markers is found satisfying all these conditions, the cell is labeled as possibly divided. In case there is more than one pair of feasible markers, we choose the one with the highest score s_i :

$$s_i = \frac{b_i + 1}{2} + \frac{w_i}{\max_i w_i} - \frac{8 \left(d_i^{(1)} + d_i^{(2)} + d_i^{(12)} \right) + d_i^{(1)} d_i^{(2)} |\sin \beta|}{16D_{max}}, \quad (5.2)$$

with

$$w_i = a_i + \frac{\min \left(mn_i^{(1)}, mn_i^{(2)} \right)}{2 \max \left(mn_i^{(1)}, mn_i^{(2)} \right)} + \frac{\min \left(mj_i^{(1)}, mj_i^{(2)} \right)}{2 \max \left(mj_i^{(1)}, mj_i^{(2)} \right)},$$

where b_i is the ratio between lengths mn_i and mj_i of, respectively, the minor and major axes of the mother cell nucleus, β is the angle between the lines connecting the markers of the potential daughters with the center of the mother cell, $a_i \in [-\pi/2, \pi/2]$ is the angle between the expected (along the minor axis of the mother cell) and the calculated division direction, $mn_i^{(1,2)}$ and $mj_i^{(1,2)}$ are the estimated minor and major axes of the potential daughter cells, while $d_i^{(12)}$ is the distance between the latter. The values of $mn_i^{(1,2)}$ and $mj_i^{(1,2)}$ are obtained by analyzing the intensity profile along the division direction and perpendicular to it, where the width of each peak is calculated using the D'Agostino K^2 test [33].

Since the number of divisions occurring at the same time can be quite high in *C. elegans* data (especially in the later stages of development), it may happen that some of the cells labeled as possibly divided share the same potential daughter.

We resolve such situations by jointly analyzing the set of all potential division configurations to find the most probable configuration of divided cells using the following steps: 1) choose the one with the highest s_i score (i_0) and label it as a true division, 2) remove from the list of all the potential divisions those pairs who share one of the markers with i_0 , and 3) remove i_0 from the list and go back to Step 1. In case a wrong decision has been made at this step because of the bad estimate of $mn_i^{(1,2)}$ and $mj_i^{(1,2)}$, it can later be corrected after the segmentation is obtained and the real values of those parameters are known.

The second operation, estimation of the motion of each cell with respect to the previous time point, is applied for its positive effect on the execution time of the segmentation and tracking step (described in the next subsection) as well as on its performance. The motion is estimated by analyzing the detected markers in the vicinity of a cell's previous position. The potential candidates (markers) of the cell's new position are scored based on two measures: goodness of fit, which incorporates both the object's size and its intensity, and the distance d_i between the candidates and the cell's position. The final motion estimate for each cell is obtained by jointly optimizing the whole set of objects on the calculated scores according to the nearest neighbor rule:

$$\operatorname{argmax}_i \left(\frac{\min(g_i^{(t)}, g_i^{(t-1)})}{\max(g_i^{(t)}, g_i^{(t-1)})} - \frac{d_i}{\max_i(d_i)} \right), \quad (5.3)$$

where $g_i^{(t)}$ and $g_i^{(t-1)}$ are, respectively, the values of the filtered intensity $I_f(t)$ calculated in the candidate point and the maximal value of $I_f(t-1)$ within the region covered by cell i . If after this procedure one of the daughter cell markers of a cell labeled as dividing is found to belong to another object, this cell is removed from the list of divided cells.

5.2.3 Multi-Cell Segmentation and Tracking

The key idea behind multi-cell segmentation and tracking by means of the model-evolution approach is that each cell i is represented by a function ϕ_i (also called the *model*), which is iteratively optimized (*evolved*) to fit the true cell region in the image stack at one time point, and then used as initial guess for the fitting procedure in the next stack in the sequence. Using level sets as a model, ϕ_i can be set to the signed distance function of the region, which is positive inside, negative outside, and zero on the boundary of the region. In this work, we chose ϕ_i to be the binary function that is *true* inside the region and *false* outside, as motivated below. The fitting procedure consists in the iterative (and simultaneous for all cells) minimization of an energy functional computed within a narrow band around the current cell boundaries. The resulting transformation of each ϕ_i mimics the displacement and deformation that the corresponding cell underwent between the previous and the present time point.

In our work, the energy functional consists of an image-based term and a smoothness constraint:

$$E = \sum_{p \in N_b} R_p(f_p) + \alpha \sum_{p,q \in N} B_{p,q}(f_p \neq f_q), \quad (5.4)$$

where p and q are voxels in the narrow band N_b , N is the set of neighbor pairings, α is a scalar that controls the smoothness of the detected boundary of the cell, and f_p and f_q are labels indicating the class (foreground fg or background bg) to which the corresponding voxels belong. The region energy R_p is set to the difference between the probabilities of voxel p to belong to the foreground or the background:

$$R_p(f_p = fg) = -R_p(f_p = bg) = -\ln P(I_p|fg) + \ln P(I_p|bg). \quad (5.5)$$

Here we have chosen to use the non-parametric probability density function P , which is calculated via the kernel density estimation [14] of the image intensities I within the corresponding region with a Gaussian kernel (the width of which is determined from the data). The boundary term $B_{p,q}$ is set to be the function of image contrast in the form:

$$B_{p,q} = \exp\left(-\frac{\|I_p - I_q\|^2}{2\sigma^2}\right) \frac{1}{\|p - q\|}, \quad (5.6)$$

where σ is calculated from the data as in [97].

For the minimization of the energy functional (5.4) we use the graph-cut algorithm [15], which turned out to be a much more efficient and effective technique for our application than level-set evolution, and guarantees finding the global minimum. Performing the energy minimization only in a narrow band around the cell regions, and restricting the solution space by applying nuclei separation (described next), makes the graph-cut algorithm (which is intrinsically a global method) suitable for multi-cell tracking. The use of graph-cuts instead of level-sets also enables a very efficient implementation of the algorithm. This is because, contrary to level-set evolution, there is no need to perform costly re-initializations of the ϕ_i to the signed distance function. Moreover, we can simply use a binary mask ("active mask") that is positive inside the cell region and negative outside. Since the energy is minimized in a narrow band around the current cell boundary, the size of each mask stored in memory can be limited to only a small window containing the cell region and a narrow band around it, together with the position of the window relative to the image stack.

During tracking, possible collisions of cells should be resolved, to prevent the incorrect situation that a cell is captured by multiple ϕ_i . This becomes increasingly challenging in later stages, as the number of cells grows rapidly, causing increased cell density and clustering. We resolve all potential collisions by a cell separation procedure, which is one of the cornerstones of our algorithm. Two main requirements for this procedure are that it should yield very accurate separation of all possible configurations of colliding cells and be computationally efficient. Here we use an improved version of the Radon-based separation algorithm that we presented

earlier [49]. The basic idea (illustrated in Figure 5.4) is to find a separating surface between each pair of adjacent nuclei in the form of a plane (justified by the typical spherical shape of a nucleus) based on the minimum of the Radon transform [34] of the image in the collision region. Two nuclei are considered “adjacent” if their corresponding narrow bands have at least one common voxel. The evolution of each ϕ_i is then constrained by its separating planes.

Several important improvements were introduced to make the separation algorithm more computationally efficient and robust to all possible configurations of clustered cell nuclei. First, the number of separations to be performed was considerably decreased by applying Delaunay triangulation [38] to the set of adjacent nuclei using their markers, and limiting the separation only to those pairs of adjacent nuclei belonging to the same Delaunay triangle, as illustrated in Figure 5.4E. Second, the space of possible solutions was restricted by employing the gradient information between the cells to be separated to find the point of minimal intensity on the line connecting their markers, and constraining the separation plane to pass through this point (Figure 5.4B). Third, the typical sphere-like shape of a *C. elegans* nucleus was exploited, by prohibiting the separation plane to be closer to any of the cell’s markers than some predefined distance (we used a value of half the major axis length).

5.2.4 Correction and Output

The correction of possible errors in the segmentation results consists in a search for false negatives (missed cell nuclei). To this end, the image foreground is estimated by thresholding, where the threshold value is chosen such that the size of the foreground (the number of voxels) is as close as possible to the total segmented volume in the previous time point (this value can be easily obtained from the cumulative histogram of the image intensity distribution). Next, the estimated foreground is divided into regions by applying the marker-controlled watershed algorithm [61] (using the markers extracted as explained earlier), and regions that intersect with at least one of the already known cell regions are excluded. Resulting candidates of false negatives with size exceeding the minimal nucleus size (computed from the previous time point) are added to the list of cell objects, and their corresponding ϕ_i are refined by energy minimization as described in the previous section. Those of the newly-found objects whose size after energy minimization falls below the minimal object size threshold are removed from the list. The rest of the objects is either labeled as “new” or as a division product (if a successful matching combination of the mitotic mother cell and the second daughter cell is found).

The preparation for segmenting the next image stack in the sequence includes updating several parameters, among others the minimal nucleus size parameter, and detecting mitotic nuclei. The minimal nucleus size is an important parameter that plays a crucial role in distinguishing real nuclei from noise. In our method, we provide an initial value for this parameter, after which its value is automatically updated after each time step based on the sizes of the segmented nuclei, subject to the physically realistic constraint that it can only decrease, and at most by 5 % between two consecutive time points. Detection of mitotic nuclei is based on their pronounced elongated shape and is performed in order to increase the computational efficiency

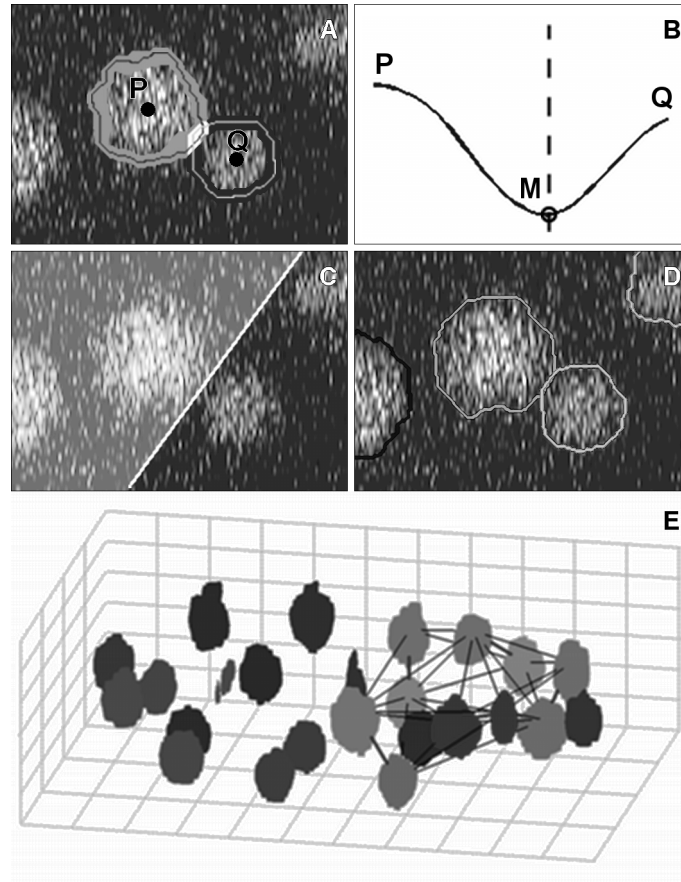


Figure 5.4: Radon-transform based cell separation. The panels show (A) the initial position of the contours (red and blue curves) of two adjacent cells (P and Q with their markers indicated by dots) for $t = 16$ with corresponding overlapping narrow bands (green and red areas), (B) the intensity profile along the line connecting the markers of the two cells to find the position of minimum intensity (indicated by the dashed vertical line and point M), (C) the separating plane (white line in this single slice) computed from the Radon transform around that position, (D) the final segmentation (colored contours) for $t = 16$, and (E) the selection procedure for adjacent cells that need to be separated. In the latter, all cell nuclei that need to be separated from at least one other cell are shown in shades of green (with the exception of the two cells in panel (A) shown in red), and all remaining cells (not adjacent to any other cell) are shown in shades of blue. All nuclei are shown with smaller size for visualization purposes. The lines connecting the markers of the cell nuclei are the edges of the Delaunay triangulation calculated on the set of adjacent (red and green) objects. Only the edges (highlighted in red) connecting actually adjacent cells are selected for performing Radon-transform based cell separation.

of the algorithm. Specifically, we make use of the observation that the majority of the divisions occurs (nearly) in the plane perpendicular to the z -axis, in the following manner: 1) we detect the reference slice of the region currently occupied by the given object as the one having the highest average intensity, 2) the lengths of the minor and the major axes and the orientation of the minor axis are calculated from the shape corresponding to the found reference slice, and 3) we label the corresponding cell as mitotic if the ratio of the lengths of the major to the minor axis b_i is greater than a user-defined threshold A_b . In addition, to simplify the distinction between mitotic nuclei and the newly-born nuclei that did not obtain a spherical shape yet, we use the natural restriction that a newly-born cell needs some time (more than a couple of minutes) before it can divide.

The software implementation of our method provides several different forms of output: textual, binary, and graphical. The segmentation results are saved in a binary image file format. Also, to facilitate visual inspection, the results per time point can be saved in the form of a 3D rendering, which can be subsequently combined into a movie (Figure 5.6). Tracking results are exported to the AceTree format [110]. In addition, information about important events (cell divisions and deaths) is stored in a human-readable log file. To further reduce (the propagation of) errors, we implemented the possibility to restart the program at any time point in the sequence, after expert manual curation of results (creation of new objects, deletion of existing ones, correction of cell divisions), which can be done using AceTree or our home-made tools.

5.3 Results and Discussion

5.3.1 Test Data Sets

The presented method was evaluated on four *C. elegans* embryogenesis image sequences, two from the EMBL Center for Genomic Regulation (Lehner lab), Barcelona, Spain, and two from the University of Washington (Waterston lab), Seattle, WA, USA. The reason for using data from different laboratories using different imaging protocols was to test the robustness of our method. Details of the data sets are listed in Table 5.1 and a sample image (before preprocessing) from each of the data sets is shown in Figure 5.2. Before segmentation and tracking, each image stack from each sequence was preprocessed by smoothing it with a disk kernel, with radius equal to half the expected nucleus radius.

Embryo preparation for the data from the Waterston lab is described in full detail in [110]. For the data from the Lehner lab, worms with GFP labeled histones (strain RW10029 [109]) were grown on OP50-seeded NGM plates and maintained by transferring the worms daily to maintain a healthy population with high-quality eggs. For embryo extraction, young adult worms were picked and placed into a drop of Boyd's buffer/methyl cellulose in a clean, prechilled watch glass. Prechilling the watch glass and solutions to 4°C temporarily slows the rate of development, leaving more time for microscope setup later. Worms were cut open with syringe needles, placing the cuts at the boundary between the uterus and the gonad, which released embryos of different stages. 1–4 cell embryos were selected from older ones

and transferred with a 10 μl pipette onto a microscope slide with 4 μl of 20 μm polystyrene beads (Polysciences) in Boyd's buffer/methyl cellulose (beads diluted 1:30 in buffer to reduce the diameter of the eggs to obtain a better fluorescence signal at the upper planes but without damaging the eggs with the cover slip). 22 \times 22 mm cover slips were gently lowered onto the bead mount to avoid the liquid touching the edge of the cover slip. Edges were sealed with molten paraffin to prevent the mountant from drying out during imaging.

5.3.2 Algorithm Parameters

A number of parameters need to be specified for our method. All of the parameters have a clear physical meaning and most of them are determined from the data. However, some of the input parameters, such as the weight of the smoothness-based energy term, can be determined only empirically, and setting a proper value for them may require some fine-tuning for each data set. As mentioned earlier, some parameters used in our algorithm, such as the minimal nucleus size, are intrinsically time-dependent. For these parameters, the user needs to specify only a suitable initial value, and for each time point the value is then automatically updated by the method based on the current state of the system. All relevant parameters and their values used for the different data sets are specified in Table 5.2. Notice that only minimal parameter changes (if any) were made to achieve optimal results for each data set, demonstrating the robustness of the algorithm.

5.3.3 Segmentation and Tracking Errors

A sample segmentation result produced by our algorithm is shown in Figure 5.6. The colored surfaces overlaid on the image data represent the segmented boundaries of each cell nucleus. Since ground truth data was not available, and manually creating a full segmentation was not feasible, only visual evaluation of the segmentation quality was possible. From the latter we concluded that, even at later stages of embryogenesis, with approximately 350 cells, the segmentations produced by our method are very realistic: in general the surfaces follow the shape of the object (spherical or elongated) and the separation surfaces between adjacent cells are positioned where they are naturally expected to be.

For the evaluation of the tracking performance of our algorithm, ground truth reference data was available (the well-known *C. elegans* lineage tree), and we used the same error measures as in [10] (all calculated per cell stage): the number of false positives (FP), false negatives (FN), mismatches (MM) per thousand nuclei, and the rate of erroneous divisions (ED). Since propagation of errors may have dramatic effects, errors were corrected (but counted) immediately after they occurred, and tracking was restarted after correction. Thus, all error measures directly correspond to the number of operations required to transform the tracked lineage into the reference one: adding (FN and ED) or removing (FP and ED) a branch and relinking (MM and ED) two branches of the tree.

Table 5.1: Microscope settings used for obtaining the test data sets.

Feature	Data Set 1	Data Set 2	Data Set 3	Data Set 4
Name	060809	100809	081505	20090505
Origin	Lehner Lab	Lehner Lab	Waterston Lab	Waterston Lab
Microscope	Leica TCS SP5	Leica TCS SP5	Zeiss LSM510	Zeiss LSM510
Objective	63 \times 1.4	63 \times 1.4	63 \times 1.4	63 \times 1.4
Zoom	3.4	3.4	2.3	2.3
Original stack size (voxels)	712 \times 512 \times 20	712 \times 512 \times 20	708 \times 512 \times 35	736 \times 512 \times 31
Cropped stack size (voxels)	570 \times 386 \times 20	550 \times 372 \times 20	550 \times 400 \times 26	540 \times 400 \times 27
XY resolution (μm)	0.13	0.13	0.09	0.09
Z resolution (μm)	1	1	1	1
Number of stacks analyzed	200	184	184	124
Temporal resolution (min)	1	1	1	1.5

Table 5.2: Algorithm parameter values used for the different test data sets.

Name	Description	Origin	060809	100809	081505	20090505
α	Contour smoothness	Set empirically	20	20	20	20
D_{max}	Maximal displacement of a daughter cell with respect to the mother cell	Detected from the data	50	40	50	75
$maxdispl$	Maximal displacement of a cell between two consecutive frames	Detected from the data	30	30	45	40
$minsize$	Minimal object size	Initial value set empirically	10 ³	2 \cdot 10 ³	10 ³	10 ³
$bandwidth$	Width of the narrow band around the object contour	Set empirically	3	3	3	5
t_{div}	Minimal time interval between two consecutive divisions of one cell	Detected from the data	5	5	5	5
A_b	Threshold for the major-to-minor-axis ratio	Detected from the data	1.2	1.2	1.2	1.2

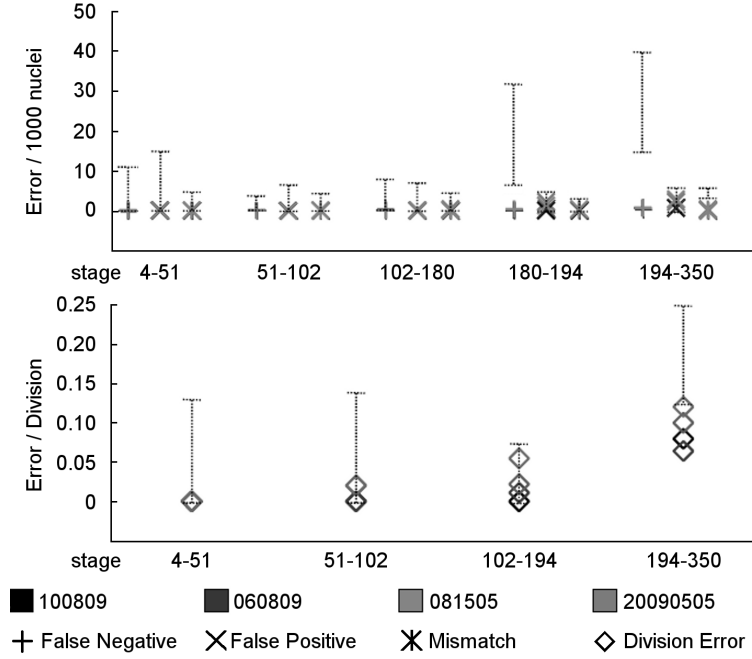


Figure. 5.5: Tracking performance of our method. The top plot shows the tracking performance of our method for the four test data sets in terms of false positives, false negatives, and mismatches, while the bottom plot shows the division errors. The results for the different data sets are indicated by different shades of gray, but if the error is the same for all four data sets, only one shade of gray is visible in the plots, as all symbols are plotted on top of each other. Error bars indicate the range (from minimal to maximal) of error values reported in the literature for StarryNite.

The error rates of our method and the corresponding maximal and minimal error values by StarryNite [10] are shown in Figure 5.5. The plots clearly indicate the superior performance of our method, especially in the earlier stages of embryonic development. In terms of FP, FN, and MM, our algorithm is perfect or near perfect until the 194-cell stage on all four data sets. From the 194-cell stage to the 350-cell stage, the number of errors increases, but still remains considerably lower than in the case of StarryNite. Of the three mentioned error measures, FN is the most significant: the other two types of errors are virtually absent, which is a direct consequence of using a model-evolution based approach. The ED rates of our method exhibit a natural increase as the number of cells grows, which can be explained by the higher cell density. Nevertheless, for all four test data sets, the ED rates until the 194-cell stage are very small and considerably lower than the maximal value by StarryNite, and between the 194-cell stage and the 350-cells stage even lower than the minimal value by StarryNite. Finally, an example of a lineage tree produced by our method for one of the data sets, is shown in Figure 5.7.

Table. 5.3: Average processing time in minutes of one image stack per time point.

Stage	4-cell	51-cell	102-cell	194-cell	350-cell
Time	0.5	1	1	2	4

5.3.4 Implementation and Processing Times

The algorithm was developed in the MATLAB (The MathWorks, Inc., USA) environment and the most computationally demanding operations were implemented in C. Average processing times of one image stack per time point on a standard PC (Intel(R) Xeon(R) CPU, 2.8 GHz, 6 GB RAM, running under Windows 7) are shown in Table 5.3.

5.4 Conclusions

A new method was presented for segmentation and tracking of a developing *C. elegans* embryo imaged by means of fluorescence microscopy. The algorithm uses a model-evolution approach, which proves to be an effective framework for the considered application, as it allows to easily exploit information from the previous time point for the segmentation of the current time point. Especially when segmenting and tracking highly clustered cells, this gives an advantage over methods that use completely separated cell detection and linking procedures. Experimental results on four data sets from two different laboratories demonstrated the superior performance of our method with respect to a current state-of-the art method. Our method is fully automated, meaning that user interaction is limited to providing a number of meaningful input parameters. However, intermediate manual error correction, which is mostly required during later stages of analysis, make the overall tracking more reliable. Our method can be used to replace a large amount of tedious human labor and, with minimal intervention, can significantly improve the productivity of the analysis of *C. elegans* embryogenesis fluorescence microscopy data.

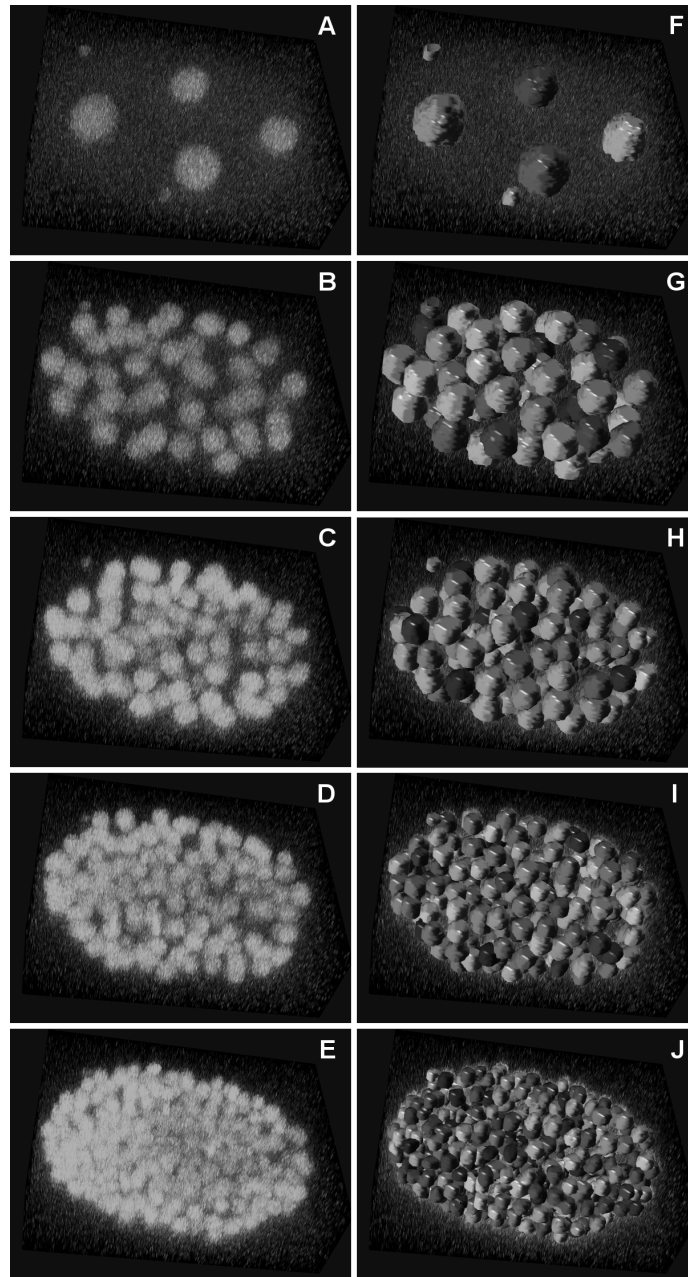


Figure. 5.6: Segmentation result for a sample data set. Original image stacks (A–E) from the 081505 data set (volume renderings) and the corresponding segmentation results (F–J) (surfaces rendered in arbitrary colors on top of the volume renderings) for the 4-cell ($t = 1$), 51-cell ($t = 74$), 102-cell ($t = 115$), 184-cell ($t = 138$), and 350-cell stage ($t = 184$).

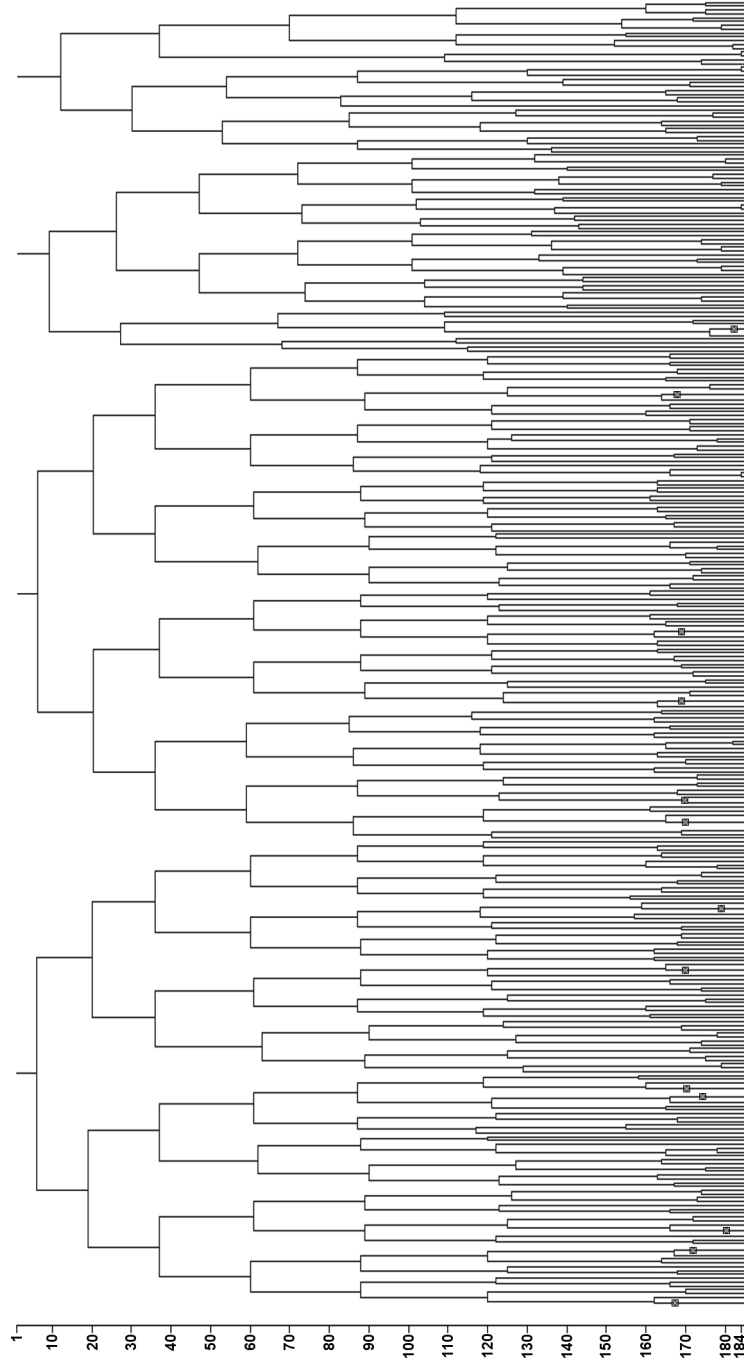
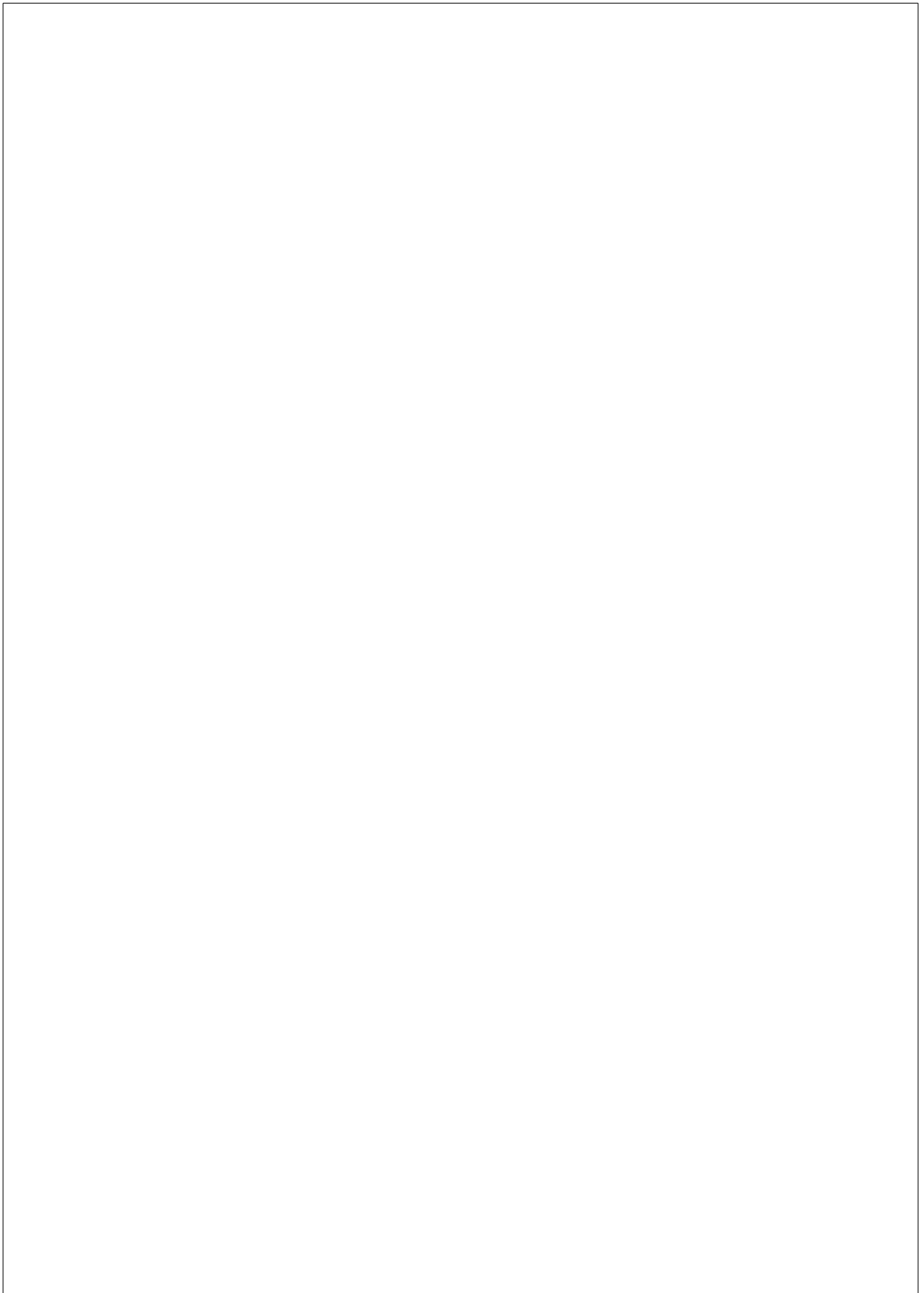


Figure 5.7: Sample lineage tree produced by our method. The tree covers the 4-cell stage ($t = 1$) until the 350-cell stage ($t = 184$) as tracked by our method in the 100809 data set. For obtaining this lineage tree, errors were corrected as a postprocessing step at the time step at which they occurred (indicated on the tree by the squares with the 'x' symbols).



Summary

In this thesis the challenge to automate the analysis of biological microscopy time-lapse image data is addressed. Three different levels of biological research: whole-organism, cellular and intracellular, are considered. The main goal of the work is to develop specialized methods for facilitating quantitative analysis of the fluorescence microscopy image data on each of the three mentioned levels that would complement or even completely replace human expertise. In order to provide a description of the imaged structure that is as realistic as possible, the developed tools make maximal use of the image information. For this purpose, several mathematical computer vision concepts are employed and customized for the given application. In particular, energy minimization methods, that allow combining information from different sources, are applied. Using mathematical methods not only helps to better analyze fluorescence microscopy time-lapse data, but also provides a theoretical basis for this kind of image analysis that would stimulate further biological research in this area.

In Chapter 2 an overview of the tracking and segmentation methods in fluorescence microscopy is given. This chapter discusses time-lapse analysis on different scales: whole-organism-, cellular- and intracellular, and how the results of these analyses can be combined. In particular, it is shown how information obtained from cell tracking and segmentation triggers analysis on the other two levels. It is also demonstrated that software tools for automated image analysis become now essential for performing research on fluorescence microscopy image data. The sophistication of these methods that is needed to be able to keep up with the growing complexity of the acquired images is continuously increasing. The main conclusion drawn from this chapter is that, even though many specialized computer tools for biological image analysis have been developed during past years, almost every particular application unavoidably requires creation of dedicated tools for analysis, processing and interpretation of the acquired image data. Keeping these observations in mind, a specialized framework for multi-level biological image analysis is developed in the following chapters of this thesis.

In Chapter 3 a specialized cell tracking and segmentation algorithm is developed and evaluated. This method belongs to the class of variational methods and allows

incorporation of prior information on object location (previous state) and appearance (intensity distribution, boundary smoothness) into one framework. The segmentation procedure at each time step is initialized with the result of the previous time step. A model evolution approach is used to find the new region which is occupied by the object. Hereto, an energy functional is minimized, which is built in such a way that it combines both intensity and smoothness information. Since at each iteration the energy minimization is performed only in a narrow band around the object, this approach at the same time achieves object tracking since it can be seen as continuous interpolation of the object's motion and deformation in the time interval between two successive acquisitions. Level-sets are used as the model because of their possibility to segment highly inhomogeneous regions, ability to change topology (this is especially useful for tracking dividing cells) and to work on data of arbitrary dimension.

During development of this algorithm, special attention was paid to quality improvement of both tracking and segmentation, since even small errors at this stage of analysis may have significant influence on analysis at the whole-organism and intracellular levels. Several important challenges that needed to be addressed included: reducing the number of required input parameters, handling of touching objects and of special division cases, improving initial segmentation, and convergence control. In the developed framework, all those issues were addressed, and for each of them novel or more efficient solutions were suggested. Considerable attention was also paid to computational aspects in order to make the methods suitable for high-throughput analysis. The method was validated on four different types of real time-lapse fluorescence microscopy sequences, and compared to both human experts (representing the gold standard) and other algorithms developed for the same purpose. The results showed that the level-set-based method in general outperforms all the other automated methods. Moreover, it is computationally efficient, unbiased, and has low sensitivity to input parameters, which makes it suitable for usage in a wide range of related biological applications.

As the next step in developing a system for multi-scale biological analysis, Chapter 4 describes a framework for performing intracellular analysis. This framework uses the results of the automated cell segmentation and tracking as input and performs the following tasks: cell motion correction, foci segmentation and foci analysis. The motion correction step is an important link between cell segmentation and tracking and intracellular analysis, as it allows separation of the intracellular dynamics from the global cell motion. In this work, this is achieved by registering all the regions occupied by the given object at different moments of time, which can be achieved by using the results of the segmentation and tracking algorithm. The potential to study intracellular dynamics is shown by analysis of fluorescent foci. Studying these foci is a very wide research field in modern biology. For segmenting foci, a multi-step scheme, including foci detection, segmentation, and selection based on statistical criteria was developed. The method is rather generic, as it incorporates only little prior information, so it can potentially be used for analysis of different foci types. The method was validated by repeating one entire foci-counting experiment that was earlier done manually. It is shown that both automated and manual methods lead to the same biological conclusions, which proves the potential of our

method in substituting human observers for performing such analyses. Finally, it is demonstrated how the statistics obtained after foci segmentation can be used for cell phase recognition of cells labeled with proliferating cell nuclear antigen (PCNA). In this case, each of the phases of the cell cycle is related to the typical pattern exhibited by the PCNA foci. Thus, analyzing relevant foci statistics (number, average size, intensity, distance to the nuclear envelope) enables recognition of the current phase of the cell cycle. The approach is very different from traditional approaches for cell phase recognition as it does not require prior training of the model.

Finally, in Chapter 5, the cell segmentation and tracking framework developed in Chapter 2 is applied to a very challenging problem: lineage construction of *C. elegans* embryogenesis. Using modern fluorescence microscopes, it is possible to follow the development of *C. elegans* from the single zygote stage to the complete adult organism. The spatial and temporal image resolution is sufficient to resolve different cells even at later stages of development and to be able to follow the same cell between two consecutive acquisitions. This makes fluorescent microscopy an excellent tool for *C. elegans*-related studies in developmental biology, where it is one of the most popular model organisms due to invariance of its lineage tree. However, creation of such lineage tree is a highly complex task, which at the present moment, except for the early stages of development, is mostly done manually, which is a tedious and error-prone procedure. Using the computer for performing these tasks not only drastically increases the productivity, but it also provides additional analysis opportunities. For example, having a method that can not only track, but also segment cells, enables analysis of expressions of different genes at each stage of the embryogenesis.

Our method, which is based on an energy minimization approach, can perform both the task of segmentation and tracking simultaneously. The level-set-based algorithm from Chapter 2 was considerably modified and extended to be able to handle these challenging data which contain more than 10000 cells in total at different moments of time. The complexity of the problem increases with cell stage (number of cells present), which, together with deteriorating image quality due to photobleaching and error propagation make tracking after a certain stage virtually impossible (the 350-cell stage being used as the current standard). Replacing the energy minimization via level-sets by a much faster graph-cut algorithm made it possible to perform segmentation of image stacks containing about 350 cells within reasonable time. In this case, the graph-cuts are minimized, similar to the level-sets, in a narrow band around the current region occupied by the object, which makes them suitable for tracking. Additionally, the method has special built-in algorithms for handling potential collisions between different objects and keeping track of dividing cells that rely on the prior information about the characteristic spherical shape of *C. elegans* nuclei and typical division pattern. Four data sets from two different laboratories were used for validation of our method. The results demonstrated that, using the suggested approach, it is possible to perform tracking and segmentation on the *C. elegans* embryogenesis data till at least the 350-cell stage. The described algorithm is fully automated, but using it in semi-automated mode, in which errors are corrected right after they happened for prevention of error propagation, provides better re-

sults. Thus, our method can already at this moment greatly simplify the work of biologists for analysis of *C. elegans* embryogenesis image data.

In conclusion, the work presented in this thesis demonstrates the potential of specialized software tools for the automated and quantitative analysis of biological time-lapse fluorescence microscopy data. In particular, such mathematical computer vision concepts as variational calculus, energy minimization, and partial differential equations have been employed and tailored to perform segmentation and tracking on different levels of biological research. The algorithms presented in this work were developed for solving a number of important practical problems rising during analysis of fluorescence microscopy data: cell tracking and segmentation, motion correction, intracellular analysis on fluorescent foci, and lineage construction of developing *C. elegans* embryos. Although the underlying techniques are quite generic, the methods were optimized for maximally extracting information from the given type of data, which may limit their direct application to other similar data types. Another potential drawback of the variational energy minimization methods is that they are in general rather slow, thus, for every particular application, the right balance between the precision of the results and the processing time has to be found. Resolving these issues will greatly increase the applicability of such methods to modern biological problems and potentially make them the main tool for high-throughput time-lapse image analysis.

Bibliography

- [1] W. M. Ahmed, S. J. Leavesley, B. Rajwa, M. N. Ayyaz, A. Ghafoor, and J. P. Robinson. State of the art in information extraction and quantitative analysis for multimodality biomolecular imaging. *Proceedings of the IEEE*, 96(3):512–531, March 2008.
- [2] O. Al-Kofahi, R. J. Radke, S. K. Goderie, Q. Shen, S. Temple, and B. Roysam. Automated cell lineage construction: A rapid method to analyze clonal development established with murine neural progenitor cells. *Cell Cycle*, 5(3):327–335, February 2006.
- [3] D. G. Altman. *Practical Statistics for Medical Research*. Chapman & Hall, London, UK, 1991.
- [4] L. Anderson, C. Henderson, and Y. Adachi. Phosphorylation and rapid relocation of 53BP1 to nuclear foci upon DNA damage. *Molecular and Cellular Biology*, 21(5):1719–1729, 2001.
- [5] S. Angenent, E. Pichon, and A. Tannenbaum. Mathematical methods in medical image processing. *Bulletin of the American Mathematical Society*, 43:365–396, 2006.
- [6] G. Aubert and P. Kornprobst. *Mathematical Problems in Image Processing: Partial Differential Equations and the Calculus of Variations (second edition)*, volume 147 of *Applied Mathematical Sciences*. Springer-Verlag, 2006.
- [7] Z. Aydin, J. I. Murray, R. H. Waterston, and W. S. Noble. Using machine learning to speed up manual image annotation: Application to a 3D imaging protocol for measuring single cell gene expression in the developing *C. elegans* embryo. *BMC Bioinformatics*, 11:84, 2010.
- [8] A. Bahnson, C. Athanassiou, D. Koebler, L. Qian, T. Shun, D. Shields, H. Yu, H. Wang, J. Goff, T. Cheng, R. Houck, and L. Cowser. Automated measurement of cell motility and proliferation. *BMC Cell Biology*, 6(1):19, 2005.
- [9] I. N. Bankman. *Handbook of Medical Image Processing and Analysis*. Academic Press, Burlington, MA, 2nd edition, 2008.
- [10] Z. Bao, J. I. Murray, T. Boyle, S. L. Ooi, M. J. Sandel, and R. H. Waterston. Automated cell lineage tracing in *Caenorhabditis elegans*. *Proceedings of the National Academy of Sciences of the United States of America*, 103(8):2707–2712, February 2006.
- [11] E. Betzig, G. H. Patterson, R. Sougrat, O. W. Lindwasser, S. Olenych, J. S. Bonifacino, M. W. Davidson, J. Lippincott-Schwartz, and H. F. Hess. Imaging intracellular fluorescent proteins at nanometer resolution. *Science*, 313(5793):1642–1645, September 2006.
- [12] W. Böcker and G. Iliakis. Computational methods for analysis of foci: Validation for radiation-induced γ -H2AX foci in human cells. *Radiation Research*, 165(1):113–124, January 2006.
- [13] J. Boulanger, C. Kervrann, and P. Bouthemy. Space-time adaptation for patch-based image sequence restoration. *IEEE Transactions on Pattern Analysis and Machine Intelligence*, 29:1096–1102, 2007.

- [14] A. W. Bowman and A. Azzalini. *Applied Smoothing Techniques for Data Analysis: The Kernel Approach with S-Plus Illustrations (Oxford Statistical Science Series)*. Oxford University Press, USA, November 1997.
- [15] Y. Boykov and V. Kolmogorov. Computing geodesics and minimal surfaces via graph cuts. In *International Conference on Computer Vision*, pages 26–33, 2003.
- [16] T. J. Boyle, Z. Bao, J. I. Murray, C. L. Araya, and R. H. Waterston. AceTree: A tool for visual analysis of *Caenorhabditis elegans* embryogenesis. *BMC Bioinformatics*, 7:275, June 2006.
- [17] K. Braeckmans, L. Peeters, N. N. Sanders, S. C. de Smedt, and J. Demeester. Three-dimensional fluorescence recovery after photobleaching with the confocal scanning laser microscope. *Biophysical Journal*, 85(4):2240–2252, 2003.
- [18] V. Braun, R. B. R. Azevedo, M. Gumbel, P.-M. Agapow, A. M. Leroi, and H.-P. Meinzer. ALES: Cell lineage analysis and mapping of developmental events. *Bioinformatics*, 19(7):851–858, May 2003.
- [19] G. Bunt and F. S. Wouters. Visualization of molecular activities inside living cells with fluorescent labels. *International Review of Cytology*, 237:205–277, 2004.
- [20] T. Byrt, J. Bishop, and J. B. Carlin. Bias, prevalence and kappa. *Journal of Clinical Epidemiology*, 46(5):423 – 429, 1993.
- [21] A. E. Carpenter, T. R. Jones, M. R. Lamprecht, C. Clarke, I. H. Kang, O. Friman, D. A. Guertin, J. H. Chang, R. A. Lindquist, J. Moffat, P. Golland, and D. M. Sabatini. Cellprofiler: Image analysis software for identifying and quantifying cell phenotypes. *Genome Biology*, 7(10):R100, 2006.
- [22] B. C. Carter, G. T. Shubeita, and S. P. Gross. Tracking single particles: A user-friendly quantitative evaluation. *Physical Biology*, 2(1):60–72, March 2005.
- [23] T. F. Chan and L. A. Vese. Active contours without edges. *IEEE Transactions on Image Processing*, 10(2):266–277, February 2001.
- [24] H. Chang, Q. Yang, and B. Parvin. Segmentation of heterogeneous blob objects through voting and level set formulation. *Pattern Recognition Letters*, 28(13):1781–1787, October 2007.
- [25] K. N. Chaudhury and K. R. Ramakrishnan. Stability and convergence of the level set method in computer vision. *Pattern Recognition Letters*, 28(7):884–893, May 2007.
- [26] M. K. Cheezum, W. F. Walker, and W. H. Guilford. Quantitative comparison of algorithms for tracking single fluorescent particles. *Biophysical Journal*, 81(4):2378–2388, October 2001.
- [27] X. Chen, X. Zhou, and S. T. C. Wong. Automated segmentation, classification, and tracking of cancer cell nuclei in time-lapse microscopy. *IEEE Transactions on Biomedical Engineering*, 53(4):762–766, April 2006.
- [28] Y. Chen, E. Ladi, P. Herzmark, E. Robey, and B. Roysam. Automated 5-D analysis of cell migration and interaction in the thymic cortex from time-lapse sequences of 3-D multi-channel multi-photon images. *Journal of Immunological Methods*, 340(1):65–80, January 2009.
- [29] Y. Chen, G. Lin, O. Al-Kofahi, W. A. Mohler, and B. Roysam. Automated extraction of cell lineages and spatial migration paths in live *c. elegans* embryos from 4D fluorescence microscopy image sequences. *Microscopy and Microanalysis*, 12(Supp 2):1672–1673, 2006.

- [30] M. Chicurel. Cell migration research is on the move. *Science*, 295(5555):606–609, January 2002.
- [31] C. J. Cronin, J. E. Mendel, S. Mukhtar, Y.-M. Kim, R. C. Stirbl, J. Bruck, and P. W. Sternberg. An automated system for measuring parameters of nematode sinusoidal movement. *BMC Genetics*, 6(1):5, February 2005.
- [32] J. Cui, S. T. Acton, and Z. Lin. A Monte Carlo approach to rolling leukocyte tracking in vivo. *Medical Image Analysis*, 10(4):598–610, August 2006.
- [33] R. B. D’Agostino, A. Belanger, and Jr. D’Agostino. A suggestion for using powerful and informative tests of normality. *The American Statistician*, 44(4):316–321, 1990.
- [34] S. R. Deans. *The Radon Transform and Some of Its Applications*. Krieger Publishing Company, Malabar, FL, 1992.
- [35] O. Debeir, I. Camby, R. Kiss, P. Van Ham, and C. Decaestecker. A model-based approach for automated in vitro cell tracking and chemotaxis analyses. *Cytometry Part A*, 60A(1):29–40, 2004.
- [36] O. Debeir, P. Van Ham, R. Kiss, and C. Decaestecker. Tracking of migrating cells under phase-contrast video microscopy with combined mean-shift processes. *IEEE Transactions on Medical Imaging*, 24(6):697–711, June 2005.
- [37] J. Degerman, T. Thorlin, J. Fajerson, K. Althoff, P. S. Eriksson, R. V. D. Put, and T. Gustavsson. An automatic system for in vitro cell migration studies. *Journal of Microscopy*, 233(1):178–191, January 2009.
- [38] B. Delaunay. Sur la sphère vide. *Izvestia Akademii Nauk SSSR, Otdelenie Matematicheskikh i Estestvennykh Nauk*, 7:793–800, 1934.
- [39] Z. N. Demou and L. V. McIntire. Fully automated three-dimensional tracking of cancer cells in collagen gels: Determination of motility phenotypes at the cellular level. *Cancer Research*, 62(18):5301–5307, 2002.
- [40] R. W. Dirks and H. J. Tanke. Advances in fluorescent tracking of nucleic acids in living cells. *BioTechniques*, 40(4):489–496, April 2006.
- [41] D. Dormann, T. Libotte, C. J. Weijer, and T. Bretschneider. Simultaneous quantification of cell motility and protein-membrane-association using active contours. *Cell Motility and the Cytoskeleton*, 52(4):221–230, August 2002.
- [42] D. Dormann and C. J. Weijer. Imaging of cell migration. *EMBO Journal*, 25(15):3480–3493, August 2006.
- [43] J. F. Dorn, G. Danuser, and G. Yang. Computational processing and analysis of dynamic fluorescence image data. *Methods in Cell Biology*, 85:497–538, 2008.
- [44] A. Dufour, V. Shinin, S. Tajbakhsh, N. Guillen-Aghion, J.-C. Olivo-Marin, and C. Zimmer. Segmenting and tracking fluorescent cells in dynamic 3-D microscopy with coupled active surfaces. *IEEE Transactions on Image Processing*, 14(9):1396–1410, September 2005.
- [45] J. S. Duncan and N. Ayache. Medical image analysis: Progress over two decades and the challenges ahead. *IEEE Transactions on Pattern Analysis and Machine Intelligence*, 22(1):85–106, January 2000.
- [46] O. Dzyubachyk, R. Jelier, B. Lehner, W. J. Niessen, and E. Meijering. Model-based approach for tracking embryogenesis in *caenorhabditis elegans* fluorescence microscopy data. In *Annual Conference of the IEEE Engineering in Medicine and Biology Society*, pages 5356–5359, 2009.

- [47] O. Dzyubachyk, W. Niessen, and E. Meijering. A variational model for level-set based cell tracking in time-lapse fluorescence microscopy images. In *Proceedings of the 2007 IEEE International Symposium on Biomedical Imaging: From Nano to Macro*, pages 97–100, Washington, DC, USA, April 2007. IEEE.
- [48] O. Dzyubachyk, W. Niessen, and E. Meijering. Advanced level-set based multiple-cell segmentation and tracking in time-lapse fluorescence microscopy images. In *Proceedings of the 2008 IEEE International Symposium on Biomedical Imaging: From Nano to Macro*, pages 185–188, Paris, France, May 2008. IEEE.
- [49] O. Dzyubachyk, W. A. van Cappellen, J. Essers, W. J. Niessen, and E. Meijering. Advanced level-set-based cell tracking in time-lapse fluorescence microscopy. *IEEE Transactions on Medical Imaging*, 29(3):852–867, March 2010.
- [50] R. Eils and C. Athale. Computational imaging in cell biology. *Journal of Cell Biology*, 161(3):477–481, May 2003.
- [51] I. Ersoy, F. Bunyak, V. Chagin, M. C. Cardoso, and K. Palaniappan. Segmentation and classification of cell cycle phases in fluorescence imaging. In Guang-Zhong Yang, David J. Hawkes, Daniel Rueckert, J. Alison Noble, and Chris J. Taylor, editors, *Medical Image Computing and Computer-Assisted Intervention - MICCAI 2009, 12th International Conference*, volume 5762 of *Lecture Notes in Computer Science*, pages 617–624, London, UK, September 20–24, 2009 2009. Springer.
- [52] J. Essers, A. F. Theil, C. Baldeyron, W. A. van Cappellen, A. B. Houtsmuller, R. Kanaar, and W. Vermeulen. Nuclear dynamics of PCNA in DNA replication and repair. *Molecular and Cellular Biology*, 25(21):9350–9359, November 2005.
- [53] J. Essers, W. A. van Cappellen, A. F. Theil, E. van Drunen, N. G. Jaspers, J. H. Hoeijmakers, C. Wyman, W. Vermeulen, and R. Kanaar. Dynamics of relative chromosome position during the cell cycle. *Molecular Biology of the Cell*, 16(2):769–775, February 2005.
- [54] S. V. Fomin and I. M. Gelfand. *Calculus of Variations*. Dover Publications, October 2000.
- [55] Y. Garini, B. J. Vermolen, and I. T. Young. From micro to nano: Recent advances in high-resolution microscopy. *Current Opinion in Biotechnology*, 16(1):3–12, February 2005.
- [56] W. Geng, P. Cosman, C. C. Berry, Z. Feng, and W. R. Schafer. Automatic tracking, feature extraction and classification of *C. elegans* phenotypes. *IEEE Transactions on Biomedical Engineering*, 51(10):1811–1820, October 2004.
- [57] D. Gerlich and J. Ellenberg. 4D imaging to assay complex dynamics in live specimens. *Nature Cell Biology*, 5:S14–S19, September 2003.
- [58] D. Gerlich, J. Mattes, and R. Eils. Quantitative motion analysis and visualization of cellular structures. *Methods*, 29(1):3–13, January 2003.
- [59] S. F. Gibson and F. Lanni. Experimental test of an analytical model of aberration in an oil-immersion objective lens used in three-dimensional light microscopy. *Journal of the Optical Society of America A: Optics and Image Science*, 8(10):1601–1613, 1991.
- [60] B. N. G. Giepmans, S. R. Adams, M. H. Ellisman, and R. Y. Tsien. The fluorescent toolbox for assessing protein location and function. *Science*, 312(5771):217–224, April 2006.
- [61] R. C. Gonzalez and R. E. Woods. *Digital Image Processing*. Prentice Hall, Upper Saddle River, N.J., 2008.
- [62] A. Gordon, A. Colman-Lerner, T. E. Chin, K. R. Benjamin, R. C. Yu, and R. Brent. Single-cell quantification of molecules and rates using open-source microscope-based cytometry. *Nature Methods*, 4(2):175–181, February 2007.

- [63] F. E. Grubbs. Procedures for detecting outlying observations in samples. *Technometrics*, 11(1):1–21, 1969.
- [64] M. Gué, C. Messaoudi, J. S. Sun, and T. Boudier. Smart 3D-FISH: Automation of distance analysis in nuclei of interphase cells by image processing. *Cytometry Part A*, 67(1):18–26, 2005.
- [65] S. Hamahashi, S. Onami, and H. Kitano. Detection of nuclei in 4D Nomarski DIC microscope images of early *Caenorhabditis elegans* embryos using local image entropy and object tracking. *BMC Bioinformatics*, 6:125, May 2005.
- [66] J. Han, H. Chang, Q. Yang, M. H. Barcellos-Hoff, and B. Parvin. 3D segmentation of mammospheres for localization studies. In *International Symposium on Visual Computing*, volume 4291 of *Lecture Notes in Computer Science*, pages 518–527, Berlin, 2006. Springer.
- [67] A. J. Hand, T. Sun, D. C. Barber, D. R. Hose, and S. MacNeil. Automated tracking of migrating cells in phase-contrast video microscopy sequences using image registration. *Journal of Microscopy*, 234(1):62–79, April 2009.
- [68] N. Harder, F. Mora-Bermúdez, W. Godinez, J. Ellenberg, R. Eils, and K. Rohr. Automated analysis of the mitotic phases of human cells in 3D fluorescence microscopy image sequences. In *Medical Image Computing and Computer-Assisted Intervention*, volume 4190 of *Lecture Notes in Computer Science*, pages 840–848. Springer, Berlin, 2006.
- [69] J. A. Hartigan and P. M. Hartigan. The Dip Test of Unimodality. *The Annals of Statistics*, 13(1):70–84, 1985.
- [70] P. J. Heid, E. Voss, and D. R. Soll. 3D-DIASemb: A computer-assisted system for reconstructing and motion analyzing in 4D every cell and nucleus in a developing embryo. *Developmental Biology*, 245(2):329–347, 2002.
- [71] S. W. Hell. Microscopy and its focal switch. *Nature Methods*, 6(1):24–32, January 2009.
- [72] L. W. Hillier, A. Coulson, J. I. Murray, Z. Bao, J. E. Sulston, and R. H. Waterston. Genomics in *C. elegans*: So many genes, such a little worm. *Genome Research*, 15(12):1651–1660, December 2005.
- [73] K. Hoshi and R. Shingai. Computer-driven automatic identification of locomotion states in *Caenorhabditis elegans*. *Journal of Neuroscience Methods*, 157(2):355–363, October 2006.
- [74] A. B. Houtsmuller and W. Vermeulen. Macromolecular dynamics in living cell nuclei revealed by fluorescence redistribution after photobleaching. *Histochemistry and Cell Biology*, 115(1):13–21, January 2001.
- [75] B. Huang, W. Wang, M. Bates, and X. Zhuang. Three-Dimensional Super-Resolution Imaging by Stochastic Optical Reconstruction Microscopy. *Science*, 319(5864):810–813, February 2008.
- [76] A. Inagaki, W. A. van Cappellen, R. van der Laan, A. B. Houtsmuller, J. H. Hoeijmakers, J. A. Grootegeod, and W. M. Baarends. Dynamic localization of human RAD18 during the cell cycle and a functional connection with DNA double-strand break repair. *DNA Repair*, 8(2):190–201, 2009.
- [77] N. N. Kachouie, P. Fieguth, J. Ramunas, and E. Jervis. Probabilistic model-based cell tracking. *International Journal of Biomedical Imaging*, 2006(12186):1–10, 2006.
- [78] Y. Kalaidzidis. Multiple objects tracking in fluorescence microscopy. *Journal of Mathematical Biology*, 58(1-2):57–80, January 2009.
- [79] P. J. Keller, A. D. Schmidt, J. Wittbrodt, and E. H. K. Stelzer. Reconstruction of zebrafish early embryonic development by scanned light sheet microscopy. *Science*, 322(5904):1065–1069, November 2008.

- [80] C. G. Kevil, A. W. Orr, W. Langston, K. Mickett, J. Murphy-Ullrich, R. P. Patel, D. F. Kucik, and D. C. Bullard. Inter cellular adhesion molecule-1 (ICAM-1) regulates endothelial cell motility through a nitric oxide-dependent pathway. *The Journal of Biological Chemistry*, 279(18):19230–19238, April 2004.
- [81] Z. Khan, T. R. Balch, and F. Dellaert. MCMC-based particle filtering for tracking a variable number of interacting targets. *IEEE Transactions on Pattern Analysis and Machine Intelligence*, 27(11):1805–1819, November 2005.
- [82] I.-H. Kim, S. Yang, P. Le Baccon, E. Heard, C. Kappel, R. Eils, and K. Rohr. Non-rigid temporal alignment of 2D and 3D multi-channel microscopy image sequences of human cells. In *Bildverarbeitung für die Medizin*, pages 16–20, 2007.
- [83] M. Kozubek, S. Kozubek, E. Lukasova, A. Mareckova, E. Bartova, M. Skalnikova, and A. Jergova. High-resolution cytometry of FISH dots in interphase cell nuclei. *Cytometry Part A*, 36(4):279–293, 1999.
- [84] K. Krissian and C.-F. Westin. Fast sub-voxel re-initialization of the distance map for level set methods. *Pattern Recognition Letters*, 26(10):1532–1542, October 2005.
- [85] M. R. Lamprecht, D. M. Sabatini, and A. E. Carpenter. Cellprofiler: Free, versatile software for automated biological image analysis. *BioTechniques*, 42(1):71–75, January 2007.
- [86] A. E. Lefohn, J. M. Kniss, C. D. Hansen, and R. T. Whitaker. A streaming narrow-band algorithm: Interactive computation and visualization of level sets. *IEEE Transactions on Visualization and Computer Graphics*, 10(4):422–433, July-August 2004.
- [87] H. Leonhardt, H.-P. Rahn, P. Weinzierl, A. Sporbert, T. Cremer, D. Zink, and C. M. Cardoso. Dynamics of dna replication factories in living cells. *Journal of Cell Biology*, 149(2):271–280, April 2000.
- [88] F. Li, X. Zhou, J. Zhu, J. Ma, X. Huang, and S. T. C. Wong. High content image analysis for human H4 neuroglioma cells exposed to CuO nanoparticles. *BMC Biotechnology*, 7:66, October 2007.
- [89] G. Li, T. Liu, A. Tarokh, J. Nie, L. Guo, A. Mara, S. Holley, and S. T. C. Wong. 3D cell nuclei segmentation based on gradient flow tracking. *BMC Cell Biology*, 8:40, 2007.
- [90] K. Li, E. D. Miller, M. Chen, T. Kanade, L. E. Weiss, and P. G. Campbell. Cell population tracking and lineage construction with spatiotemporal context. *Medical Image Analysis*, 12(5):546–566, October 2008.
- [91] J. W. Lichtman and J.-A. Conchello. Fluorescence microscopy. *Nature Methods*, 2(12):910–919, December 2005.
- [92] G. Lin, M. K. Chawla, K. Olson, C. A. Barnes, J. F. Guzowski, C. Bjornsson, W. Shain, and B. Roysam. A multi-model approach to simultaneous segmentation and classification of heterogeneous populations of cell nuclei in 3D confocal microscope images. *Cytometry Part A*, 71(9):724–736, September 2007.
- [93] J. Lippincott-Schwartz, N. Altan-Bonnet, and G. H. Patterson. Photobleaching and photoactivation: Following protein dynamics in living cells. *Nature Cell Biology*, 5:S7–S13, September 2003.
- [94] J. Lippincott-Schwartz and G. H. Patterson. Development and use of fluorescent protein markers in living cells. *Science*, 300(5616):87–91, April 2003.
- [95] F. Long, H. Peng, X. Liu, S. K. Kim, and E. Myers. A 3d digital atlas of c. elegans and its application to single-cell analyses. *Nature Methods*, 6(9):667–672, September 2009.

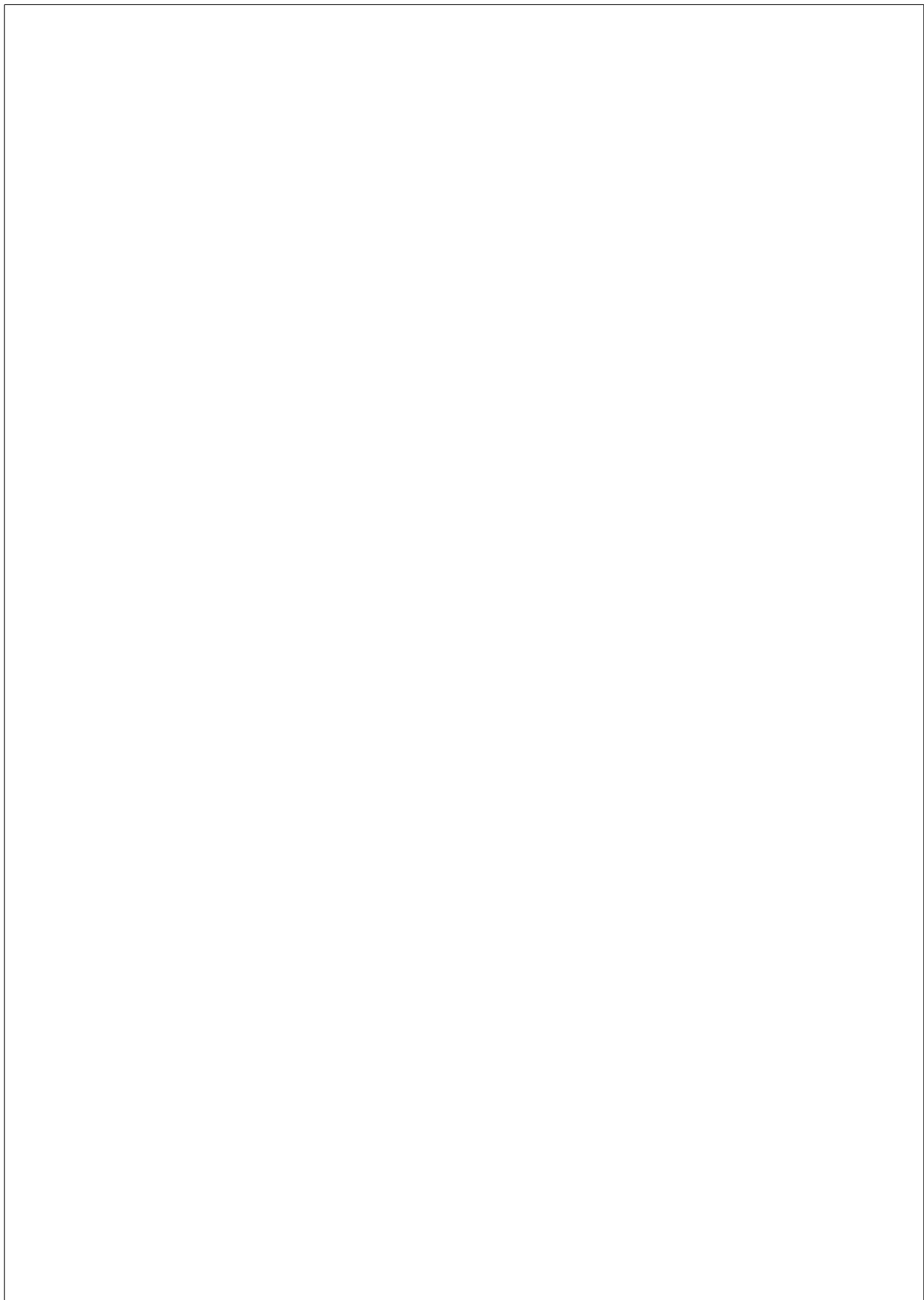
- [96] D. G. Lowe. *Perceptual organization and visual recognition*. PhD thesis, Stanford, CA, USA, 1985.
- [97] J. Malcolm, Y. Rath, and A. Tannenbaum. Multi-object tracking through clutter using graph cuts. In *Workshop on Non-rigid Registration and Tracking through Learning*, pages 1–5, 2007.
- [98] J. R. Mansfield, K. W. Gossage, C. C. Hoyt, and R. M. Levenson. Autofluorescence removal, multiplexing, and automated analysis methods for in-vivo fluorescence imaging. *Journal of Biomedical Optics*, 10(4):41207, August 2005.
- [99] J. Mattes, J. Nawroth, P. Boukamp, R. Eils, and K. M. Greulich-Bode. Analyzing motion and deformation of the cell nucleus for studying co-localizations of nuclear structures. In *Proceedings of the 2006 IEEE International Symposium on Biomedical Imaging: From Nano to Macro*, pages 1044–1047, Arlington, VA, USA, 6–9 April 2006.
- [100] P. Matula, P. Matula, M. Kozubek, and V. Dvořák. Fast point-based 3-D alignment of live cells. *IEEE Transactions on Image Processing*, 15(8):2388–2396, August 2006.
- [101] D. P. McCullough, P. R. Gudla, B. S. Harris, J. A. Collins, K. J. Meaburn, M. A. Nakaya, T. P. Yamaguchi, T. Misteli, and S. J. Lockett. Segmentation of whole cells and cell nuclei from 3-D optical microscope images using dynamic programming. *IEEE Transactions on Medical Imaging*, 27(5):723–734, May 2008.
- [102] E. Meijering, O. Dzyubachyk, I. Smal, and W. A. van Cappellen. Tracking in cell and developmental biology. *Seminars in Cell and Developmental Biology*, 20(8):894–902, October 2009.
- [103] E. Meijering, I. Smal, and G. Danuser. Tracking in molecular bioimaging. *IEEE Signal Processing Magazine*, 23(3):46–53, 2006.
- [104] E. Meijering, I. Smal, O. Dzyubachyk, and J.-C. Olivo-Marin. Time-lapse imaging. In Q. Wu, F. A. Merchant, and K. R. Castleman, editors, *Microscope Image Processing*, chapter 15, pages 401–440. Academic Press, Burlington, MA, 2008.
- [105] P. Meister, A. Taddei, A. Ponti, G. Baldacci, and S. Gasser. Replication foci dynamics: Replication patterns are modulated by S-phase checkpoint kinases in fission yeast. *EMBO Journal*, 26(5):1315–1326, 2007.
- [106] M. Moser, M. Frühwirth, and T. Kenner. The symphony of life: Importance, interaction, and visualization of biological rhythms. *IEEE Engineering in Medicine and Biology Magazine*, 27(1):29–37, January 2008.
- [107] D. P. Mukherjee, N. Ray, and S. T. Acton. Level set analysis for leukocyte detection and tracking. *IEEE Transactions on Medical Imaging*, 13(4):562–572, April 2004.
- [108] R. F. Murphy, E. Meijering, and G. Danuser. Special issue on molecular and cellular bioimaging. *IEEE Transactions on Image Processing*, 14(9):1233–1236, September 2005.
- [109] J. I. Murray, Z. Bao, T. J. Boyle, M. E. Boeck, B. L. Mericle, T. J. Nicholas, Z. Zhao, M. J. Sandel, and R. H. Waterston. Automated analysis of embryonic gene expression with cellular resolution in *C. elegans*. *Nature Methods*, 5(8):703–709, August 2008.
- [110] J. I. Murray, Z. Bao, T. J. Boyle, and R. H. Waterston. The lineaging of fluorescently-labeled *Caenorhabditis elegans* embryos with StarryNite and AceTree. *Nature Protocols*, 1(3):1468–1476, November 2006.
- [111] S. K. Nath, K. Palaniappan, and F. Bunyak. Cell segmentation using coupled level sets and graph-vertex coloring. In *Medical Image Computing and Computer-Assisted Intervention*, volume 4190 of *Lecture Notes in Computer Science*, pages 840–848, Berlin, 2006. Springer.

- [112] H. Netten, L. J. van Vliet, H. Vrolijk, W. C. R. Sloos, H. J. Tanke, and I. T. Young. Fluorescent dot counting in interphase cell nuclei. *Bioimaging*, 4(2):93–106, 1996.
- [113] H. Netten, I. T. Young, L. J. van Vliet, H. J. Tanke, H. Vrolijk, and W. C. R. Sloos. FISH and chips: Automation of fluorescent dot counting in interphase cell nuclei. *Cytometry*, 28(1):1–10, 1997.
- [114] S. J. Osher and R. P. Fedkiw. *Level Set Methods and Dynamic Implicit Surfaces*. Springer, Berlin, 2002.
- [115] D. Padfield, J. Rittscher, N. Thomas, and B. Roysam. Spatio-temporal cell cycle phase analysis using level sets and fast marching methods. *Medical Image Analysis*, 13(1):143–155, February 2009.
- [116] D. R. Padfield, J. Rittscher, and B. Roysam. Spatio-temporal cell segmentation and tracking for automated screening. In *Proceedings of the 2008 IEEE International Symposium on Biomedical Imaging: From Nano to Macro*, pages 376–379, Paris, France, May 2008. IEEE.
- [117] A. Paganin-Gioanni, E. Bellard, B. Couderc, J. Teissie, and M. Golzio. Tracking in vitro and in vivo siRNA electrotransfer in tumor cells. *Journal of RNAi and Gene Silencing*, 4(1):281–288, May 2008.
- [118] N. Panchuk-Voloshina, J. Bishop-Stewart, M. K. Bhalgat, P. J. Millard, F. Mao, W. Y. Leung, and R. P. Haugland. Alexa dyes, a series of new fluorescent dyes that yield exceptionally bright, photostable conjugates. *Journal of Histochemistry and Cytochemistry*, 47(9):1179–88, August 1999.
- [119] N. Paragios, Y. Chen, and O. Faugeras. *Handbook of Mathematical Models in Computer Vision*. Springer-Verlag New York, Inc., Secaucus, NJ, USA, 2005.
- [120] N. Paragios and R. Deriche. Geodesic active regions and level set methods for supervised texture segmentation. *International Journal of Computer Vision*, 46(3):223–247, February 2002.
- [121] N. Paragios, M. Rousson, and V. Ramesh. Non-rigid registration using distance functions. *Computer Vision and Image Understanding*, 89(2-3):142–165, 2003.
- [122] J. B. Pawley. *Handbook of Biological Confocal Microscopy*. Springer, New York, 3rd edition, 2006.
- [123] H. Peng. Bioimage informatics: A new area of engineering biology. *Bioinformatics*, 24(17):1827–1836, September 2008.
- [124] R. Pepperkok and J. Ellenberg. High-throughput fluorescence microscopy for systems biology. *Nature Reviews Molecular Cell Biology*, 7(9):690–696, September 2006.
- [125] Z. Pincus and J. A. Theriot. Comparison of quantitative methods for cell-shape analysis. *Journal of Microscopy*, 227(2):140–156, August 2007.
- [126] F. Raimondo, M. A. Gavrielides, G. Karayannopoulou, K. Lyroutdia, I. Pitas, and I. Kostopoulos. Automated evaluation of her-2/neu status in breast tissue from fluorescent in situ hybridization images. *IEEE Transactions on Image Processing*, 14(9):1288–1299, 2005.
- [127] N. Ray and S. T. Acton. Motion gradient vector flow: An external force for tracking rolling leukocytes with shape and size constrained active contours. *IEEE Transactions on Medical Imaging*, 23(12):1466–1478, 2004.
- [128] N. Ray, S. T. Acton, and K. Ley. Tracking leukocytes *in vivo* with shape and size constrained active contours. *IEEE Transactions on Medical Imaging*, 21(10):1222–1235, 2002.

- [129] J. Rittscher, R. Machiraju, and S. T. C. Wong. *Microscopic Image Analysis for Life Science Applications*. Artech House, Norwood, MA, 2008.
- [130] A. Rodrigue, M. Lafrance, M.-C. Gauthier, D. McDonald, M. Hendzel, S. C. West, M. Jasin, and J.-Y. Masson. Interplay between human DNA repair proteins at a unique double-strand break in vivo. *EMBO Journal*, 25(1):222–231, 2006.
- [131] N. Roussel, C. A. Morton, F. P. Finger, and B. Roysam. A computational model for *C. elegans* locomotory behavior: Application to multiworm tracking. *IEEE Transactions on Biomedical Engineering*, 54(10):1786–1797, October 2007.
- [132] M. Rousson and R. Deriche. A variational framework for active and adaptative segmentation of vector valued images. In *MOTION '02: Proceedings of the Workshop on Motion and Video Computing*, page 56, Washington, DC, 2002. IEEE Computer Society.
- [133] S. Särkkä, A. Vehtari, and J. Lampinen. Rao-Blackwellized Monte Carlo data association for multiple target tracking. In Per Svensson and Johan Schubert, editors, *Proceedings of the Seventh International Conference on Information Fusion*, volume I, pages 583–590, Mountain View, CA, June 2004. International Society of Information Fusion.
- [134] M. Sezgin and B. Sankur. Survey over image thresholding techniques and quantitative performance evaluation. *Journal of Electronic Imaging*, 13(1):146–168, 2004.
- [135] H. Shen, G. Nelson, S. Kennedy, D. Nelson, J. Johnson, D. Spiller, M. R. H. White, and D. B. Kell. Automatic tracking of biological cells and compartments using particle filters and active contours. *Chemometrics and Intelligent Laboratory Systems*, 82(1-2):276–282, 2006.
- [136] A. Sigal, R. Milo, A. Cohen, N. Geva-Zatorsky, Y. Klein, I. Alaluf, N. Swerdlin, N. Perzov, T. Danon, Y. Liron, T. Raveh, A. E. Carpenter, G. Lahav, and U. Alon. Dynamic proteomics in individual human cells uncovers widespread cell-cycle dependence of nuclear proteins. *Nature Methods*, 3(7):525–531, July 2006.
- [137] I.-M. Sintorn and G. Borgefors. Weighted distance transforms for volume images digitized in elongated voxel grids. *Pattern Recognition Letters*, 25(5):571–580, April 2004.
- [138] I. Smal, E. Meijering, K. Draegestein, N. Galjart, I. Grigoriev, A. Akhmanova, M. E. van Royen, A. B. Houtsmuller, and W. Niessen. Multiple object tracking in molecular bioimaging by Rao-Blackwellized marginal particle filtering. *Medical Image Analysis*, 12(6):764–777, December 2008.
- [139] I. Smal, W. Niessen, and E. Meijering. A new detection scheme for multiple object tracking in fluorescence microscopy by joint probabilistic data association filtering. In *Proceedings of the 2008 IEEE International Symposium on Biomedical Imaging: From Nano to Macro*, pages 264–267, Paris, France, May 2008. IEEE.
- [140] K. Smith, D. Gatica-Perez, and J.-M. Odobez. Using particles to track varying number of interacting people. In *Proceedings of IEEE Conference on Computer Vision and Pattern Recognition*, volume 1, pages 962–969, June 2005.
- [141] B. Song. *Topics in Variational PDE Image Segmentation, Inpainting and Denoising*. PhD thesis, University of California, Los Angeles, USA, 2003.
- [142] D. J. Stephens and V. J. Allan. Light microscopy techniques for live cell imaging. *Science*, 300(5616):82–86, April 2003.
- [143] J. E. Sulston, E. Schierenberg, J. G. White, and J. N. Thomson. The embryonic cell lineage of the nematode *Caenorhabditis elegans*. *Developmental Biology*, 100(1):64–119, November 1983.

- [144] J. S. Suri, D. Wilson, and S. Laximinarayan. *Handbook of Biomedical Image Analysis*. Kluwer Academic / Plenum Publishers, New York, NY, 2005.
- [145] J. R. Swedlow, I. Goldberg, E. Brauner, and P. K. Sorger. Informatics and quantitative analysis in biological imaging. *Science*, 300(5616):100–102, 2003.
- [146] J. R. Swedlow, S. E. Lewis, and I. G. Goldberg. Modelling data across labs, genomes, space and time. *Nature Cell Biology*, 8(11):1190–1194, November 2006.
- [147] O. Tassy, F. Daian, C. Hudson, V. Bertrand, and P. Lemaire. A quantitative approach to the study of cell shapes and interactions during early chordate embryogenesis. *Current Biology*, 16(4):345–358, February 2006.
- [148] N. Thomas. Lighting the circle of life: Fluorescent sensors for covert surveillance of the cell cycle. *Cell Cycle*, 2(6):545–549, November/December 2003.
- [149] L. Trinkle-Mulcahy, P. D. Andrews, S. Wickramasinghe, J. Sleeman, A. Prescott, Y. W. Lam, C. Lyon, J. R. Swedlow, and A. I. Lamond. Time-lapse imaging reveals dynamic relocation of PP1 γ throughout the mammalian cell cycle. *Molecular Biology of the Cell*, 14:107–117, January 2003.
- [150] R. Y. Tsien. The green fluorescent protein. *Annual Review of Biochemistry*, 67:509–544, 1998.
- [151] R. Y. Tsien. Imagining imaging’s future. *Nature Reviews Molecular Cell Biology*, 4:S16–S21, September 2003.
- [152] C. van Rijsbergen. *Information Retrieval*. Butterworth, London, U.K., 2nd edition, 1979.
- [153] N. Vaswani, A. Tannenbaum, and A. Yezzi. Tracking deforming objects using particle filtering for geometric active contours. *IEEE Transactions on Pattern Analysis and Machine Intelligence*, 29(8):1470–1475, August 2007.
- [154] J. Vermot, S. E. Fraser, and M. Liebling. Fast fluorescence microscopy for imaging the dynamics of embryonic development. *HFSP Journal*, 2(3):143–155, June 2008.
- [155] L. Vincent and P. Soille. Watersheds in digital spaces: An efficient algorithm based on immersion simulations. *IEEE Transactions on Pattern Analysis and Machine Intelligence*, 13(6):583–598, June 1991.
- [156] C. Vonesch, F. Aguet, J.-L. Vonesch, and M. Unser. The colored revolution of bioimaging. *IEEE Signal Processing Magazine*, 23(3):20–31, May 2006.
- [157] C. Wählby, I.-M. Sintorn, F. Erlandsson, G. Borgefors, and E. Bengtsson. Combining intensity, edge and shape information for 2D and 3D segmentation of cell nuclei in tissue sections. *Journal of Microscopy*, 215(1):67–76, July 2004.
- [158] P. K. Wallace and K. A. Muirhead. Cell tracking 2007: A proliferation of probes and applications. *Immunological Investigations*, 36(5-6):527–561, September 2007.
- [159] T. Walter, M. Held, B. Neumann, J.-K. Heriche, C. Conrad, R. Pepperkok, and J. Ellenberg. High-throughput RNAi screening by time-lapse imaging of live human cells. *Nature Methods*, 3(5):385–390, May 2006.
- [160] M. Wang, X. Zhou, F. Li, J. Huckins, R. W. King, and S. T. C. Wong. Novel cell segmentation and online SVM for cell cycle phase identification in automated microscopy. *Bioinformatics*, 24(1):94–101, January 2008.
- [161] S. K. Warfield, K. H. Zou, and W. M. Wells. Simultaneous truth and performance level estimation (STAPLE): An algorithm for the validation of image segmentation. *IEEE Transactions on Medical Imaging*, 23(7):903–921, July 2004.

- [162] R. Waterston and J. Sulston. The genome of *Caenorhabditis elegans*. *Proceedings of the National Academy of Sciences of the United States of America*, 92(24):10836–10840, November 1995.
- [163] D. J. Webb and A. F. Horwitz. New dimensions in cell migration. *Nature Cell Biology*, 5(8):690–692, August 2003.
- [164] Q. Wen, J. Gao, and K. Luby-Phelps. Multiple interacting subcellular structure tracking by sequential Monte Carlo method. In *Proceedings of the IEEE International Conference on Bioinformatics and Biomedicine*, pages 437–442, 2007.
- [165] C. A. Wilson and J. A. Theriot. A correlation-based approach to calculate rotation and translation of moving cells. *IEEE Transactions on Image Processing*, 15(7):1939–1951, July 2006.
- [166] Q. Wu, F. A. Merchant, and K. R. Castleman. *Microscope Image Processing*. Academic Press, Burlington, MA, 2008.
- [167] J. Xie, S. Khan, and M. Shah. Automatic tracking of *Escherichia coli* in phase-contrast microscopy video. *IEEE Transactions on Biomedical Engineering*, 56(2):390–399, February 2009.
- [168] F. Yang, M. A. Mackey, F. Ianzini, G. Gallardo, and M. Sonka. Cell segmentation, tracking, and mitosis detection using temporal context. In James S. Duncan and Guido Gerig, editors, *Medical Image Computing and Computer-Assisted Intervention*, volume 3749 of *Lecture Notes in Computer Science*, pages 302–309, Berlin, 2005. Springer.
- [169] S. Yang, D. Kohler, K. Teller, T. Cremer, P. Le Baccon, E. Heard, R. Eils, and K. Rohr. Nonrigid registration of 3-D multichannel microscopy images of cell nuclei. *IEEE Transactions on Image Processing*, 17(4):493–499, April 2008.
- [170] X. Yang, H. Li, and X. Zhou. Nuclei segmentation using marker-controlled watershed, tracking using mean-shift, and Kalman filter in time-lapse microscopy. *IEEE Transactions on Circuits and Systems I: Regular Papers*, 53(11):2405–2414, November 2006.
- [171] A. J. Yezzi and S. Soatto. Deformation: Deforming motion, shape average and the joint registration and approximation of structures in images. *International Journal of Computer Vision*, 53(2):153–167, 2003.
- [172] X. Zhou, F. Li, J. Yan, and S. T. C. Wong. A novel cell segmentation method and cell phase identification using Markov model. *IEEE Transactions on Information Technology in Biomedicine*, 13(2):152–157, March 2009.
- [173] X. Zhou and S. T. C. Wong. Informatics challenges of high-throughput microscopy. *IEEE Signal Processing Magazine*, 23(3):63–72, May 2006.
- [174] C. Zimmer, E. Labruyère, V. Meas-Yedid, N. Guillén, and J.-C. Olivo-Marin. Segmentation and tracking of migrating cells in videomicroscopy with parametric active contours: A tool for cell-based drug testing. *IEEE Transactions on Medical Imaging*, 21(10):1212–1221, October 2002.
- [175] C. Zimmer and J.-C. Olivo-Marin. Coupled parametric active contours. *IEEE Transactions on Pattern Analysis and Machine Intelligence*, 27(11):1838–1842, November 2005.
- [176] C. Zimmer, B. Zhang, A. Dufour, A. Thébaud, S. Berlemont, V. Meas-Yedid, and J.-C. Olivo-Marin. On the digital trail of mobile cells. *IEEE Signal Processing Magazine*, 23(3):54–62, May 2006.
- [177] B. Zitova and J. Flusser. Image registration methods: A survey. *Image and Vision Computing*, 21(11):977–1000, October 2003.



Samenvatting

Het thema van dit proefschrift is de ontwikkeling en evaluatie van automatische methoden voor de analyse van beeldseries van biologische processen verkregen met behulp van fluorescentie microscopie. Daarbij worden drie schaalniveaus onderscheiden: het hele organisme, het cellulaire niveau, en het intracellulaire niveau. Het voornaamste doel van het beschreven werk is het vergemakkelijken van de kwantitatieve analyse van beelden op elk van de drie genoemde niveaus, ter ondersteuning of zelfs volledige vervanging van de analyse door menselijke experts. Om te komen tot een zo nauwkeurig mogelijke beschrijving van de relevante biologische structuren, dienen automatische methoden optimaal gebruik te maken van de beschikbare beeldinformatie. Om dit te bewerkstelligen worden in dit proefschrift verschillende wiskundige concepten ontwikkeld en verfijnd. In het bijzonder wordt gekeken naar zogenaamde energieminimalisatiemethoden, welke het mogelijk maken om verschillende soorten informatie te combineren. Het gebruik van wiskundige modellen ondersteunt niet alleen de analyse in microscopische beeldseries, maar verschaft ook een theoretische basis voor dergelijke analyses, die verder biologisch onderzoek kan stimuleren.

In Hoofdstuk 2 wordt een overzicht gegeven van methoden voor het volgen en segmenteren van objecten in fluorescentie microscopie beelden. Het hoofdstuk bespreekt de analyse van beeldseries op de drie genoemde schaalniveaus, en hoe de resultaten van deze analyses kunnen worden gecombineerd. In het bijzonder wordt duidelijk gemaakt dat het volgen van cellen van cruciaal belang is voor analyses op zowel het cellulaire niveau alsook op het niveau van het hele organisme en van intracellulaire processen. Tevens wordt gewezen op de toenemende noodzaak van het ontwikkelen van automatische methoden en software tools voor dergelijke analyses. De groeiende omvang en complexiteit van biologische beelddata vraagt om steeds intelligentere methoden en steeds efficiëntere implementaties van deze methoden. De belangrijkste conclusie van dit hoofdstuk is dat, hoewel er al verschillende methoden zijn ontwikkeld voor biologische beeldanalyse, bijna elke specifieke toepassing vraagt om meer gespecialiseerde methoden voor een optimale analyse, verwerking, en interpretatie van de beeldinformatie. In de volgende hoofdstukken van het proefschrift worden daartoe nieuwe methoden voorgesteld en geëvalueerd.

Hoofdstuk 3 beschrijft en evalueert een gespecialiseerd algoritme voor het segmenteren en volgen van cellen in beeldseries. Het behoort tot de klasse van variationele methoden en is in staat om vooraf bekende informatie over de locatie en andere eigenschappen van cellen te benutten. In elk beeld van een tijdsopname wordt de segmentatieprocedure geïnitieerd met de resultaten uit het vorige beeld.

De contour van elke cel in het beeld wordt vervolgens gevonden door evolutie van het contourmodel vanuit de initiële positie. Dit wordt bereikt door minimalisatie van een energiefunctionaal die beeldinformatie (intensiteiten in en rondom de cellen) combineert met contourinformatie (de gladheid van het model). Het iteratieve minimalisatieproces wordt slechts uitgevoerd in een smalle band rondom de celcontouren en levert een interpolatie op van de beweging en deformatie van elke cel in het tijdsinterval tussen elke twee opeenvolgende beelden. Hiermee wordt automatisch het volgen van alle cellen bewerkstelligd. Voor het modelleren van cellen maakt het algoritme gebruik van zogenaamde level-sets, vanwege hun vermogen om sterk inhomogene gebieden te segmenteren, hun topologie te veranderen (wat vooral handig is in het geval van delende cellen), en om toegepast te worden op data met een willekeurig aantal dimensies.

Bij de ontwikkeling van het algoritme is bijzondere aandacht besteed aan de verbetering van de kwaliteit van zowel de segmentatie als van het volgen van de cellen, omdat zelfs kleine fouten in dit stadium aanzienlijke invloed kunnen hebben op vervolganalyses. Belangrijke uitdagingen omvatten het verminderen van het aantal benodigde parameters, een correcte behandeling van elkaar rakende cellen en van delende cellen, het verbeteren van de initiële segmentatie, en de convergentie van het algoritme. Voor elk van deze aspecten zijn nieuwe of verbeterde oplossingen ontwikkeld. Met het oog op mogelijke toepassingen in zogenaamde high-throughput experimenten is ook veel aandacht besteed aan computationele efficiëntie. Het algoritme is gevalideerd op vier verschillende typen fluorescentie microscopie beeldseries, door vergelijking met zowel menselijke experts (die als referentie worden gebruikt) en andere algoritmes ontwikkeld voor hetzelfde doel. De resultaten tonen de superioriteit aan van het in het hoofdstuk beschreven algoritme. Bovendien is het algoritme efficiënt, onbevooroordeeld, en weinig gevoelig voor parameterwaarden, waardoor het geschikt is voor gebruik in een breed scala van gerelateerde biologische toepassingen.

Als volgende stap in de ontwikkeling van een systeem voor multischaal biologische analyse, beschrijft Hoofdstuk 4 een algoritme voor het uitvoeren van intracellulaire analyse. Dit algoritme gebruikt als input de resultaten van de geautomatiseerde cel segmentatie en volging, en voert de volgende taken uit: celbewegingscorrectie, segmentatie van intracellulaire foci, en de analyse daarvan. De bewegingscorrectiestap is een belangrijke schakel tussen de segmentatie en volging enerzijds, en de intracellulaire analyse anderzijds, aangezien daarmee intracellulaire bewegingen gescheiden worden van de globale beweging van een cel. In het gepresenteerde algoritme wordt dit bereikt door per cel alle betreffende gebieden in de opeenvolgende beelden in een serie te registreren ten opzichte van het eerste beeld. De mogelijkheid om vervolgens intracellulaire dynamische processen te bestuderen wordt aangetoond door de analyse van foci, kleine fluorescente gebieden die de aanwezigheid van specifieke proteïnen aangeven, en die beeldstructuren vormen die zeer vaak voorkomen in biologische studies. Voor de segmentatie daarvan is een algoritme ontwikkeld dat potentiële foci detecteert, segmenteert, en tenslotte selecteert op basis van statistische criteria. Het algoritme is vrij generiek, doordat het slechts weinig a priori informatie vereist, en kan dus worden gebruikt voor de analyse van verschillende soorten foci. Het algoritme is gevalideerd door herhaling van een ex-

periment dat eerder handmatig is uitgevoerd, waarbij het ging om het meten van aantallen foci. Uit de resultaten blijkt dat de automatisch en handmatig verkregen waarden leiden tot dezelfde biologische conclusies, hetgeen aantoont dat de automatische methode de handmatige methode kan vervangen in het uitvoeren van dergelijke analyses. Tenslotte wordt aangetoond hoe de statistieken verkregen uit de foci analyse (aantallen, gemiddelde grootte, intensiteit, en afstand tot de celkernmembranen) kunnen worden gebruikt voor de automatische herkenning van de fase van cellen gelabeld met een specifiek antigeen (PCNA). Elk van de bestudeerde fasen van de celcyclus vertoont namelijk een kenmerkend patroon van PCNA foci. Deze aanpak is heel anders dan traditionele methoden voor dynamische celfaseherkenning, die voorafgaande training van een model vereisen.

Tenslotte wordt in Hoofdstuk 5 het in Hoofdstuk 2 ontwikkelde algoritme voor cel segmentatie en volging toegepast op een zeer uitdagend probleem: de reconstructie van de afkomst van alle cellen in *C. elegans* embryogenese. Met behulp van moderne fluorescentie microscopen is het mogelijk om de ontwikkeling van *C. elegans* te volgen vanaf het zygote stadium tot een volledig volwassen organisme. De ruimtelijke en temporele beeldresolutie is voldoende om de afzonderlijke cellen in het organisme te onderscheiden, zelfs in latere stadia van de ontwikkeling, en om eenzelfde cel te volgen tussen twee opeenvolgende beelden in een serie. Dit maakt fluorescentie microscopie een uitstekend hulpmiddel in de ontwikkelingsbiologie, waar *C. elegans* een van de meest populaire modelorganismen is, dankzij de invariantie van de afkomstboom van de cellen. De reconstructie van deze afkomstboom uit de beeldinformatie is echter een zeer complexe taak, die op dit moment, met uitzondering van de vroege stadia van de ontwikkeling, meestal handmatig wordt uitgevoerd, wat niet alleen tijdrovend maar ook foutgevoelig is. De automatisering van deze taak met behulp van computeralgoritmes resulteert niet alleen in een drastische verhoging van de productiviteit, maar biedt ook aanvullende analysemogelijkheden. Bijvoorbeeld, een methode die cellen niet alleen kan volgen maar ook segmenteren, maakt een analyse mogelijk van de expressie van verschillende genen in elk stadium van de embryogenese.

De gepresenteerde methode, welke gebaseerd is op energiminimalisatie, kan cellen tegelijkertijd segmenteren en volgen. Het algoritme uit Hoofdstuk 2 is aanzienlijk aangepast en uitgebreid om deze geschikt te maken voor het analyseren van in totaal meer dan 10.000 cellen op verschillende tijdstippen in *C. elegans* beelddata. De toenemende complexiteit van het probleem (het groeiend aantal cellen in de tijd), samen met de afnemende beeldkwaliteit (ten gevolge van blekingsprocessen), en de propagatie van segmentatiefouten (door beperkingen van het algoritme), maken het volgen na een bepaalde fase (doorgaans het stadium van 350 cellen) vrijwel onmogelijk. De vervanging van de energiminimalisatie met level-sets door een veel efficiëntere aanpak gebaseerd op het zogenaamde graph-cut algoritme, maakt het mogelijk om de segmentatie van een beeld met ongeveer 350 cellen binnen een redelijke tijd uit te voeren. Net als met level-sets worden de graph-cuts geminimaliseerd in een smalle band rondom de celcontouren, waardoor ze geschikt zijn voor het volgen ervan. Daarnaast heeft de methode speciale ingebouwde algoritmen voor het afhandelen van mogelijke botsingen tussen de cellen en het bijhouden van delende cellen. Deze zijn afhankelijk van a priori informatie over de karakteristieke vorm van *C. ele-*

gans kernen en hun delingspatroon. Vier beeldseries van twee verschillende laboratoria zijn gebruikt voor de validatie van de methode. De resultaten tonen aan dat het met behulp van de voorgestelde methode mogelijk is om *C. elegans* embryogenese goed te volgen tot ten minste het stadium van 350 cellen. Het beschreven algoritme is volledig geautomatiseerd, maar het gebruik in semi-automatische modus, waarbij fouten direct na het optreden worden gecorrigeerd ter voorkoming van foutpropagatie, geeft betere resultaten. Hoewel er dus nog ruimte is voor verdere verbetering, biedt de methode op dit moment al een sterke vergemakkelijking van het werk van biologen bij de analyse van *C. elegans* embryogenese.

Samenvattend toont dit proefschrift de mogelijkheden van gespecialiseerde methoden voor de automatische en kwantitatieve analyse van biologische beeldseries gemaakt met fluorescentie microscopie aan. In het bijzonder worden verschillende wiskundige concepten zoals variationele calculus, energiminimalisatie, en partiële differentiaalvergelijkingen toegepast en afgestemd op de segmentatie en het volgen van objecten in beelden op verschillende schaalniveaus van biologisch onderzoek. De gepresenteerde algoritmen zijn ontwikkeld voor het oplossen van een aantal belangrijke praktische problemen die zich voordoen bij de analyse van fluorescentie microscopie beelden: het segmenteren en volgen van cellen, bewegingscorrectie, intracellulaire analyse van fluorescente foci, en de reconstructie van de afkomst van cellen in *C. elegans* embryogenese. Hoewel de onderliggende technieken vrij generiek zijn, zijn de ontwikkelde algoritmen specifiek gemaakt voor optimale extractie van informatie uit de gegeven typen beelden, waardoor hun directe toepassing op andere data typen beperkt kan zijn. Een ander potentieel nadeel van de variationele energiminimalisatie methoden is dat ze in het algemeen veel rekenkracht vereisen. Voor elke specifieke toepassing dient daarom de juiste balans te worden gevonden tussen de nauwkeurigheid van de resultaten en de vereiste reken-tijd. Het oplossen van deze problemen zal leiden tot een verdere verbetering van de toepasbaarheid van deze methoden in biologische studies, en zal de gepresenteerde methoden uiteindelijk maken tot belangrijke instrumenten in high-throughput experimenten.

Acknowledgement

At the moment when I will be defending this thesis, it will be almost five years since I started working on this project joining the Biomedical Imaging Group Rotterdam. Five long years, during which I met many interesting people who had strong influence on my life and work. Some of these people, as well as other important people in my life, I want to acknowledge here.

First of all, I want to express my gratitude to my promotor Prof. Wiro Niessen and co-promotor Erik Meijering for giving me the opportunity to perform research on such an exciting subject within a truly excellent environment. I really enjoyed working with both of you, and tried to learn from you as much as possible. Wiro, I truly admire your deep and detailed theoretical knowledge, your broad view of the field, and your perpetual enthusiasm and energy in each of the many things you are involved in: supervising, organizing, teaching. Erik, having you next to me as my supervisor during these years not only made my life as a Ph.D. student much easier, but also gave me a great example how much more space I still have for my personal improvement.

I am also grateful to all my collaborators, who contributed to this work by challenging me with very interesting biological problems, providing the data, patience in waiting for the results, and, especially, for letting me learn about many new and exciting things. Gert van Cappellen, Jeroen Essers, and Akiko Inagaki: thank you for all the interesting discussions, ideas, editing, and not being scared of doing “dirty” work like producing manual segmentations. Rob Jelier, Ben Lehner, and Angela Krüger: I really enjoyed visiting your lab in Barcelona. Thank you for all your hard work on improving the quality of the images, creative inputs and ideas. I believe that the most exciting things in our project are still ahead, and I am really looking forward to discovering them.

Next, I want to thank the CELMIA people, with whom I also had pleasure to share the office. Ihor, thanks for always being ready to answer (in Ukrainian!) my questions on every possible subject, agreeing to be my paranimf, and just being a great friend. Esben and Noemí, it was my big pleasure having you around. I was truly impressed by your openness, and by how easy you both can get along with new people and in no time become centers and catalysts of all possible activities.

Gyula, I was really enjoying our train chats about everything what was interesting and important in our lives: family, hobbies, work.

I also want to thank all the BIGR people I worked with: Adriënne, Albert, Alfonso, Arna, Azadeh, Coert, Danijela, Désirée, Diego, Dirk, Empar, Eugene, Fedde, Hakim, Henri, Hortenese, Hui, Jifke, Karin, Lejla, Marcel K. Marcel van S., Marius,

Marleen, Mart, Michiel, Nóra, Petra, Rahil, Rashindra, Reinhard, Renske, Stefan, Theo, and all the colleagues from the faculties of Medical Informatics and Radiology. You are all very different, but, nevertheless, such versatility has produced a great working atmosphere, which I was enjoying throughout my whole stay at the Erasmus MC.

Eva, you were next to me for most of these years, believing in me, supporting me, and sharing every little thing in my life, no matter if it was happy or sad, exciting or frustrating. Thank you for all of it!

Окремо хочу подякувати моїм друзям, без яких моє життя було би просто безбарвним. Ігор О., Сергій і Софія: я дуже вдячний вам за ваше вміння (і бажання!) вислухати, порадити (а то й розрадити. . .), і просто за те що ви є у моєму житті. Ігор М., Андрій і Оксана: на жаль, усі ці роки ми не мали змоги спілкуватись і бачитись так часто як би того хотілось. Але ваша підтримка в досить непростий для мене час була просто неоціненною (Андрієві хочу виразити окрему подяку за згоду бути моїм паранімфом).

І, звичайно, найбільша моя подяка найважливішим людям у моєму житті, моїй сім'ї: мамі Оксані, татові Миколі, сестрі Юлії, швагрові Володі, племінникові Ромчикові, бабцям Дарії та Євгенії. Дякую вам за все, а насамперед: за вашу любов, турботу та підтримку!

Finally, I want to thank God for inspiring me, guiding me through all these years, and giving me strength to finish the work and to write this book.

Oleh Dzyubachyk
Rotterdam, March 2011

Олег Дзюбачик
Роттердам, Березень 2011

PhD Portfolio

In-Depth Courses:

Measuring Features, ASCI	2006
Front-End Vision and Multiscale Image Analysis, ASCI	2006
Knowledge driven Image Segmentation, ASCI	2007
BioInformatics, ASCI	2007

Other Presentations:

Medical Informatics PhD Days, Berg en Dal	2007
Research seminars: Biomedical Imaging Group Rotterdam (4x), Department of Medical Informatics (2x)	2007– 2010

Attending International Conferences:

IEEE Nonlinear Statistical Signal Processing Workshop: Classical, Unscented and Particle Filtering Methods, Cambridge, UK	2006
IEEE International Symposium on Biomedical Imaging: From Nano to Macro, Arlington, VA, USA	2007
IEEE International Symposium on Biomedical Imaging: From Nano to Macro, Paris, France	2008
IEEE International Symposium on Biomedical Imaging: From Nano to Macro, Boston, MA, USA	2009
Annual International Conference of the IEEE Engineering in Medicine and Biology Society, Minneapolis, MN, USA	2009
IEEE International Symposium on Biomedical Imaging: From Nano to Macro, Rotterdam	2010

Attending International Workshops:

The Colored Revolution of Bio-imaging: New Opportunities for Signal Processing, Arlington, VA, USA	2007
Advanced Optical Microscopy: Challenges and Opportunities, Paris, France	2008
High Performance Medical Image Computing, Boston, MA, USA	2009
Optical Microscopy and Deconvolution, Rotterdam	2010

Other:

Reviewing for IEEE Transactions on Image Processing, Computer Methods and Programs in Biomedicine, Journal of Microscopy	2008–2011
--	-----------

Publications

Publications in International Journals:

- E. Meijering, **O. Dzyubachyk**, I. Smal, W. A. van Cappellen, "Tracking in Cell and Developmental Biology". *Seminars in Cell and Developmental Biology*, vol. 20, no. 8, October 2009, pp. 894–902
- **O. Dzyubachyk**, W. A. van Cappellen, J. Essers, W. J. Niessen, E. Meijering, "Advanced Level-Set Based Cell Tracking in Time-Lapse Fluorescence Microscopy". *IEEE Transactions on Medical Imaging*, vol. 29, no. 3, March 2010, pp. 852–867
- **O. Dzyubachyk**, J. Essers, W. A. van Cappellen, C. Baldeyron, A. Inagaki, W. J. Niessen, E. Meijering, "Automated Analysis of Time-Lapse Fluorescence Microscopy Images: From Live Cell Images to Intracellular Foci". *Bioinformatics*, vol. 26, no. 9, October 2010, pp. 2424–2430
- **O. Dzyubachyk**, R. Jelier, A. Krüger, W. J. Niessen, B. Lehner, E. Meijering, "Model-Evolution Based Tracking of *Caenorhabditis Elegans* Embryogenesis in Fluorescence Microscopy", *prepared for submission*

Book Chapters:

- E. Meijering, I. Smal, **O. Dzyubachyk**, J.-C. Olivo-Marin, "Time-Lapse Imaging" in *Microscope Image Processing*, Q. Wu, F. A. Merchant, K. R. Castleman (eds.), Elsevier Academic Press, Burlington, MA, Chapter 15, pp. 401–440, 2008

Publications in International Conference Proceedings:

- **O. Dzyubachyk**, W. Niessen, E. Meijering. "A Variational Model for Level-Set Based Cell Tracking in Time-Lapse Fluorescence Microscopy Images", in *IEEE International Symposium on Biomedical Imaging: From Nano to Macro — ISBI 2007* (4th international conference, held in Arlington, VA, USA, April 12–15, 2007), J. Fessler and T. Denney (eds.), IEEE, Piscataway, NJ, pp. 97–100, 2007
- **O. Dzyubachyk**, W. Niessen, E. Meijering, "Advanced Level-Set Based Multiple-Cell Segmentation and Tracking in Time-Lapse Fluorescence Microscopy

Images", in *IEEE International Symposium on Biomedical Imaging: From Nano to Macro — ISBI 2008* (5th international conference, held in Paris, France, May 14–17, 2008), J.-C. Olivo-Marin, I. Bloch and A. Laine (eds.), IEEE, Piscataway, NJ, pp. 185–188, 2008

- **O. Dzyubachyk**, W. A. van Cappellen, J. Essers, W. Niessen, E. Meijering, "Energy Minimization Methods for Cell Motion Correction and Intracellular Analysis in Live-Cell Fluorescence Microscopy", in *IEEE International Symposium on Biomedical Imaging: From Nano to Macro — ISBI 2009* (6th international conference, held in Boston, MA, USA, June 28–July 1, 2009), W. C. Karl, B. Rosen, D. Brooks (eds.), IEEE, Piscataway, NJ, pp. 1127–1130, 2009
- **O. Dzyubachyk**, R. Jelier, B. Lehner, W. Niessen, E. Meijering, "Model-Based Approach for Tracking Embryogenesis in *Caenorhabditis Elegans* Fluorescence Microscopy Data", in *31st Annual International Conference of the IEEE Engineering in Medicine and Biology Society (EMBC '09)* (held in Minneapolis, MN, USA, September 3–6, 2009), Z.-P. Liang (edt.), IEEE, Piscataway, NJ, pp. 5356–5359, 2009
- N. Carranza, I. Smal, **O. Dzyubachyk**, W. Niessen, E. Meijering, "Automated Lineage Tree Reconstruction from *Caenorhabditis Elegans* Image Data using Particle Filtering Based Cell Tracking", in *IEEE International Symposium on Biomedical Imaging: From Nano to Macro — ISBI 2011* (8th international conference, to be held in Chicago, IL, USA, March 29–April 3, 2011)

Color Image Section

Chapter 2

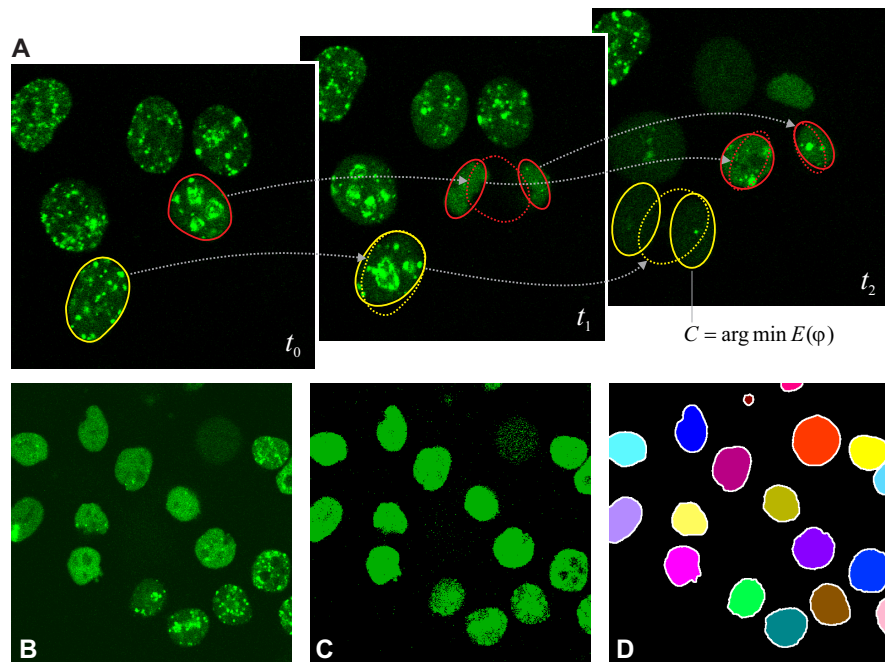


Figure. 2.1 (see page 11): Cell tracking. (A) Three frames from a time-lapse fluorescence microscopy image, illustrating the concept of model-evolution based cell segmentation and association. Cell contours or surfaces can be defined parametrically or as the zero-level of a higher-dimensional function. In each image frame, the final contour of a cell (solid line) is obtained by minimization of an energy functional, typically consisting of image-based and shape-based terms. The initial cell contour (dotted line) for each frame is usually taken to be the final contour from the previous frame. Cell divisions can be detected by monitoring the shape of the contour function during energy minimization. (B) Depending on the type of labeling, the appearance of cells (or in this case their nuclei) may vary greatly, within one frame as well as over time. (C) Thresholding usually results in a very noisy (at low thresholds) or fragmented (at high thresholds) segmentation. (D) Model-based segmentation (in this case using level sets) can yield much more sensible results.

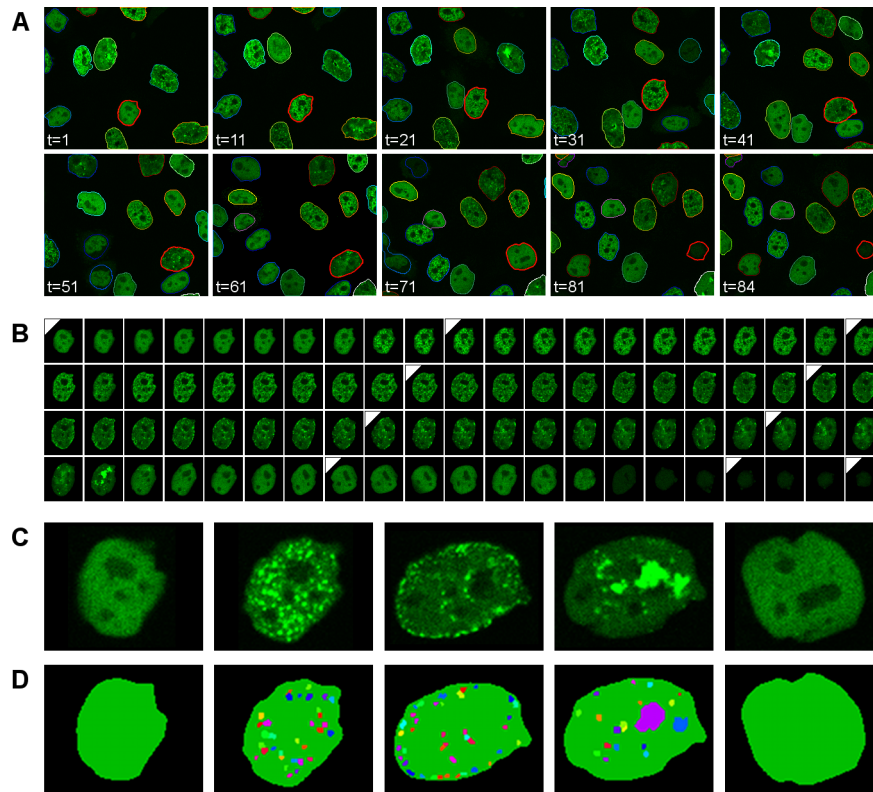


Figure. 2.2 (see page 14): Example of cell motion correction. (A) One cell followed through the time-lapse fluorescence microscopy image data set (outlined). During its lifetime the cell undergoes complex changes: movement, deformations, rotations, etc. (B) Cell segmentation and tracking enables extraction of each of the cells separately at every moment of time and bringing all the extracted regions occupied by the same cell to the “frozen” coordinate system by applying motion correction. Marked time points correspond to the time points shown in panel (A). In this case only the global motion of the nucleus is subtracted. (C,D) Appearance and result of segmentation of the PCNA foci for each stage of the cell cycle: G1, early-S, mid-S, late-S and G2 correspondingly (magnified).

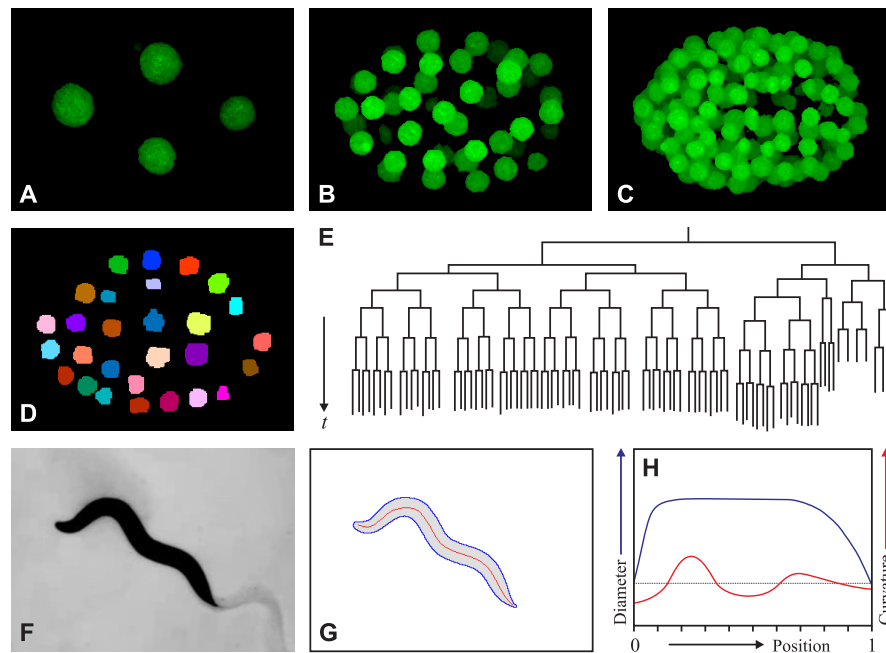


Figure. 2.3 (see page 17): Organism tracking. (A-C) Volume renderings of three time points (3D image stacks) from a time-lapse fluorescence microscopy data set, showing *C. elegans* embryogenesis from the four-cell stage to approximately one and two hours later, respectively. The rapidly increasing number of cells and cell density pose a real challenge for automated cell tracking. (D) Result of 3D segmentation (only one plane is shown here) obtained by applying a level-set based model-evolution algorithm and morphological postprocessing to the stack rendered in (C). (E) Tracking results can be conveniently summarized and presented (after completion or even in the process) using lineage trees, which give a clear picture of mother-daughter relations of cells, division times, and symmetry breaking events. (F) Single frame from time-lapse image data acquired using a dissecting microscope and showing the morphological and behavioral phenotypes of an adult worm. (G) Owing to the high contrast in the image, the worm body can be accurately segmented using intensity thresholding, and simple morphological operations subsequently yield the outer contour and centerline ("skeleton"). (H) Finally, a variety of morphological features, such as body diameter and curvature, can be easily computed at any position along the extracted centerline.

Chapter 3

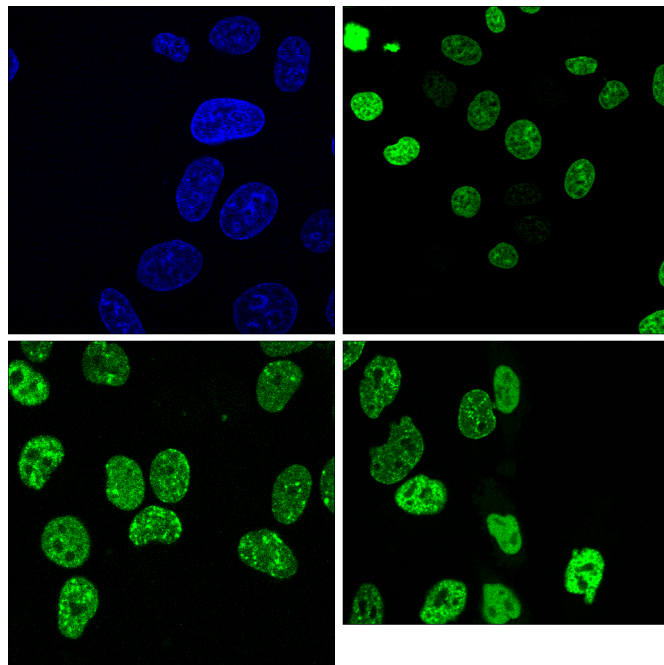


Figure. 3.1 (see page 23): Sample images from the data sets used in this study. From top-left to bottom-right: Hoechst-labeled HeLa cells, H2B-GFP labeled HeLa cells, RAD18-YFP labeled HeLa cells, and PCNA-GFP labeled CHO cells (see Section 3.4 for abbreviations and experimental details).

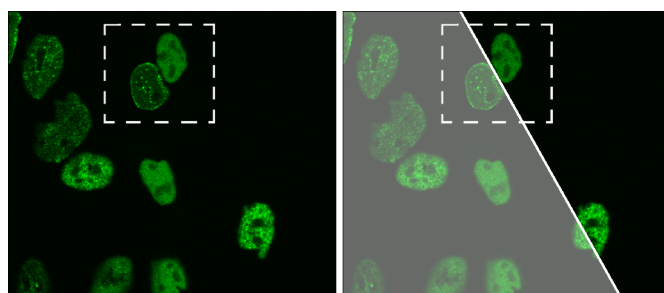


Figure. 3.3 (see page 37): Two closely positioned cells separated using the Radon transform. The transform is computed in a small region around the two cells (indicated by the dashed rectangles in the images), and a separating plane is obtained by finding the correct local minimum in the transform, which is used to construct evolution masks for the level-set functions corresponding to the two cells (one mask is shown as a shaded area in the right image).

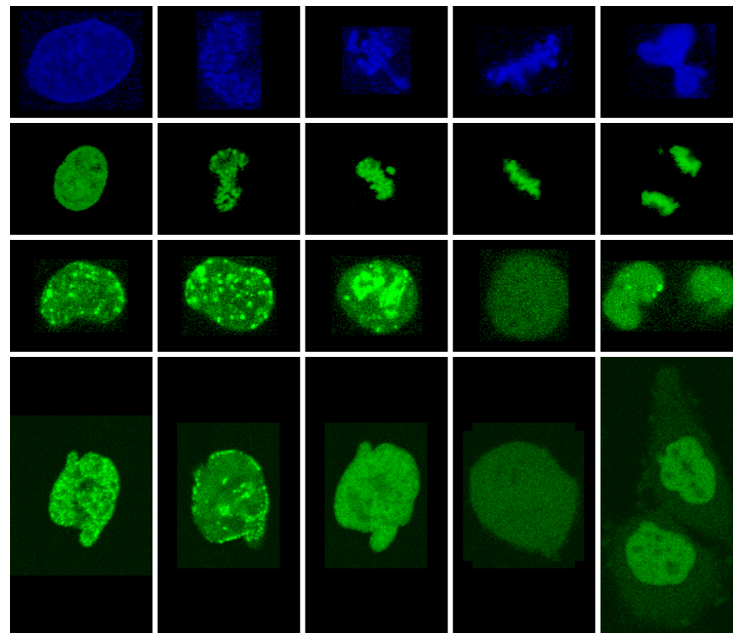


Figure. 3.5 (see page 40): Typical appearance of the nuclei through the cell cycle under different staining: Hoechst (first row), H2B-GFP (second row), RAD18-YFP (third row) and PCNA-GFP (fourth row). These images clearly indicate the difficulty connected with tracking mitosis events caused by dramatic change of nuclei shape and intensity during cell division.

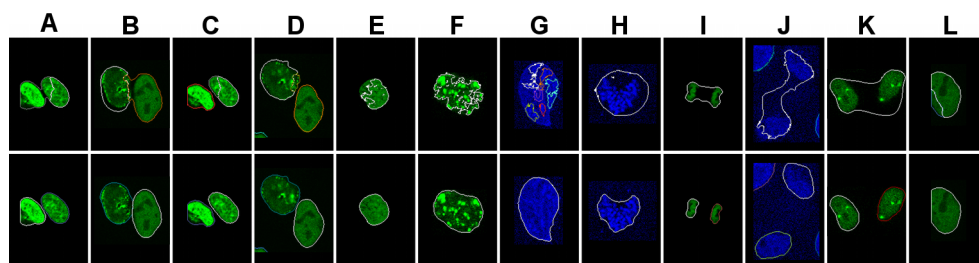


Figure. 3.9 (see page 47): Typical examples of errors produced by the original multiple-level-set tracking algorithm (top row) in comparison with improved performance by our modified algorithm (bottom row): (A,B) incorrect separation of two touching cells; (C,D) contour splitting as a result of such incorrect separation (this may lead to detection of cell division that in reality did not occur); (E,F) incorrect segmentation of objects with complex foreground intensity distribution; (G) the same, which leads to breaking of the contour into a number of sub-contours segmenting intracellular structures instead of the whole nucleus; (H) disability to handle rapid shape change; (I–K) difficulty with properly handling the correct moment of cell division, which may cause a significant delay of detection of this event; (L) incorrect identification of a part of an existent object located at image's boundary as a new object.

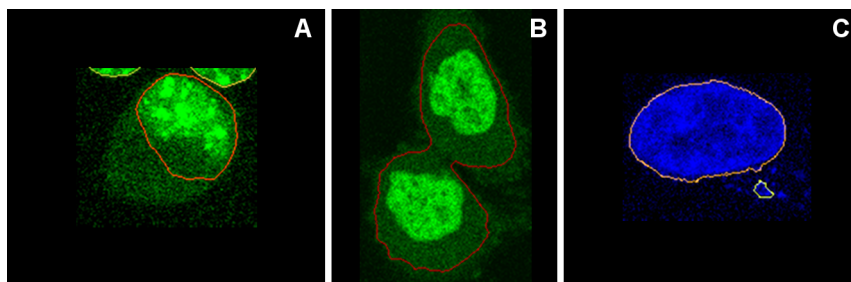


Figure. 3.10 (see page 47): Typical examples of segmentation and tracking errors produced by our algorithm: (A) incorrect segmentation after rapid change of objects's shape and contrast (correct segmentation was recovered after the next time step); (B) delayed detection of cell division event (separation of daughter nuclei); (C) false cell division event due to rare event (appeared apoptotic cell) in the vicinity of the object.

Chapter 4

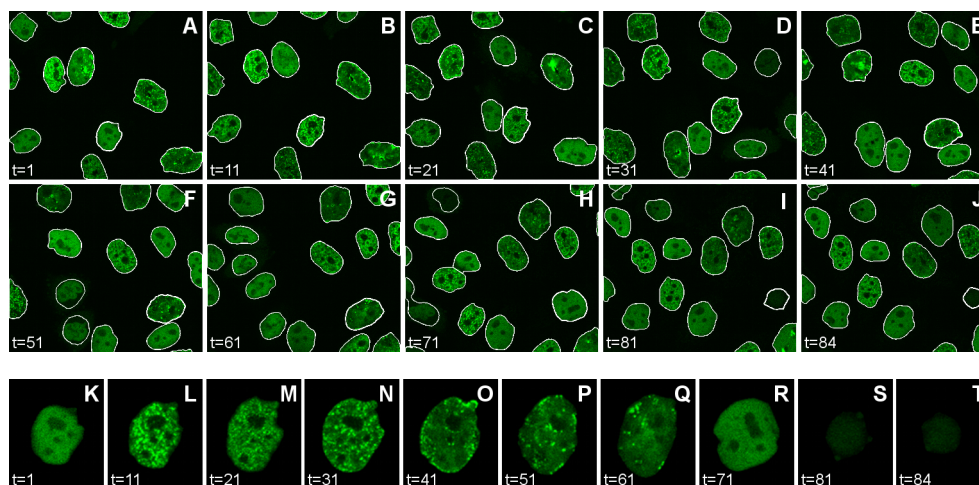


Figure. 4.1 (see page 52): Example of motion correction using the proposed approach. The two top rows show the motion of one cell extracted from a time-lapse fluorescence microscopy image data set (outlined in white). One slice ($z = 1$) is shown for time steps 1, 11, 21, 31, 41, 51, 61, 71, 81, and 84. The third row shows (magnified) the result of cell motion correction after segmentation and tracking. In this case only the global motion of the nucleus is subtracted.

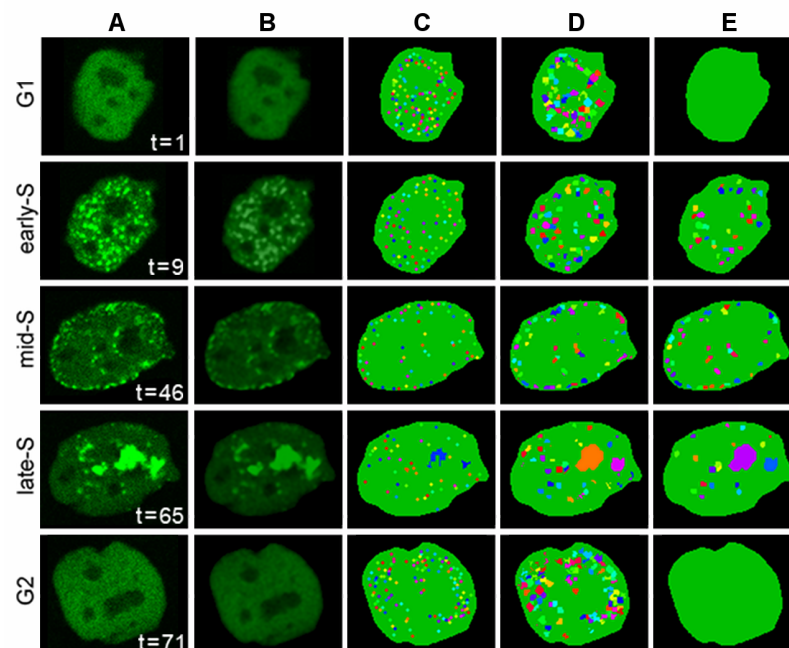


Figure. 4.2 (see page 54): Example of foci segmentation using our algorithm: (A) images of the same nucleus in five different time steps (1, 9, 46, 65, 71), each representing one of the phases of the cell cycle (G1, early-S, middle-S, late-S, G2); (B) results of applying patch-based reconstruction to each image; (C) initially detected foci markers (dots in different colors); (D) results of the graph-cut based segmentation algorithm; (E) final results after foci selection. All images are the first slice ($z = 1$) of the corresponding 3D image stack.

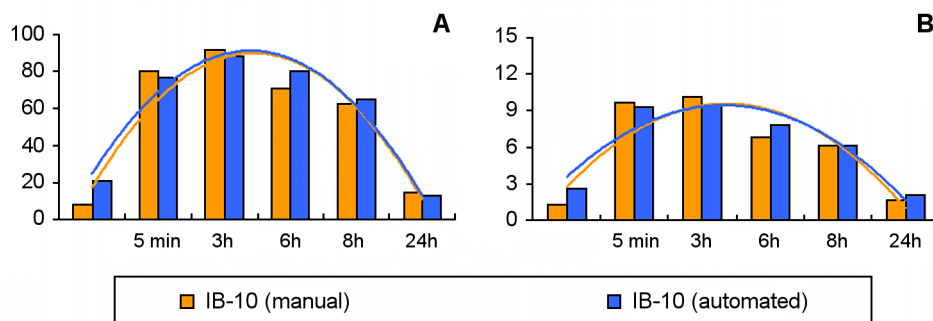


Figure. 4.3 (see page 58): Comparison between manual (orange) and automated (blue) 53BP1 foci counting for normal embryonic stem cells (IB-10) in terms of (A) the percentage of the positive cells and (B) the average number of foci per cell at various time points. For each of the measures the corresponding values and the obtained polynomial trend lines are shown.

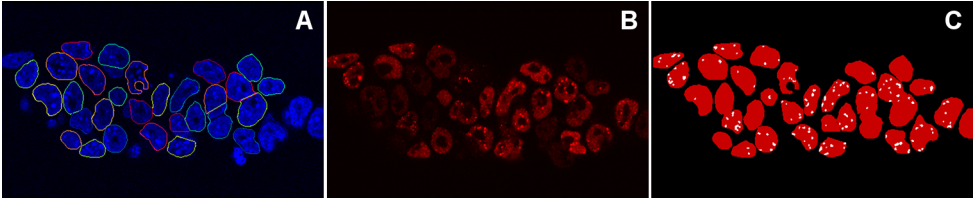


Figure. 4.4 (see page 58): Sample results from the automated foci counting experiment: (A) DNA channel with segmented cell boundaries overlaid (contours of various colors); (B) protein channel; (C) region masks (red) extracted from (A) together with the foci of interest (white) segmented from (B). Each of the images has been cropped from its original size and on the images (A) and (B) contrast enhancement was performed for better visualization.

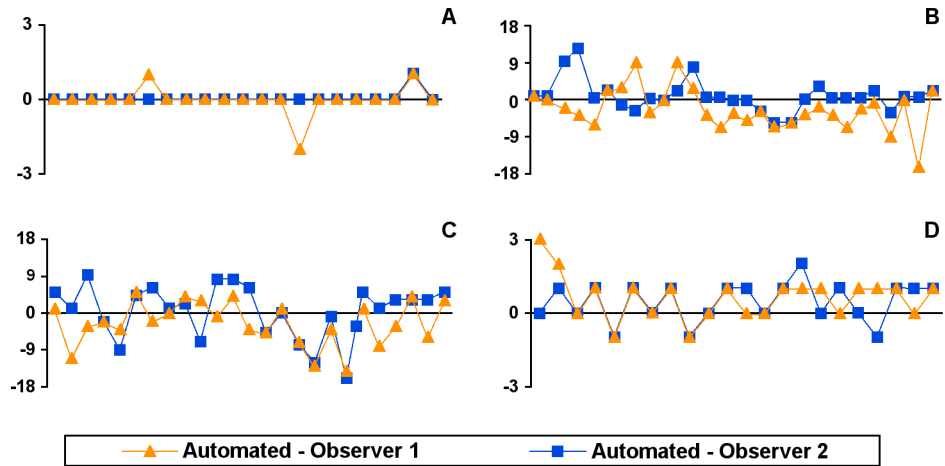


Figure. 4.5 (see page 59): Comparison between manual and automated detection of phase transition moments in PCNA-stained cells. The four plots correspond to the four possible phase transitions: (A) G1 to early-S (21 cases), (B) early-S to middle-S (29 cases), (C) middle-S to late-S (26 cases), and (D) late-S to G2 (22 cases). In each case, the difference in detection times between the automated method and each of the two observers is plotted. A missing point on one of the curves in (C) means that the corresponding phase transition was not detected by the corresponding observer.

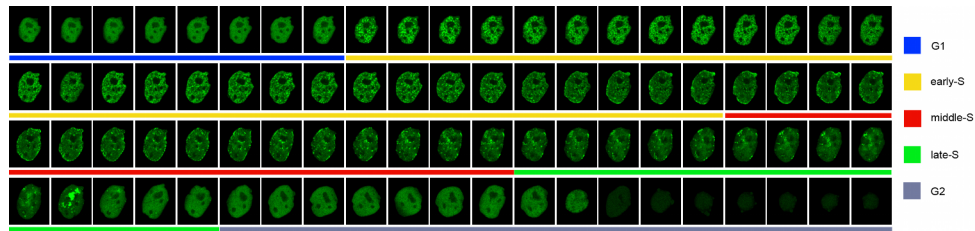


Figure. 4.6 (see page 60): Sample results from the cell phase identification experiment. Shown from top left to bottom right are cropped images of 84 successive time points of a single, motion-corrected cell nucleus, going from the G1 phase, through the early-S, middle-S, late-S, to the G2 phase (indicated by bars in different colors below the images), as automatically recognized by our system based on characteristic foci patterns for each of these phases. The example also illustrates the observation that it is easier (also visually) to distinguish the G phases from the S phases than to distinguish between the different S phases.

Chapter 5

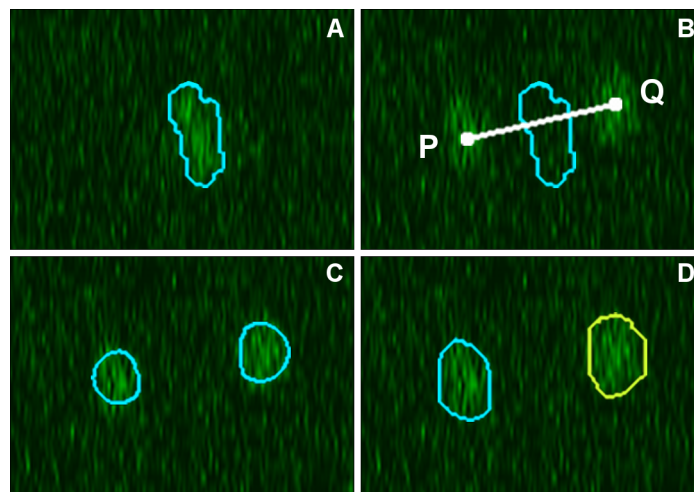


Figure. 5.3 (see page 68): Detection of cell division. The panels show (A) a cell in one time point, with its segmentation (overlaid colored contour), (B) the line connecting markers P and Q of the potential daughter cells, (C) the seeds and (D) final segmentation of the two daughter nuclei.

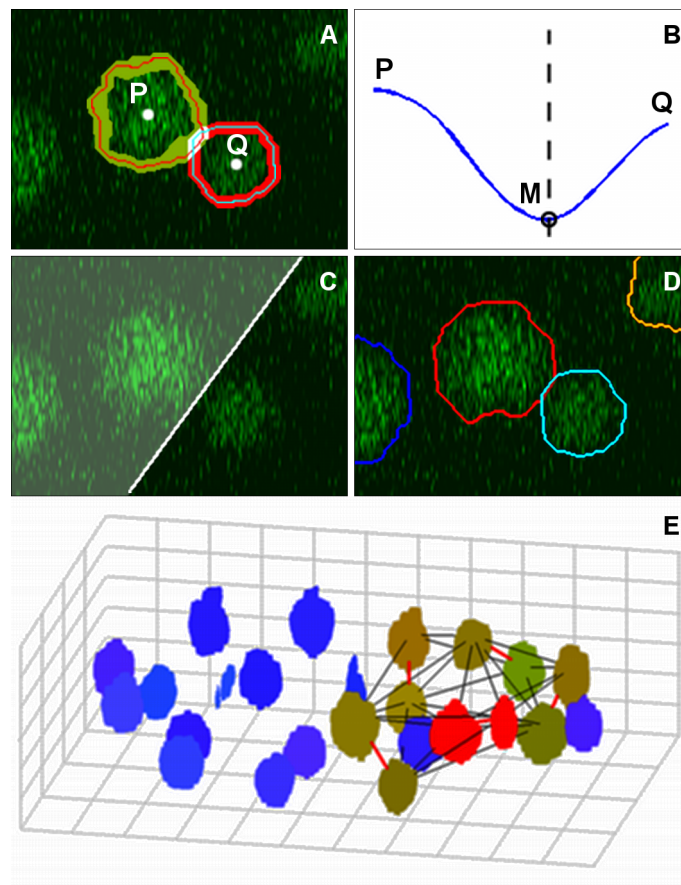


Figure. 5.4 (see page 72): Radon-transform based cell separation. The panels show (A) the initial position of the contours (red and blue curves) of two adjacent cells (P and Q with their markers indicated by dots) for $t = 16$ with corresponding overlapping narrow bands (green and red areas), (B) the intensity profile along the line connecting the markers of the two cells to find the position of minimum intensity (indicated by the dashed vertical line and point M), (C) the separating plane (white line in this single slice) computed from the Radon transform around that position, (D) the final segmentation (colored contours) for $t = 16$, and (E) the selection procedure for adjacent cells that need to be separated. In the latter, all cell nuclei that need to be separated from at least one other cell are shown in shades of green (with the exception of the two cells in panel (A) shown in red), and all remaining cells (not adjacent to any other cell) are shown in shades of blue. All nuclei are shown with smaller size for visualization purposes. The lines connecting the markers of the cell nuclei are the edges of the Delaunay triangulation calculated on the set of adjacent (red and green) objects. Only the edges (highlighted in red) connecting actually adjacent cells are selected for performing Radon-transform based cell separation.

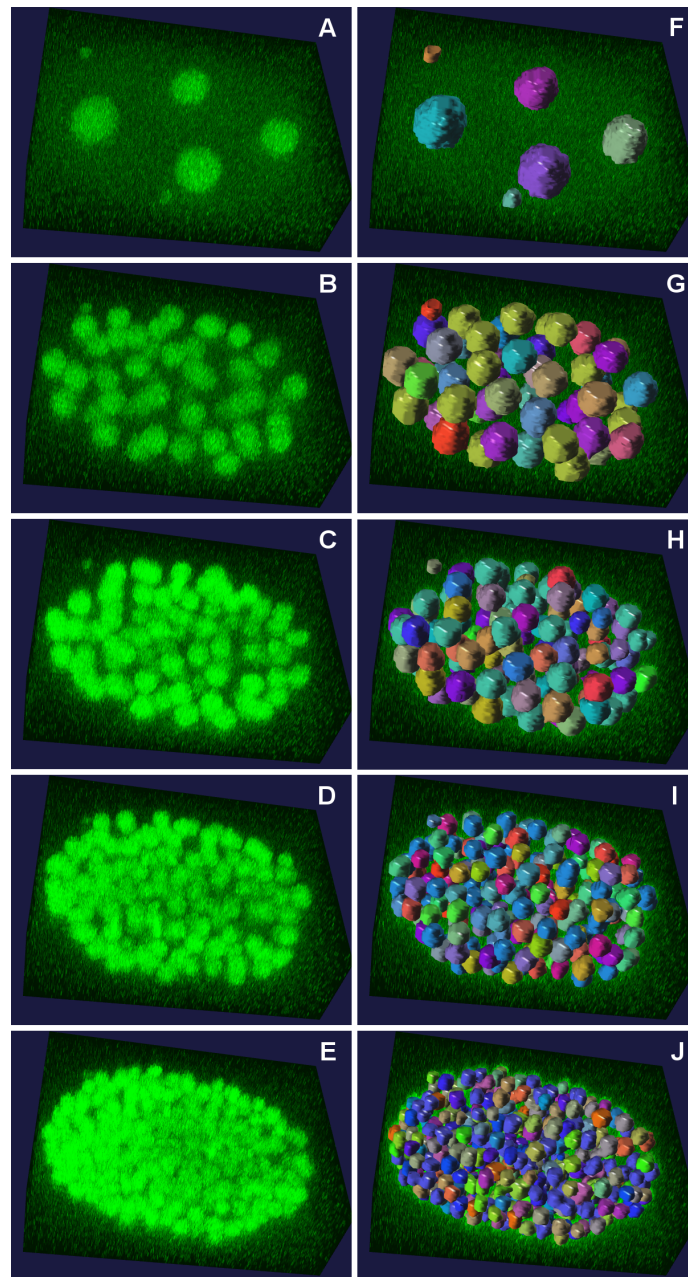
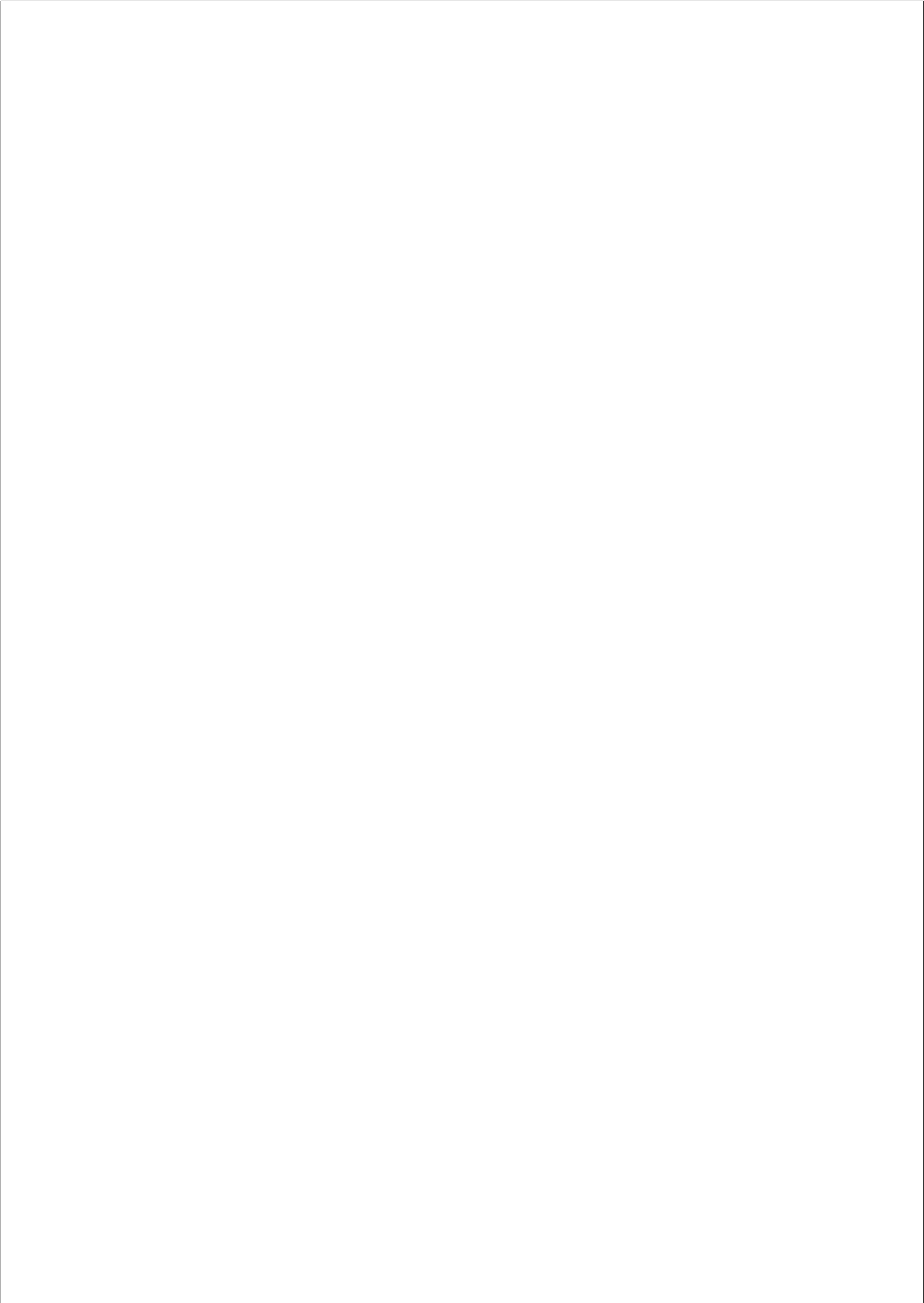


Figure. 5.6 (see page 78): Segmentation result for a sample data set. Original image stacks (A–E) from the 081505 data set (volume renderings) and the corresponding segmentation results (F–J) (surfaces rendered in arbitrary colors on top of the volume renderings) for the 4-cell ($t = 1$), 51-cell ($t = 74$), 102-cell ($t = 115$), 184-cell ($t = 138$), and 350-cell stage ($t = 184$).



Curriculum Vitae

Oleh Dzyubachyk was born in Lviv, Ukraine, on August 20, 1976. He received a M.Sc. degree (cum laude) in Mathematics from Ivan Franko National University of Lviv, Ukraine, in 1998. From 1998 to 2003, he carried out research on modeling coupled fields in ferromagnetic materials at Pidstryhach Institute for Applied Problems of Mechanics and Mathematics (Lviv, Ukraine).

From 2003 to 2005, he was a Research Assistant (postmaster program “Mathematics for Industry”) at the department of Mathematics and Computer Science of Technical University of Eindhoven, the Netherlands. After graduating in 2005 he obtained a Professional Doctorate in Engineering (PDEng) degree.

From 2006 to 2010 Oleh was a Ph.D. student at the Biomedical Imaging Group Rotterdam, part of Departments of Medical Informatics and Radiology of the Erasmus University Rotterdam, the Netherlands. The results of this work are described in this thesis. In October 2010 he joined the Laboratorium voor Klinische en Experimentele Beeldverwerking (LKEB) at the Leiden University Medical Center.